A Quest for the Physics Beyond the Cosmological Standard Model

Thesis by

Lotty Ackerman Mayer

In Partial Fulfillment of the Requirements

for the Degree of

Doctor of Philosophy

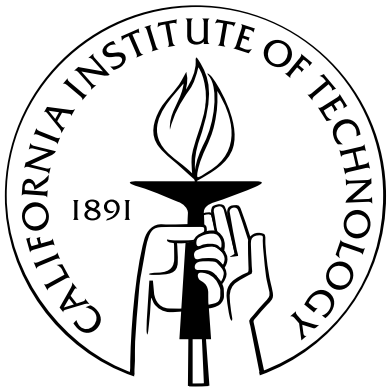

California Institute of Technology

Pasadena, California

2010

(Defended August 13, 2009)

Acknowledgements

The time I have spent at Caltech has been one of scientific and personal development. This thesis owes much to a large number of people that have been influential these past years.

First, I would like to thank my advisor, Sean Carroll. Sean, I thank you for your guidance, support, and encouragement. Thank you for the many exciting, enjoyable, enriching, and insightful conversations about cosmology and for your patience answering my many questions. For me, it has also been very influential to learn from such a great speaker and somebody interested in outreach to non-scientists. You have been an incredible mentor and I will always be grateful.

I am also very grateful to Mark Wise – whom I consider my advisor as well. Thank you for always having your door open for questions about physics and for your support and patience through the years. Thank you for treating your students as collaborators. It has been an honor and very educational to work with you and also to see how you work.

It has been a privilege to collaborate with Marc Kamionkowski and learn from his breadth of knowledge and curiosity about science, as well as being impressed by his intuition. Sean, Mark, and Marc each have a unique intuition about cosmology and physics. Thank you for sharing it with me.

I thank Sunil Golwala for being part of my candidacy and defense committee.

I have been fortunate to collaborate with other astro/physicists as well. I would like to specially thank Hans Kristian Eriksen, Ingunn Wehus, and Nicolaas Groeneboom. Thank you for introducing me to how CMB data is actually gathered and processed, as well as how to code (and in a supercomputer!). Thank you for your patience answering the many questions that this curious person keeps asking. I would also like to thank all of you for inviting me to visit Norway. Not only was it a very

enriching scientific experience, but you made sure to also make it a cultural one. Who knew that tacos were a Norwegian Friday tradition? Thank you for teaching this Venezuelan that snow rolls like a carpet and other fun winter nordic activities. I hope that in the future we can continue collaborating and I can share with you the tropical skills that perhaps would be necessary to survive in the heat of Texas.

I also thank Matt Buckley and Keith Lee for sharing some of their particle physics knowledge with me.

To my other collaborators, Christian Bauer and Michael Graesser, thank you for helping me take my first steps as a researcher.

I would like to thank other current and former members of the phenomenology/cosmology group. In particular Tim Dulaney, Moira Gresham, Matt Johnson, Jennifer Kile, Donal O'Connell, Mike Salem, Heywood Tam, and Sean Tulin. Special thanks to Moira for being such a great officemate and the conversations about cosmology and English that we have had. Special thanks as well to Donal, Mike, and Jen for their help through the years. I would also like to thank Jonathan Pritchard, Tristan Smith, and Jie Yang for many conversations and support. Ketan Vyas, thank you for the many dinners we have had together.

I am grateful to Carol Silberstein for keeping the Theory Group running smoothly as well as for the chocolates and conversations. I would also like to thank Donna Driscoll who has always been happy to help me with the administrative part of the Physics program.

Science for the most part is made in collaboration and in small steps. I acknowledge all the researchers that have contributed to the science involved in this thesis. I also acknowledge the use of technology that we have grown used to, but that is fundamental to the way science is done today. Between other tools, I acknowledge the arXiv, Spires, Google and Latex.

To my family, I am very thankful for the support that you have given me through the years, even when I have chosen an unusual path.

An important part of my experience at Caltech I owe to the friends I have met here. In particular, Lorelei Isaacs, Yashashree Kulkarni, Jennifer Lanski, James Maloney, Jon Othmer, Katalin Othmer, Jonathan Pritchard, Paige Randall, Jess Reynolds, Marie-Helene Rousseau, Amy Trangsrud, Daniel Wagenaar and Rob

Ward. Never before I have encountered such a combination of intelligence, creativity, thoughtfulness, kindness, respect, and appreciation for people's differences and love for learning. I am very thankful to all of you. Thank you for your support, for the time that we have spent together, and for teaching me so many things. I would like to specially thank Katalin. My life at Caltech would certainly been different without you. Thank you for your unconditional support, help, understanding, kindness and adventures through the years.

Abstract

Recent advances in observational cosmology have culminated in the establishment of the cosmological standard model. In spite of this remarkable achievement, the underlying physics remains unknown.

In this thesis we propose models whose predictions can be compared with observations, and can thereby help us discover this as-yet unknown physics of the Universe. We examine (i) the consequences that a preferred direction during the inflationary era would have on the Cosmic Microwave Background (CMB) anisotropies, (ii) the effect of asymmetric beams in the Wilkinson Microwave Anisotropy Probe (WMAP), (iii) astrophysical consequences of a dark photon that couples only to dark matter, and (iv) explore a mechanism for producing density perturbations during the period of reheating.

Contents

Acknowledgements **iii**

Abstract **vi**

1 Introduction **1**

1.1 Imprints of a Primordial Preferred Direction on the Microwave Background 3

1.2 Preliminary Investigation on the Effect of Asymmetric Beams in the Wilkinson Microwave Anisotropy Probe Experiment 4

1.3 Dark Matter and Dark Radiation 4

1.4 Light Scalars and the Generation of Density Perturbations During Preheating or Inflaton Decay 6

2 Imprints of a Primordial Preferred Direction on the Microwave Background **7**

2.1 Introduction 7

2.2 Microwave Background 10

2.3 Inflation Model with a Preferred Direction 14

2.4 Concluding Remarks 22

3 Preliminary Investigation on the Effect of Asymmetric Beams in the Wilkinson Microwave Anisotropy Probe Experiment **24**

3.1 Introduction 24

3.2 Pipeline overview 27

3.2.1 Simulation of time-ordered data 28

3.2.2 Map making with differential data 30

3.2.3 Estimation of hybrid beam transfer functions 33
3.3 Data and simulations 35
3.4 Comparison with analytic case 37
3.5 The effect of asymmetric beams in WMAP 39
3.6 Impact on cosmological parameters 42
3.7 Conclusions 45

4 Dark Matter and Dark Radiation 54
4.1 Introduction 54
4.2 Dark Radiation and the Early Universe 58
4.3 Galactic Dynamics 67
4.4 Weakly Coupled Models 74
4.5 Other Effects of Dark Photons 78
4.5.1 Bremsstrahlung 78
4.5.2 Structure Formation 79
4.5.3 Plasma Instabilities 81
4.6 Conclusions 82

5 Light Scalars and the Generation of Density Perturbations During Preheating or Inflaton Decay 86

A Convergence of the Differential Map Maker 101

Bibliography 104

List of Figures

3.1 Comparison between the analytic expression for the transfer function for a Gaussian beam of $20'$ FWHM with the transfer function computed from direct simulation 48
3.2 Comparison of the V1 WMAP beam transfer functions obtained from six and twelve months of observations 49
3.3 Comparison between transfer functions derived in this chapter to the nominal WMAP transfer functions 50
3.4 The ratio between the transfer functions derived in this chapter and the nominal WMAP transfer functions for all DAs 51
3.5 Difference between a V1 simulation convolved with the full asymmetric beam and the same realization convolved with the corresponding symmetrized transfer function 52
3.6 Total correction to the 5-year co-added WMAP temperature power spectrum due to asymmetric beams 53
3.7 Marginal distributions for cosmological parameters derived with and without correction for asymmetric beams 53

4.1 The allowed values of dark $g_{\rm light}$ (those degrees of freedom relativistic at $T_{\rm BBN}$) and $g_{\rm heavy}$ (the remaining dark degrees of freedom) arising from BBN constraints 62
4.2 Pair annihilation/creation of dark matter χ into dark photons $\hat{\gamma}$ . . . 63
4.3 The allowed regions of $\hat{\alpha}$ vs. m_χ parameter space 65
4.4 Feynman diagrams leading to $\gamma/\hat{\gamma}$ mixing 76
4.5 Feynman diagram leading to $\hat{\gamma}$ interactions with SM fermions 77
4.6 The leading order interaction of the dark sector with SM fermions . . 77

5.1 Quantum corrections may generate a dependence of m_χ^2 on super-horizon fluctuations in σ. 89
5.2 Logarithmic plot of $R = \rho_\chi/\rho_\Phi$ 97
5.3 Logarithmic plot of the effect of the mass fluctuation δm_χ^2 on $z_{\rm RH}$ . . 98
5.4 Logarithmic plot of the effect of the fluctuation in the coupling constant δg^2 on $z_{\rm RH}$ 98

A.1 Comparison of convergence of the differential map maker for two different choices of initialization 103

List of Tables

3.1 Summary of DA parameters 32

3.2 Comparison of cosmological parameters 43

5.1 Definition of the four choices of parameter sets used to show a change in the duration of reheating generated by a fluctuation δm_χ^2 97

Chapter 1

Introduction

We live in exciting times for the study of our Universe. Measurements of the Cosmic Microwave Background radiation (CMB) [1], in combination with other important astrophysical observations such as galaxy surveys [2] and the study of Type Ia supernovae [3], have opened an era of precision cosmology. These advances in observational cosmology have led to the establishment of the cosmological standard model [4]. We have compelling evidence about the energy budget of the Universe. On the other hand, we only understand 5% of it! This 5% is composed of matter explained by the standard model of particle physics. The rest is known as the dark sector; 25% consists of dark matter and the remaining 70% is made of dark energy–a negative pressure component responsible for the current acceleration of the Universe.

Of particular relevance has been the measurements of the CMB. The CMB gives us information from the snapshot of the Universe's history when it was cool enough for atoms to form and for photons to decouple and propagate freely. Observations of the CMB have allowed us to measure a uniform temperature of the background radiation to one part in 10^{-5}. These tiny perturbations are the seeds which grow with the help of gravity to form the galactic structures that we observe today. The detection and analysis of these fluctuations have been fundamental not only

in understanding the epoch of recombination, but also in establishing the standard cosmological model.

The leading contender to explain the almost-uniform-temperature of the CMB, as well as to provide a mechanism for the generation of the small inhomogeneities, is inflation [5, 6]. The epoch of inflation is characterized by accelerated expansion of the Universe. As a consequence of this, vacuum fluctuations in a light scalar field are pushed outside the Hubble radius. These fluctuations re-enter the Hubble radius at a later time and imprint an approximately scale-invariant spectrum of classical density perturbations [7].

In spite of the remarkable advances in the understanding of the Cosmos, many questions remain unanswered. For example, what is the nature of dark energy; what is dark matter made of; what is the theory behind inflation and the density perturbations? The underlying physics of the standard cosmological model is still unknown.

Of the many unanswered questions about the physics of the Universe, in this thesis we examine (i) the consequences that a preferred direction during the inflationary era would have on the CMB anisotropies, (ii) the effect of asymmetric beams in the Wilkinson Microwave Anisotropy Probe (WMAP), (iii) astrophysical consequences of a dark photon that couples only to the dark matter and, (iv) explore a mechanism for producing density perturbations during the period of reheating.

1.1 Imprints of a Primordial Preferred Direction on the Microwave Background

In science it is essential to question the untested assumptions. If density perturbations do arise from inflation, they provide a window to very high energies. An upper limit on the energy scale of inflation ($E \sim V^{1/4}$) can be found by noting that it is typically related to the amplitude of scalar perturbations, $\Delta^2_{\mathcal{R}}$, and the reduced Planck mass via $E < (\Delta^2_{\mathcal{R}})^{1/4} M_P$. As we observe $\Delta^2_{\mathcal{R}} = (2.445 \pm 0.096) \times 10^{-9}$ at $k = 0.002$ Mpc^{-1} [1], it is plausible that inflation occurs only a few orders of magnitude below the Planck scale. At those energies we don't have many experimental constraints and it is reasonable to keep an open mind about the physics in play during inflation.

In chapter 2 we study the effects that a preferred direction during the inflationary era would have on the CMB anisotropies. If such breaking of rotational invariance had occurred, then the primordial power spectrum of the density perturbations would not only depend on the wavelength of the perturbations, but also on the angle between a given wave-vector and the preferred direction. For the case of a small breaking of rotational invariance, we find the general form of the power spectrum and compute explicit expressions for the amplitudes of the spherical-harmonic coefficients. We suggest that it is reasonable to expect that the imprints on the primordial power spectrum of a preferred spatial direction are approximately scale invariant.

1.2 Preliminary Investigation on the Effect of Asymmetric Beams in the Wilkinson Microwave Anisotropy Probe Experiment

An experiment observes the CMB by scanning the sky with an instrumental beam of finite resolution. This operation effectively corresponds to averaging over beam-sized angular scales, and is expressed either in pixel space by a convolution of the beam with the underlying sky, or in harmonic space by a multiplication of the two corresponding sets of harmonic expansion coefficients. For simplicity, the harmonic space expansion of the beam is typically expressed in terms of Legendre coefficients of an (azimuthally symmetric) effective beam response. This function is often called "the beam transfer function".

Understanding the effects of the detector and scanning strategy are important to make cosmological inferences from the CMB power spectrum. Chapter 3 has two parts. First, we produce by direct simulation CMB sky maps that take into account the effects of the WMAP beams being asymmetric as well as the WMAP scanning strategy. Second, we estimate the effective beam transfer function for each of the WMAP detectors.

1.3 Dark Matter and Dark Radiation

Overwhelming evidence points to the existence of dark matter, and a promising candidate for dark matter is a WIMP: a stable, neutral particle with weak-scale couplings and mass. Particles of this type arise in models that aim to solve the hierarchy problem, i.e. supersymmetry [12] and theories of extra dimensions [13].

The weak-scale cross-section of such WIMPs provides a natural way to obtain the measured relic abundance of dark matter, but it is important to remember that we still do not know what the dark matter is.

In chapter 4 we explore the astrophysical consequences of an unbroken U(1) force that couples only to the dark matter. An interesting aspect of this model is that interactions between dark particles exist, even though the halo is overall neutral. Current observations suggest that the dark matter is effectively collisionless, which constrains the parameters of the model. For TeV-scale dark matter, this implies that the dark fine-structure constant must be less than or equal to 10^{-3}. A consequence of this constraint is that one cannot build a dark matter model with a hidden unbroken U(1) in which this interaction alone is responsible for the observed dark matter relic abundance. One could introduce other interactions in addition to the dark U(1) gauge group that would increase the annihilation cross-section and, in that way, obtain the correct freeze-out density. We investigate the possibility of coupling the dark matter to the usual weak-interactions, as well as charging it under an unbroken U(1). Near the upper limit of the galactic dynamics bound important effects on galactic structure might occur. It has been suggested that alterations to the dark halo shapes, which our model would have, may actually lead to better agreement with observations [14]. On the other hand, we also point out that there are plasma instabilities that may play an important role in the assembly of galactic halos and may further constrain this model.

1.4 Light Scalars and the Generation of Density Perturbations During Preheating or Inflaton Decay

After inflation, a period of reheating is necessary to set up the hot big bang evolution. This reheating process can occur through inflaton decay and also through coherent oscillations of the inflaton field that increases the energy density in the decay products exponentially.

In chapter 5 we explore the scenario where the particles produced during reheating interact with scalars that were light during inflation. The fluctuations acquired by the light fields during inflation modify the time it takes for reheating to be completed. As the energy density in matter redshifts slower than the energy density in radiation, regions of the Universe where reheating takes longer to complete stay matter-dominated longer and will be denser. We find that significant density perturbations can be generated during reheating and, furthermore, that these perturbations can be highly non-Gaussian.

The work presented in chapter 2 was completed in collaboration with Sean M. Carroll and Mark B. Wise and has been published as [8]. Chapter 3 is the result of a collaboration with Ingunn Kathrine Wehus, H. K. Eriksen, and Nicolaas E. Groeneboom and has been submitted for publication in *The Astrophysical Journal*. The discussion presented in chapter 4 is the result of work done in conjunction with Matthew R. Buckley, Sean M. Carroll, and Marc Kamionkowski and has appeared in [9]. Chapter 5 was previously published as [10] and was coauthored with Christian W. Bauer, Michael L. Graesser, and Mark B. Wise.

Chapter 2

Imprints of a Primordial Preferred Direction on the Microwave Background

2.1 Introduction

Inflationary cosmology, originally proposed as a solution to the horizon, flatness, and monopole problems [5, 6], provides a very successful mechanism for generating primordial density perturbations. During inflation, quantum vacuum fluctuations in a light scalar field are redshifted far outside the Hubble radius, imprinting an approximately scale-invariant spectrum of classical density perturbations [7, 15]. Models that realize this scenario have been widely discussed [16, 17, 18]. The resulting perturbations give rise to galaxy formation and temperature anisotropies in the cosmic microwave background, in excellent agreement with observation [19, 20, 21, 22, 23, 24, 25, 26, 27, 28].

If density perturbations do arise from inflation, they provide a unique window on physics at otherwise inaccessible energy scales. In a typical inflationary model (although certainly not in all of them), the energy scale $E = V^{1/4}$ is related to the amplitude of density fluctuations δ and the reduced Planck mass $M_{\rm P}$ via $E \sim \sqrt{\delta} M_{\rm P}$.

Since we observe $\delta \sim 10^{-5}$, it is very plausible that inflation occurs near the scale of grand unification, and not too far from scales where quantum gravity is relevant. Since direct experimental probes provide very few constraints on physics at such energies, it makes sense to be open-minded about what might happen during the inflationary era.

In this paper we ask what happens when a cherished property of low-energy physics – rotational invariance – is violated during inflation. Rotational invariance is of course a subset of Lorentz invariance, and theoretical models of Lorentz violation in the current universe (and experimental constraints thereon) have been extensively studied in recent years [29, 30, 31, 32, 33]. Here we are specifically concerned with the possibility that rotational invariance may have been broken during inflation by an effect that has subsequently disappeared, and study the effects of such breaking on CMB anisotropies. It is possible that such an effect has already been detected, in the form of the "Axis of Evil," an apparent alignment of the CMB multipoles on very large scales [34, 35, 36, 37, 38, 39, 40, 41, 42, 43, 44, 45, 46, 47, 48, 49, 50, 51, 52, 53, 54]. Although its statistical significance is hard to quantify, a variety of models have been put forward to explain this phenomenon [55, 56, 57, 58, 59, 60, 61, 62, 63, 64]. Our aim is not to construct a model contrived to explain the currently observed large-scale anomalies, but rather to make robust predictions for the observable consequences of a preferred direction during inflation, allowing observations to put constraints on its magnitude.

The power spectrum $P(k)$ for the primordial density perturbations $\delta(\mathbf{k})$ is defined by

$$\langle \delta(\mathbf{k}) \delta^*(\mathbf{q}) \rangle = P(k) \delta^3(\mathbf{k} - \mathbf{q}). \tag{2.1}$$

The Dirac delta function in Eq. (2.1) implies that modes with different wavenumbers are uncoupled, and is a consequence of translational invariance during the inflationary era. On the other hand, the fact that the power spectrum $P(k)$ only depends on the magnitude of the vector $\mathbf{k}$ is a consequence of rotational invariance. Suppose that during the inflationary era rotational invariance is broken by the presence of a small vector that points in the direction of a unit vector $\mathbf{n}$. Assuming a parity $\mathbf{k} \to -\mathbf{k}$ symmetry, the leading effect of the violation of rotational invariance changes the most general form of the power spectrum from $P(k)$ to $P'(\mathbf{k})$, where

$$P'(\mathbf{k}) = P(k) \left(1 + g(k)(\hat{\mathbf{k}} \cdot \mathbf{n})^2\right). \tag{2.2}$$

Here $\hat{\mathbf{k}}$ is the unit vector along the direction of $\mathbf{k}$ and we are neglecting higher powers of $\hat{\mathbf{k}} \cdot \mathbf{n}$ since they will be suppressed by more powers of the magnitude of the small vector that breaks rotational invariance. (Effects of a *timelike* vector on inflationary perturbations have also been studied [65].)

Towards the end of the inflationary era, the physical wavelengths that correspond to scales of astrophysical interest are large compared with the inverse Hubble constant during inflation or any of the dimensionful particle-physics quantities that might be relevant during inflation. The same naturalness arguments that lead to the scale-invariant Harrison-Zeldovich spectrum (i.e., primordial $P(k) \propto 1/k^3$) imply that $g(k)$ in Eq. (2.2) should be independent of k. Assuming that $g(k)$ is a k-independent constant g_* over the scales of astrophysical interest, we arrive at

$$P'(\mathbf{k}) = P(k) \left(1 + g_*(\hat{\mathbf{k}} \cdot \mathbf{n})^2\right). \tag{2.3}$$

This is the form of the primordial power spectrum that takes into account the leading effects of the violation of rotational invariance by a small vector in the inflationary era that points in the direction **n**. In the next section we discuss the implications of the power spectrum in Eqs. (2.2) and (2.3) for the anisotropy of the microwave background radiation. The breaking of rotational invariance gives rise to correlations between multipole moments that would normally vanish and also alters the predictions for the usual multipole moment correlations. In section three we discuss a simple model that realizes the form of the primordial power spectrum in Eq. (2.3). Concluding remarks are given in section four.

2.2 Microwave Background

We are interested in a quantitative understanding of how the substitution, $P(k) \to P'(\mathbf{k})$, changes the prediction for the microwave background anisotropy $\Delta T/T$. The multipole moments are defined by

$$a_{lm} = \int \mathrm{d}\Omega_{\mathbf{e}} (Y_l^m(\mathbf{e}))^* \frac{\Delta T}{T}(\mathbf{e}). \tag{2.4}$$

The anisotropy of the microwave background temperature T along the direction of the unit vector $\mathbf{e}$ is related to the primordial fluctuations by

$$\frac{\Delta T}{T}(\mathbf{e}) = \int \mathrm{d}\mathbf{k} \sum_l \left(\frac{2l+1}{4\pi}\right) (-i)^l P_l(\hat{\mathbf{k}} \cdot \mathbf{e}) \delta(\mathbf{k}) \Theta_l(k), \tag{2.5}$$

where P_l is the Legendre polynomial of order l and $\Theta_l(k)$ is a function of the magnitude of the wave-vector $\mathbf{k}$ that includes, for example, the effects of the transfer

function. It can only depend on the magnitude of the wave-vector since the dynamics after the inflationary era is assumed to be rotationally invariant.

We would like to compute the expectation values $\langle a_{lm} a^*_{l'm'} \rangle$ to first order in the small quantity $g(k)$ that characterizes the primordial violation of rotational invariance. We write

$$\langle a_{lm} a^*_{l'm'} \rangle = \langle a_{lm} a^*_{l'm'} \rangle_0 + \Delta(lm; l'm'), \tag{2.6}$$

where the subscript 0 denotes the usual rotationally invariant piece,

$$\langle a_{lm} a^*_{l'm'} \rangle_0 = \delta_{ll'} \delta_{mm'} \int_0^\infty \mathrm{d}k k^2 P(k) \Theta_l(k)^2. \tag{2.7}$$

It is useful to introduce the "spherical" components of the unit vector $\mathbf{n}$ that defines the preferred direction for rotational non-invariance,

$$n_+ = -\left(\frac{n_x - i n_y}{\sqrt{2}} \right), \; n_- = \left(\frac{n_x + i n_y}{\sqrt{2}} \right), \; n_0 = n_z. \tag{2.8}$$

In terms of these components, the unit norm condition becomes $n_0^2 - 2 n_+ n_- = 1$. Note that we do not assume that the preferred direction $\mathbf{n}$ coincides with the $\hat{\mathbf{z}}$ axis of the coordinate system used to parameterize the microwave sky (i.e., that $n_+ = n_- = 0$). Expressions analogous to ours have been derived by Gümrükçüoğlu et al. [64] under the assumption that these two directions are coincident; see also [49].

Using the identity

$$P_l(\hat{\mathbf{k}}\cdot\mathbf{e}) = \frac{4\pi}{2l+1}\sum_{m=-l}^{l} Y_l^m(\mathbf{e})(Y_l^m(\hat{\mathbf{k}}))^*, \tag{2.9}$$

it is straightforward to express the sought-after perturbation as

$$\Delta(lm;l'm') = (-i)^{l-l'}\xi_{lm;l'm'}\int_0^\infty \mathrm{d}k k^2 P(k) g(k)\Theta_l(k)\Theta_{l'}(k), \tag{2.10}$$

where [1]

$$\begin{aligned}\xi_{lm;l'm'} &= \frac{4\pi}{3}\int \mathrm{d}\Omega_{\mathbf{k}}(Y_l^m(\hat{\mathbf{k}}))^* Y_{l'}^{m'}(\hat{\mathbf{k}}) \\ &\quad\times\left(n_+ Y_1^1(\hat{\mathbf{k}}) + n_- Y_1^{-1}(\hat{\mathbf{k}}) + n_0 Y_1^0(\hat{\mathbf{k}})\right)^2.\end{aligned} \tag{2.11}$$

The integral in (2.10) encodes information about the power spectrum and the transfer function, as well as the scale-dependence of the preferred-direction effect, while the constants $\xi_{lm;l'm'}$ are purely geometric. The integration over solid angles is straightforward to perform. It is convenient to decompose the $\xi_{lm;l'm'}$ into coefficients of the quadratic quantities $n_i n_j$, via

$$\begin{aligned}\xi_{lm;l'm'} &= n_+^2\xi_{lm;l'm'}^{++} + n_-^2\xi_{lm;l'm'}^{--} + 2n_+n_-\xi_{lm;l'm'}^{+-} \\ &\quad + 2n_+n_0\xi_{lm;l'm'}^{+0} + 2n_-n_0\xi_{lm;l'm'}^{-0} + n_0^2\xi_{lm;l'm'}^{00}.\end{aligned} \tag{2.12}$$

These coefficients are then given by the following expressions:

[1] We use the Condon-Shortley phase convention for the spherical harmonics. See [66]

$$
\begin{aligned}
\xi^{--}_{lm;l'm'} &= -\delta_{m',m+2}\left[\delta_{l',l}\frac{\sqrt{(l^2-(m+1)^2)(l+m+2)(l-m)}}{(2l+3)(2l-1)}\right.\\
&\quad -\frac{1}{2}\delta_{l',l+2}\sqrt{\frac{(l+m+1)(l+m+2)(l+m+3)(l+m+4)}{(2l+1)(2l+3)^2(2l+5)}}\\
&\quad \left.-\frac{1}{2}\delta_{l',l-2}\sqrt{\frac{(l-m)(l-m-1)(l-m-2)(l-m-3)}{(2l+1)(2l-1)^2(2l-3)}}\right],\\
\xi^{++}_{lm;l'm'} &= \xi^{--}_{l'm';lm},\\
\xi^{+-}_{lm;l'm'} &= \frac{1}{2}\delta_{m',m}\left[-2\,\delta_{l',l}\frac{(-1+l+l^2+m^2)}{(2l-1)(2l+3)}+\delta_{l',l+2}\sqrt{\frac{((l+1)^2-m^2)((l+2)^2-m^2)}{(2l+1)(2l+3)^2(2l+5)}}\right.\\
&\quad \left.+\,\delta_{l',l-2}\sqrt{\frac{(l^2-m^2)((l-1)^2-m^2)}{(2l-3)(2l-1)^2(2l+1)}}\right],\\
\xi^{-0}_{lm;l'm'} &= -\frac{1}{\sqrt{2}}\delta_{m',m+1}\left[\delta_{l',l}\frac{(2m+1)\sqrt{(l+m+1)(l-m)}}{(2l-1)(2l+3)}\right.\\
&\quad +\,\delta_{l',l+2}\sqrt{\frac{((l+1)^2-m^2)(l+m+2)(l+m+3)}{(2l+1)(2l+3)^2(2l+5)}}\\
&\quad \left.-\,\delta_{l',l-2}\sqrt{\frac{(l^2-m^2)(l-m-1)(l-m-2)}{(2l-3)(2l-1)^2(2l+1)}}\right],\\
\xi^{+0}_{lm;l'm'} &= -\xi^{-0}_{l'm';lm},\\
\xi^{00}_{lm;l'm'} &= \delta_{m,m'}\left[\delta_{l,l'}\frac{(2l^2+2l-2m^2-1)}{(2l-1)(2l+3)}+\delta_{l',l+2}\sqrt{\frac{((l+1)^2-m^2)((l+2)^2-m^2)}{(2l+1)(2l+3)^2(2l+5)}}\right.\\
&\quad \left.+\delta_{l',l-2}\sqrt{\frac{(l^2-m^2)((l-1)^2-m^2)}{(2l-3)(2l-1)^2(2l+1))}}\right]. \qquad (2.13)
\end{aligned}
$$

The formulas (2.12, 2.13) are explicit expressions for the geometrical part of the perturbation (2.10). As we mentioned in the introduction, it is natural to imagine that the violation of rotational invariance is approximately scale invariant, which implies that it is a good approximation to set $g(k) = g_*$, a constant. If we define

polar coordinates θ_*, ϕ_* for the preferred direction,

$$n_x = \sin\theta_* \cos\phi_* \, , \; n_y = \sin\theta_* \sin\phi_* \, , \; n_z = \cos\theta_* \, , \tag{2.14}$$

these expressions can be compared directly with observations to constrain the three parameters (g_*, θ_*, ϕ_*).

When $g(k) = g_*$, a simplification occurs for $l = l'$ and $m = m'$, as the dependence on the power spectrum for the terms that violate rotational invariance $\Delta(lm; lm)$ is the same as the rotationally-invariant part $\langle a_{lm} a^*_{lm} \rangle_0$. We can then find a simple expression for their ratio,

$$\begin{aligned} \frac{\Delta(lm;lm)}{\langle a_{lm} a^*_{lm} \rangle_0} &= \frac{g_*}{2} \Bigg[\sin^2\theta_* + \\ &\qquad (3\cos^2\theta_* - 1) \left(\frac{2l^2 + 2l - 2m^2 - 1}{(2l-1)(2l+3)} \right) \Bigg] . \end{aligned} \tag{2.15}$$

For large multipoles, $l \gg 1$, and for the magnitude of m of the order of l, this expression simplifies to

$$\frac{\Delta(lm;lm)}{\langle a_{lm} a^*_{lm} \rangle_0} = \frac{g_*}{4} \left[1 + \cos^2\theta_* - (3\cos^2\theta_* - 1) \frac{m^2}{l^2} \right] . \tag{2.16}$$

2.3 Inflation Model with a Preferred Direction

It is interesting to see how the rotationally non-invariant power spectrum in Eq. (2.3) can arise in an explicit model of anisotropic inflation. We will assume that, during most of the inflationary era, rotational invariance is broken by a spacelike four-vector

u^μ with invariant length

$$g_{\mu\nu}u^\mu u^\nu = m^2. \tag{2.17}$$

We will consider the effect of the energy-momentum tensor associated with this vector on the expansion of the universe during inflation, ignoring direct couplings of u^μ to other fields. Gravitational effects of dynamical Lorentz-violating vector fields have been considered previously in the literature [68, 69, 70, 71, 72, 73].

We assume that the four-vector u^μ is non-zero only during the time interval $0 < t < t_*$, where t_* is the end of inflation, so that the dynamics is rotationally invariant during reheating and thereafter. During the time interval $0 < t < t_*$, the dynamics of interest is governed by the action

$$S = \int \mathrm{d}^4x\sqrt{-}g\left(\frac{1}{16\pi G}R - \rho_\Lambda + \mathcal{L}_u + \mathcal{L}_\chi\right), \tag{2.18}$$

where

$$\mathcal{L}_\chi = -\frac{1}{2}g^{\mu\nu}\partial_\mu\chi\partial_\nu\chi \tag{2.19}$$

and

$$\begin{aligned}\mathcal{L}_u &= -\beta_1\nabla^\mu u^\sigma\nabla_\mu u_\sigma - \beta_2(\nabla_\mu u^\mu)^2 \\ &\quad -\beta_3\nabla^\mu u^\sigma\nabla_\sigma u_\mu + \lambda(u^\mu u_\mu - m^2)\ .\end{aligned} \tag{2.20}$$

Here λ is a Lagrange multiplier that enforces the constraint (2.17). Quantum fluctuations in the massless scalar field χ are assumed to dominate the density perturbations via the DGZK mechanism [67]. In that case we need simply calculate the fluctuations in χ, without worrying about the behavior of the inflationary potential.

We approximate the inflaton energy density as a constant, modeling the effects of the inflaton field by a vacuum energy ρ_Λ in Eq. (2.18). The inflationary spacetime is taken of the form

$$\mathrm{d}s^2 = -\mathrm{d}t^2 + a(t)^2 \mathrm{d}\mathbf{x}_\perp^2 + b(t)^2 \mathrm{d}z^2 \tag{2.21}$$

since we have chosen the four-vector to be aligned along the z-axis direction,

$$u^0 = 0 \ \ , u^x = 0 \ \ , u^y = 0 \ \ , u^z = \frac{m}{b(t)}. \tag{2.22}$$

The energy-momentum tensor for u^μ derived from (2.20) is [71]

$$\begin{aligned} T^{(u)}_{\mu\nu} &= 2\beta_1(\nabla_\mu u^\rho \nabla_\nu u_\rho - \nabla^\rho u_\mu \nabla_\rho u_\nu) \\ &\quad -2[\nabla_\rho(u_{(\mu} J^\rho{}_{\nu)}) + \nabla_\rho(u^\rho J_{(\mu\nu)}) - \nabla_\rho(u_{(\mu} J_{\nu)}{}^\rho)] \\ &\quad +2m^{-2} u_\sigma \nabla_\rho J^{\rho\sigma} u_\mu u_\nu + g_{\mu\nu}\mathcal{L}_u, \end{aligned} \tag{2.23}$$

where $J^\mu{}_\sigma$ is the current tensor,

$$J^\mu{}_\sigma = -\beta_1 \nabla^\mu u_\sigma - \beta_2 \, \delta^\mu_\sigma \, \nabla_\rho u^\rho - \beta_3 \nabla_\sigma u^\mu.$$

Given Eqs. (2.22) and (2.23), the nonvanishing components of the stress tensor

are

$$\begin{aligned} T^{(u)}_{00} &= \beta_1 m^2 \left(\frac{\dot{b}}{b}\right)^2 \\ T^{(u)}_{xx} &= T_{yy} = \beta_1 m^2 a^2 \left(\frac{\dot{b}}{b}\right)^2 \\ T^{(u)}_{zz} &= \beta_1 m^2 \left(\dot{b}^2 - 2\ddot{b}b - 4\frac{\dot{a}\dot{b}b}{a}\right). \end{aligned} \tag{2.24}$$

Note that the components of the energy momentum tensor in our chosen background are independent of β_2 and β_3.

Solving Einstein's equation during the time interval $0 < t < t_*$, with initial conditions $a(0) = 1$ and $b(0) = 1$, gives

$$a(t) = e^{H_a t}, \quad b(t) = e^{H_b t}, \tag{2.25}$$

where

$$\begin{aligned} H_a &= \frac{\dot{a}}{a} = H_b(1 + 16\pi G\beta_1 m^2), \\ H_b &= \frac{\dot{b}}{b} = \sqrt{\frac{8\pi G\rho_\Lambda}{(1 + 8\pi G\beta_1 m^2)(3 + 32\pi G\beta_1 m^2)}}. \end{aligned} \tag{2.26}$$

According to the cosmic no-hair theorem, initially expanding homogeneous cosmological models in the presence of a positive cosmological constant will rapidly approach a de Sitter solution, if the other matter fields obey the dominant and strong energy conditions [74]. Our specific model violates these conditions. Nevertheless, for $\beta_3 = -\beta_1$ and $\beta_2 = 0$ the kinetic term for fluctuations about our background has the form of a field strength tensor squared and so is ghost free. We

therefore expect the configuration to be stable with respect to small fluctuations.

It will turn out to be convenient to refer to a fictitious isotropic metric,

$$\mathrm{d}\bar{s}^2 = -\mathrm{d}t^2 + \bar{a}(t)^2[\mathrm{d}x^2 + \mathrm{d}y^2 + \mathrm{d}z^2], \tag{2.27}$$

in which the scale factor expands exponentially

$$\bar{a}(t) = e^{\bar{H}t} \tag{2.28}$$

with an "average" Hubble parameter,

$$\bar{H} = \frac{1}{3}(2H_a + H_b). \tag{2.29}$$

Deviations from isotropy can be parameterized by

$$\epsilon_H = \frac{2}{3}\left(\frac{H_b - H_a}{\bar{H}}\right), \tag{2.30}$$

where the 2/3 will become useful later. We work in the limit $N_*|\epsilon_H| << 1$, where $N_* = \bar{H}t_*$ is the number of e-foldings during the time when the four-vector u^μ is non-zero. This assures that the violation of rotational invariance due to the anisotropic expansion is always a small perturbation.

We need to compute the correlation function $\langle\chi(\mathbf{x},t)\chi(\mathbf{y},t)\rangle$. Treating ϵ_H as a small perturbation, we find that to first order in this quantity we obtain (i.e. ref.

[75])

$$\begin{aligned}\langle\chi(\mathbf{x},t)\chi(\mathbf{y},t)\rangle &\simeq \langle\chi_I(\mathbf{x},t)\chi_I(\mathbf{y},t)\rangle \\ &\quad +i\int_0^t \mathrm{d}t'\langle[H_I(t'),\chi_I(\mathbf{x},t)\chi_I(\mathbf{y},t)]\rangle.\end{aligned} \tag{2.31}$$

Here the interaction-picture Hamiltonian $H_I(t)$ is given by

$$\begin{aligned}H_I(t) &= \int \mathrm{d}^3x\frac{1}{2}\left[(b(t)-\bar{a}(t))\left(\frac{\mathrm{d}\chi_I}{d\mathbf{x}_\perp}\right)^2\right. \\ &\quad \left.+\left(\frac{a(t)^2}{b(t)}-\bar{a}(t)\right)\left(\frac{\mathrm{d}\chi_I}{dx^3}\right)^2\right].\end{aligned} \tag{2.32}$$

The interaction-picture (i.e., free) field obeys the rotationally-invariant equation of motion,

$$\frac{\mathrm{d}^2\chi_I}{\mathrm{d}t^2}+3\bar{H}\frac{\mathrm{d}\chi_I}{\mathrm{d}t}-\frac{1}{\bar{a}(t)^2}\frac{\mathrm{d}^2\chi_I}{\mathrm{d}\mathbf{x}^2}=0. \tag{2.33}$$

We can write the two-point correlation function (2.32) in terms of Fourier transforms as

$$\begin{aligned}\langle\chi(\mathbf{x},t)\chi(\mathbf{y},t)\rangle &= \int\frac{\mathrm{d}^3k}{(2\pi)^3}e^{-i\mathbf{k}\cdot(\mathbf{x}-\mathbf{y})}\left[P(k)\right. \\ &\quad \left.+(\hat{\mathbf{k}}\cdot\mathbf{n})^2\Delta P(k)\right].\end{aligned} \tag{2.34}$$

Converting to the conformal time of the isotropic metric,

$$\tau=-\frac{1}{\bar{H}}e^{-\bar{H}t}, \tag{2.35}$$

and expanding in ϵ_H, we find that $P(k) \simeq |\chi_k^{(0)}(\tau)|^2$, and

$$\Delta P(k) \simeq 3ik^2\epsilon_H \int_{-1/\bar{H}}^{\tau} \mathrm{d}\tau' \left(-\frac{1}{\bar{H}\tau'}\right)^2 \times \log(-\bar{H}\tau') \left[(\chi_k^{(0)}(\tau')\chi_k^{(0)}(\tau)^*)^2 - (\chi_k^{(0)}(\tau')^*\chi_k^{(0)}(\tau))^2\right], \tag{2.36}$$

where

$$\chi_k^{(0)}(\tau) = \frac{\bar{H}}{\sqrt{2k}} e^{-ik\tau}\left[\tau - \frac{i}{k}\right]. \tag{2.37}$$

We assume that the modes k of astrophysical interest have wavelengths much smaller than the Hubble radius at the beginning of inflation, which in our normalization implies $k >> \bar{H}$. They cross the horizon around sixty e-foldings before the end of inflation (which we take to occur at about t_*). Taking $|k\tau| << 1$, we find that

$$\Delta P(k) \simeq \frac{9}{4}\epsilon_H \frac{\bar{H}^2}{k^3}\log(k/\bar{H}), \tag{2.38}$$

where we have neglected contributions not enhanced by the large logarithm.

There is another way to derive Eq. (2.38). For modes with wavenumbers along the $\hat{\mathbf{z}}$ direction or perpendicular to this direction, the Fourier transform of the two point function $\langle\chi(\mathbf{x},t)\chi(\mathbf{y},t)\rangle$ can be found exactly without resorting to perturbation theory. For example, modes χ_k with $\mathbf{k} = k\hat{\mathbf{z}}$ (wavevectors parallel to the preferred direction) obey the differential equation

$$\frac{\mathrm{d}^2\chi_k}{\mathrm{d}t^2} + 3\bar{H}\frac{\mathrm{d}\chi_k}{\mathrm{d}t} + \frac{k^2}{b(t)^2}\chi_k = 0. \tag{2.39}$$

The canonical commutation relations imply that χ_k satisfies the normalization con-

dition,

$$\left(\frac{\mathrm{d}\chi_k(\tau)}{\mathrm{d}\tau}\right)\chi_k(\tau)^* - \left(\frac{\mathrm{d}\chi_k(\tau)^*}{\mathrm{d}\tau}\right)\chi_k(\tau) = -i(\bar{H}\tau)^2. \tag{2.40}$$

We find that the properly normalized solution to Eq. (2.39) is

$$\chi_k(\tau) = \frac{\bar{H}\sqrt{\pi}\tau^{3/2}}{2\sqrt{1+\epsilon_H}} H_\nu^{(2)}\left(\frac{(k/\bar{H})^{-\epsilon_H}(k\tau)^{1+\epsilon_H}}{1+\epsilon_H}\right), \tag{2.41}$$

where $H_\nu^{(2)}$ is a Hankel function, and

$$\nu = \frac{3}{2+2\epsilon_H}. \tag{2.42}$$

The contribution to the Fourier transform of the two point χ correlation for a mode along the $\hat{\mathbf{z}}$ direction is $|\chi_k(\tau)|^2$. For small ϵ_H and $|k\tau|$ and large $k/\bar{H}$, this becomes

$$|\chi_k(\tau)|^2 \simeq \frac{\bar{H}^2}{2k^3}\left(1 + 3\epsilon_H \log(k/\bar{H})\right). \tag{2.43}$$

Here we have neglected terms linear in ϵ_H that are not enhanced by the large logarithm. Combining this result with a similar analysis for modes perpendicular to the $\hat{\mathbf{z}}$ direction reproduces the result in Eq. (2.38).

Finally we note that the density perturbation power spectrum is defined by a Fourier transform with respect to coordinates where physical laws have manifest rotational invariance. However at time $t = t_*$, the coordinates in Eq. (2.21) do not exhibit manifest rotational invariance due to the difference between $a(t_*)$ and $b(t_*)$. Rescaling coordinates, $z \to z(\bar{a}(t_*)/b(t_*))$ and $\mathbf{x}_\perp \to \mathbf{x}_\perp(\bar{a}(t_*)/a(t_*))$, we find that the function $g(k)$ characterizing the rotationally non-invariant part of the power

spectrum for the primordial density perturbations is

$$\begin{aligned} g(k) &= \frac{9}{2}\epsilon_H(\log(k/\bar{H}) - N_*) \\ &= \frac{9}{2}\epsilon_H \log(q(t_*)/\bar{H}), \end{aligned} \tag{2.44}$$

where the term proportional to N_* comes from the rescaling of coordinates and $q(t_*) = k/\bar{a}(t_*)$ is the physical wavelength of the mode of interest at the end of inflation.

The logarithm in (2.44) is actually nearly constant over values of $q(t_*)$ of astrophysical interest. The range of $q(t_*)$ probed by CMB measurements is about a factor of 10^3, so $\log(q(t_*)/\bar{H})$ changes by roughly 7. But the modes of cosmological interest cross the deSitter horizon around 60 e-foldings before the end of inflation. So $|\log(q(t_*)/\bar{H})|$ is approximately 60. Hence, in this model $g(k)$ varies by about 10% over the range of modes of cosmological interest and our general expectation that setting $g(k) = g_*$ is a reasonable approximation has been confirmed.

For simplicity in this analysis we neglected terms that directly couple u^μ to χ. For example, we could have added the term $u^\mu u^\nu \partial_\mu \chi \partial_\nu \chi / M^2$ to the Lagrange density. It is easy to see that this gives an additional scale invariant contribution, $3m^2/M^2$, to $g(k)$.

2.4 Concluding Remarks

We have investigated the possibility that rotational invariance may have been explicitly broken during inflation by an effect that has disappeared in the later universe. The observed CMB temperature anisotropies provide a direct window onto

the physics of the inflationary era, and therefore offer a unique opportunity for constraining (and discovering) new phenomena at high scales. Our aim has been to investigate the generic predictions we expect from the presence of a preferred direction during inflation.

If rotational invariance is violated during inflation, it is natural for the effects of such a violation to show up in a scale-invariant way, just as the amplitude of the perturbations themselves are approximately scale-invariant. Under that assumption, we derive a powerful set of predictions for the expectation values $\langle a_{lm} a^*_{l'm'} \rangle$ that depend on only three parameters: a single amplitude g_*, and a direction on the sky defined by a unit vector $\mathbf{n}$. Investigation of a simple model confirms the approximate scale-independence of this effect. The resulting expressions (2.10,2.12,2.13) can be directly compared with observations to probe the existence of small Lorentz-violating effects in the very early Universe.

Chapter 3

Preliminary Investigation on the Effect of Asymmetric Beams in the Wilkinson Microwave Anisotropy Probe Experiment

3.1 Introduction

Without doubt, the angular CMB power spectrum is today our single most important source of cosmological information. Perhaps the most striking demonstration of this fact to date is the WMAP experiment, [77, 28, 86] which has allowed cosmologists to put unprecedented constraints on all main cosmological parameters, as well as ruling out vast regions of the possible model spaces. Similarly, in only a few years from now Planck will finally provide the definitive measurements of the temperature power spectrum, as well as polarization spectra with unprecedented accuracy. This will certainly lead to similar advances in our knowledge about the history of our universe.

Each of these experiments observes the CMB field by scanning the sky with an instrumental beam of finite resolution. This operation effectively corresponds to averaging over beam-sized angular scales, and is expressed technically either in pixel

space by a convolution of the beam with the underlying sky, or in harmonic space by multiplication of the two corresponding sets of harmonic expansion coefficients. For simplicity, the harmonic space expansion of the beam is typically expressed in terms of Legendre coefficients of an (azimuthally symmetric) effective beam response. This function is often called "the beam transfer function", b_ℓ.

Before it is possible to make unbiased cosmological inferences based on the CMB power spectrum, it is of critical importance to know the beam transfer function to high precision, as an error in the beam function translates into a direct bias in the estimated power spectrum. This in turn requires detailed knowledge about the beam response function on the sky for each experiment. For a full description of the WMAP beam estimation process and final model, see [92], [89], and [84].

The impact of asymmetric beams may also be important for applications other than power spectrum estimation. One example of special interest to us is the assessment of non-Gaussianity and violation of statistical isotropy. Specifically, [76] considered a model based on violation of rotational invariance in the early universe, and derived explicit parametric expressions for the corresponding observational signature. Then, in a follow-up paper [82] analysed the 5-year WMAP data with respect to this model and, most surprisingly, found a detection at the 3.8σ confidence level. Given that this was a most unexpected result, several questions concerning systematic errors in the WMAP data were considered, in particular those due to residual foregrounds, correlated noise and asymmetric beams. However, it was shown in the same paper that neither foregrounds nor correlated noise were viable explanations, while the question of asymmetric beams was left unanswered, due to a lack of proper simulation machinery. This question provided our initial motivation for considering

the problems studied in this chapter.

The starting point for tackling the asymmetric beam problem for WMAP is a set of beam maps released by the WMAP team, two for each differencing assembly (DA), denoted A and B, respectively. These maps were derived by observing Jupiter for extended periods of time. Then, in order to derive the proper beam transfer functions, the WMAP team adopted a computationally fast and convenient approach: They first symmetrized the effective beam for each DA, collapsing the information in the A and B sides into one common function, and then computed the Legendre transform of the corresponding radial profile. However, for this to be an accurate approximation, one must on the one hand assume that the beams on the two sides are very similar, and on the other hand either assume that both beams are intrinsically circularly symmetric, or that all pixels on the sky are observed from all angles an equal number of times due to the scanning strategy. In reality none of these conditions are met, and one may therefore ask whether there might be any residual effect due to the combination of an asymmetric beam and anisotropic scanning in the WMAP beam functions.

This problem was addressed analytically by [28], who derived an approximate expression for the expected power spectrum bias due to asymmetric beams in the WMAP data. Their conclusion was that such effects were $\lesssim$1% for the 3-year WMAP data.

In this chapter, we revisit the question of asymmetric beams in WMAP with two main goals. First, we seek to estimate the effective beam transfer functions for each WMAP DA, taking into account the full details of the asymmetric beams and specifics of the WMAP scanning strategy by direct simulation. This way, we check

whether the analytic approximations presented by [28] are valid. Second, we want to produce a set of high-fidelity simulated CMB sky maps, with beam properties as close as possible to those observed by WMAP, that can later be used for general studies of asymmetric beam effects in WMAP.

It was pointed by the referee of this work, that we didn't take into account the fact that the beam maps distributed by the WMAP collaboration are smoothed. As a consequence of this, the method that we employ in this chapter is sound, but the quoted numbers will be modified. We intent to take this effect into account in a revised version of this work.

3.2 Pipeline overview

In this section we summarize the methods and algorithms used in this chapter. Note that none of the individual steps described below are original to this chapter, and only the main ideas will therefore be discussed in the following.

We begin by defining our notation. We will be estimating the product of the WMAP beam transfer function, b_ℓ, and pixel window, p_ℓ, by direct simulation. This product is denoted $\beta_\ell = b_\ell p_\ell$. Given this function, the combined effect on a sky map, $T(\hat{n})$, of convolution by an instrumental beam and averaging over finite-sized pixels may be approximated in harmonic space as

$$T(\hat{n}) = \sum_{\ell=0}^{\ell_{\rm max}} \sum_{m=-\ell}^{\ell} \beta_\ell a_{\ell m} Y_{\ell m}(\hat{n}), \tag{3.1}$$

where $Y_{\ell m}(\hat{n})$ are the usual spherical harmonics.

The angular power spectrum of T is given by

$$\hat{C}_\ell = \frac{1}{2\ell+1} \sum_{m=-\ell}^{\ell} \beta_\ell^2 |a_{\ell m}|^2, \tag{3.2}$$

while the power spectrum of the true underlying CMB map, $s(\hat{n})$, is

$$C_\ell = \frac{1}{2\ell+1} \sum_{m=-\ell}^{\ell} |a_{\ell m}|^2. \tag{3.3}$$

The effect of the beam convolution and pixel averaging on the power spectrum is therefore simply given by a multiplication with β_ℓ^2.

The overall approach for estimating β_ℓ used in this chapter may be summarized by the following steps: First, we simulate time-ordered data (TOD) for each DA, taking into account both the detailed beam maps of WMAP and the exact orientation of the spacecraft at each point in time. We then produce a sky map from this TOD. Finally we compute the square root of the ratio between the output and the input power spectra, which becomes our estimate of β_ℓ.

Note that in this chapter we are only concerned with the effect of asymmetric beams, not other systematic effects such as instrumental noise. All following discussions will therefore assume noiseless observations.

3.2.1 Simulation of time-ordered data

Our first step is to simulate a reference CMB sky realization, s, given an angular temperature power spectrum, $C_\ell^{\rm theory}$. This can be achieved with a standard code such as "anafast", which is available in the HEALPix[1] software package. Note

[1] http://healpix.jpl.nasa.gov

that this map should not be smoothed with either an instrumental beam or a pixel window; adding these effects is the task of the following pipeline. Explicitly, the input reference map should simply be pure spherical harmonic modes projected onto a set of pixel centers.

Next, we need to be able to convolve this map with a given beam map at arbitrary positions and orientations on the sphere. In this chapter we do this by brute-force integration in pixel space. For an alternative fast Fourier space based approach to the same problem, see [95].

We define $\hat{p}$ to be a unit vector pointing towards the beam center, and specify its position on the sphere using longitude and co-latitude (ϕ, θ). We further define ψ to be the angle between some fixed reference direction in the beam map and the local meridian. The value of the beam map at position $\hat{n} = (\phi', \theta')$, which in principle is non-zero over the full sky, is denoted $b(\phi', \theta'; \phi, \theta, \psi)$. With these definitions, the desired convolution may be written as

$$T(\phi, \theta, \psi) = \int_{4\pi} s(\phi', \theta') b(\phi', \theta'; \phi, \theta, \psi) d\Omega'. \tag{3.4}$$

Computationally speaking, we approximate this integral as a direct sum over HEALPix pixels, which all have equal area, with the product $s \cdot b$ being evaluated at HEALPix pixel centers. To make these calculations computationally feasible, we assume that the beam is zero beyond some distance from the beam center (ranging between 3.5 and 7° for the WMAP channels), and thus only include the main lobe in the following analysis. While the WMAP beam maps are provided as pixelized maps, we need to know the beam values at arbitrary positions (i.e., HEALPix pixel

centers). We solve this by computing a 2D spline for each beam map, enabling us to interpolate to arbitrary positions.

WMAP is a differential experiment, and measures at each point in time the difference between the signals received by two different detectors, denoted A and B. The full set of time-ordered WMAP data may therefore be written as

$$d_x(i) = T_x^{\mathrm{A}}(i) - T_x^{\mathrm{B}}(i), \tag{3.5}$$

where $x = \{\mathrm{K1, Ka1, Q1\text{-}2, V1\text{-}2, W1\text{-}4}\}$ is a DA label, and i is a time index, and for each detector a short-hand for (ϕ, θ, ψ). This equation may be written in the following matrix form,

$$\mathbf{d}_x = \mathbf{A}\mathbf{T}_x, \tag{3.6}$$

where we have introduced an $N_{\mathrm{tod}} \times N_{\mathrm{pix}}$ pointing matrix $\mathbf{A}$. This matrix contains two numbers per row; 1 in the column hit by the center of beam A at time i, and -1 in the column hit by the center of beam B.

The remaining problem is to determine the position and orientation of each detector at each time step. This information has been made publicly available by the WMAP team on LAMBDA[2], and consists of a large set of pointing files together with useful IDL routines for extracting the desired information.

3.2.2 Map making with differential data

For the map making step we adopt the algorithm developed by Wright et al. [96], which was used in the 1- and 3-year WMAP pipelines [85, 28]. Here we only sum-

[2] http://lambda.gsfc.nasa.gov

marize the essential algebra, and outline the algorithm.

Our goal is to establish an unbiased and, preferably, optimal estimate of the (smoothed) sky signal, $\hat{\mathbf{T}}$, given a set of differential TOD values, $\mathbf{d}$. For noiseless data, the maximum likelihood estimator is simply

$$\hat{\mathbf{T}} = (\mathbf{A}^t\mathbf{A})^{-1}\mathbf{A}^t\mathbf{d}. \tag{3.7}$$

For high-resolution sky maps, this equation involves an inverse of a large matrix and cannot be solved explicitly. Instead, one often resorts to iterative methods such as Conjugate Gradients, or, for differential data, the method developed by Wright et al. [96].

We present the iterative differential map maker in a simple manner: Define $\mathbf{D}$ to be the diagonal matrix that counts the number of hits $N_{\rm obs}(p)$ per pixel p on the diagonal, and a_i and b_i to be the pixels hit by side A and side B at time i, respectively. Suppose that we already have established some estimate for the solution, $\hat{\mathbf{T}}^j$. (Note that this can be zero.) Then the iterative scheme

$$\hat{\mathbf{T}}^{j+1} = \hat{\mathbf{T}}^j + \mathbf{D}^{-1}\mathbf{A}^t(\mathbf{d} - \mathbf{A}\hat{\mathbf{T}}^j) \tag{3.8}$$

will converge to the true solution: If $\hat{\mathbf{T}}^j = \mathbf{T}$, then $\mathbf{d} = \mathbf{A}\hat{\mathbf{T}}^j$, and the second term on the right hand side is zero. This algorithm is implemented by the following scheme:

$$\hat{T}_p^{j+1} = \frac{\sum_i \left(\delta_{p,a_i}\left[\hat{T}_{b_i}^j + d_i\right] + \delta_{p,b_i}\left[\hat{T}_{a_i}^j - d_i\right]\right)}{N_{\rm obs}(p)}. \tag{3.9}$$

This algorithm was originally presented by Wright et al. [96]. The only new

DA	FWHM (arcmin)	Radius (degrees)	$N_{\rm side}$	$\ell_{\rm max}$	$\ell_{\rm hybrid}$	$N_{\rm samples}$ (10^8)	$\sigma_{\rm N}$ (μK)
K1	53	7.0	512	750	318	2.5	...
Ka1	40	5.5	512	850	411	2.5	...
Q1	31	5.0	512	1100	522	3.1	78.2
Q2	31	5.0	512	1100	515	3.1	74.2
V1	21	4.0	1024	1500	789	4.1	99.0
V2	21	4.0	1024	1500	779	4.1	88.2
W1	13	3.5	1024	1700	1164	6.2	143.8
W2	13	3.5	1024	1700	1148	6.2	159.7
W3	13	3.5	1024	1700	1162	6.2	168.5
W4	13	3.5	1024	1700	1169	6.2	164.4

Table 3.1: Summary of DA parameters. Note: FWHM is the effective symmetrized beam size. The Radius is used for pixelized beam convolutions. See [84] for details. Average full-sky RMS values evaluated at $N_{\rm side} = 512$.

feature introduced here is the choice of starting point. In the original paper, Wright et al. [96] initialized the iterations at the DMR dipole, since their test simulation included a CMB dipole term. However, for a given scanning strategy, there will often be some large-scale modes that are less well-sampled than others. For instance, for the WMAP strategy $\ell = 5$ is more problematic than other modes [85]. This leads to slow convergence with the above scheme for this mode.

We therefore choose a different approach: Before solving for the high-resolution map by iterations, we solve Equation 3.7 by brute-force at low resolution. For the cases considered later in this chapter, we choose a HEALPix resolution of $N_{\rm side} = 16$ for this purpose. With 3072 pixels, about 30 seconds are needed to solve this system by singular value decomposition. (Note that the monopole is arbitrary for differential measurements, and one must therefore use an eigenvalue decomposition type algorithm to solve the system.) The improvement in convergence speed due to this choice of initial guess is explicitly demonstrated in Appendix A.

Our convergence criterion is chosen such that the RMS difference between two

consecutive iterations must be less than 0.05 μK. We have verified that this leads to errors of less than 0.1 μK in the final solution, of which most is due to a residual dipole. This is typically achieved with 30–50 iterations, although some converge already after 20–30 iterations and a few after 70 or more iterations.

At first glance, the fact that the final residuals are as small as 0.1 μK for an RMS stopping criterion as large as 0.05 μK may seem surprising. However, this is explained by the fact that the iterative solution obtained by Equation 3.8 often alternates between high and low values about the true answer. This suggests that a further improvement to the algorithm may be possible: Faster convergence may perhaps be obtained by computing the average of two consecutive iterations, $\hat{\mathbf{T}} = (\hat{\mathbf{T}}^j + \hat{\mathbf{T}}^{j+1})/2$, as the map estimate for iteration $j+2$. However, the computational resources spent during map making is by far sub-dominant compared to the TOD simulation, and we have therefore not yet implemented this step in our codes.

3.2.3 Estimation of hybrid beam transfer functions

As described in the introduction to this section, we estimate the transfer function by the square root of the ratio between the power spectra of the convolved map and the input map,

$$\hat{\beta}_\ell = \sqrt{\frac{\hat{C}_\ell}{C_\ell}}. \tag{3.10}$$

However, as noted above, this function describes both the effect from instrumental beam smoothing and averaging over pixels. In the present chapter we are concerned mostly with the former of these, which has a stronger impact on large to intermediate scales. This is because the beam component is largely independent of total observation time, assuming at least one year of observations for WMAP, whereas the

pixel averaging component depends strongly on total observation time, or the average number of samples per pixel. The latter, therefore, evolves much more strongly with time than the former, as will be explicitly demonstrated later.

In order to provide transfer functions that are valid for long observation periods (e.g., 5 or 7 years of WMAP observations), we choose to construct a hybrid transfer function,

$$\hat{\beta}_\ell = \begin{cases} \sqrt{\frac{\hat{C}_\ell}{C_\ell}} & \text{for} \quad \ell \leq \ell_{\rm hybrid} \\ \sqrt{\frac{\hat{C}_{\ell_{\rm hybrid}}}{C_{\ell_{\rm hybrid}}}} \frac{b_\ell^{\rm WMAP}}{b_{\ell_{\rm hybrid}}^{\rm WMAP}} \frac{p_\ell}{p_{\ell_{\rm hybrid}}} & \text{for} \quad \ell > \ell_{\rm hybrid} \end{cases} . \tag{3.11}$$

Here $b_\ell^{\rm WMAP}$ is the nominal symmetrized transfer function published by the WMAP team, p_ℓ is the (uniformly averaged) HEALPix pixel window, and $\ell_{\rm hybrid}$ is some transition multipole. In other words, we adopt our own direct estimate of the transfer function up to $\ell_{\rm hybrid}$, but the symmetrized, asymptotically uniform and properly scaled WMAP transfer function at higher multipoles.

Note that this issue is of minor importance in terms of cosmological interpretation, i.e., angular power spectrum and cosmological parameters, because the transition typically takes place in the noise dominated high-ℓ regime. The effect of the anisotropic pixel window is, therefore, largely suppressed. In the present chapter, we choose to focus on the beam dominated region, and leave a detailed study of the pixel window to a future paper. See Section 3.4 for a detailed discussion of this issue.

Finally, because we only generate a relatively small number of simulations in this chapter, there is considerable Monte Carlo scatter in our estimated transfer functions on an ℓ-by-ℓ basis. To reduce this Monte Carlo noise, we smooth all transfer functions using the smooth spline formalism described by Green & Silverman [81]

and others.

3.3 Data and simulations

All data products used in this study are provided by the WMAP team on LAMBDA as part of their 5-year data release. However, the calculations performed here are computationally extremely demanding, and we therefore include only roughly one year's worth of data in our calculations. To be precise, we include the period between July 10th 2001 and August 2nd 2002, except for three days with missing data, for a total of 383 days[3].

We consider all 10 WMAP DAs in our calculations, which are denoted, in order from low to high frequencies, K1 (23 GHz), Ka1 (33 GHz), Q1–2 (41 GHz), V1–2 (61 GHz) and W1–4 (94 GHz), respectively. Their resolutions range from 53' FWHM at K-band to 13' FWHM at W-band. Because of this large range in resolution, we specify the pixel resolution and harmonic space range for each case separately. For instance, K-band is pixelized at $N_{\rm side} = 512$, and includes multipoles up to $\ell_{\rm max} = 750$ (the highest multipole present in the transfer function provided by the WMAP team), while the W-band is pixelized at $N_{\rm side} = 1024$, and includes multipoles up to $\ell_{\rm max} = 1700$. A full summary of all relevant parameters for each DA is given in Table 3.1.

Note that the listed noise RMS values are only used for estimating the power spectrum weights in Section 3.6. For simplicity we have adopted the official RMS values for the foreground-reduced 5-year WMAP maps here, but note that there is

[3]Our original intention was to include precisely one year of observations in our analysis, and therefore we processed 365 WMAP pointing files. However, we noticed after the calculations were completed that some of the pointing files contained slightly more than one day's worth of data, such that a total of 383 days was in fact included.

a $\sim 1\%$ bias in some of these values [83]. However, this has no significant impact on the results presented in this chapter.

The beam maps for each DA are provided in the form of pixelized maps and separately for side A and B. Each beam map contains non-zero values inside a radius around the beam center which is specified for each DA. For instance, the K-band radius is 7°, and the W-band radius is 3.5°. When evaluating the convolution defined in Equation 3.4, we include all pixels inside this radius.

The pixel size of the beam maps is $2.4'$, which over-samples even the W-band beams. Based on these high-resolution maps, we precompute all coefficients of the corresponding bi-cubic spline which allows us to very quickly interpolate at arbitrary positions in the beam map with high accuracy.

Each beam is normalized by convolving a map constant equal to 1 at 1000 random positions and orientations, and demanding that the average of the resulting 1000 values equals unity. With the 2D spline interpolation scheme, the random uncertainties on the normalization due to beam position and orientation are $\sim$ 0.2%. For comparison, directly reading off pixel values from the beam maps without interpolation lead to variations in the normalization at the $\sim 2\%$ level.

For our base CMB reference sky set, we draw ten random Gaussian realizations from the best-fit ΛCDM power spectrum derived from the 5-year WMAP data alone [1]. These maps are generated at both $N_{\rm side} = 512$ and $N_{\rm side} = 1024$ using the same seeds, and include neither an instrumental beam nor a pixel window; they are simply spherical harmonic modes projected onto the HEALPix pixel centers. All ten realizations are processed for all ten DAs, such that the resulting simulations may be used for multifrequency analysis, if so desired.

As noted above, the computational requirements for the analyses presented here are demanding. The CPU time for processing a single W-band DA is $\sim$ 4000 hours, and the total disk usage for the entire project is $\sim$1TB. For comparison, the corresponding map making step requires $\sim$ 60 CPU hours, and is thus completely sub-dominant the TOD simulation.

3.4 Comparison with analytic case

In order to test our pipeline and understand its outputs, we start by considering a perfect Gaussian beam. This case is treated in two different ways: First, we convolve a CMB realization directly in harmonic space (as defined by Equation 3.1) with a $\sigma_{\rm fwhm} = 20'$ FWHM analytic Gaussian beam and the appropriate HEALPix pixel window, p_ℓ for $N_{\rm side} = 1024$. The combined transfer function for this case reads

$$\beta_\ell^{\rm ref} = e^{-\frac{1}{2}\ell(\ell+1)\sigma^2} p_\ell, \tag{3.12}$$

where $\sigma = \sigma_{\rm fwhm}/\sqrt{8\ln 2}$, and $\sigma_{\rm fwhm}$ is expressed in radians.

Second, we map out a corresponding two-dimensional Gaussian in pixel space over a grid of $2.4'$ pixels, the same resolution as the WMAP beam maps. We then input this into our simulation pipeline together with the same CMB realization used for the analytic convolution, and with the V1 channel pointing sequence. From the resulting brute-force convolved map, we then obtain the effective transfer function, β_ℓ, as described in Section 3.2.3.

This function is plotted in the top panel of Figure 3.1, together with the product of the analytic Gaussian beam and the HEALPix pixel window. The ratio of the

two effective functions is shown in the lower panel.

From this figure it is clear that the agreement between the two approaches is excellent up to $\ell \approx 800$. At higher ℓ's, however, the ratio increases rapidly, indicating that the analytic approach smooths more than the brute-force approach. This is due to the different definitions of the pixel windows in the two cases: In the HEALPix case, the pixel window is defined as an effective average both over each pixel and over the full sky. In other words, it assumes that all points have been observed an equal (and infinite) number of times.

However, this is not the case for a real experiment which scans the sky for a finite length of time. As a consequence, each pixel is observed only a relatively small number of times, and this leads effectively to less smoothing. In the extreme case of only one observation per pixel, there would be no pixel averaging at all. Now, the average pixel window would formally equal unity. On the other hand, the random realization-specific uncertainties would be very large, and the pixel window as such would have zero predictive power.

In practice, one is well advised not to consider scales smaller than those that are properly oversampled by the scanning strategy. In this chapter, we adopt the analytic case considered in this section to guide us in determining which scale that is. Explicitly, we conservatively demand that the effective beam transfer function must be greater than 0.15 in order to consider it to be properly oversampled, and therefore independent of scanning strategy. We adopt the corresponding multipole moment to be $\ell_{\rm hybrid}$, as defined in Section 3.2.3. Thus, the symmetrized WMAP beam and HEALPix pixel window are used at scales for which the beam amplitude drops below 0.15.

Note that if we included more years of WMAP scanning in our calculations, we could increase $\ell_{\rm hybrid}$, since we would obtain more samples, and the WMAP pointings do not perfectly coincide from year to year. This is computationally very expensive, and we have therefore chosen to limit our analysis to the range described here.

As a direct illustration of this effect, we present in Figure 3.2 the transfer function ratios for the V1 WMAP DA with respect to the nominal WMAP transfer function, computed for both six months of observations and a full year of observations. The low and intermediate ℓ behaviour is the same for the two, but the pixel window effect becomes important earlier for the six month case than for the full year case.

3.5 The effect of asymmetric beams in WMAP

We now present the main results obtained in this chapter, namely the effective beam transfer functions for each WMAP DA, taking into account both the full asymmetric beam patterns and scanning strategy. These are shown in Figure 3.3 (red lines), and compared to the nominal WMAP transfer functions (dashed black lines). The vertical dotted line indicates $\ell_{\rm hybrid}$ for each case.

Clearly, the differences between the two sets of results are relatively small, as no visual discrepancies are seen in this plot. However, in Figure 3.4 we plot the ratio between our transfer functions and the WMAP transfer functions for $\ell \leq \ell_{\rm hybrid}$, and here we do see small but significant differences between the two sets of results.

First, we see that the ratios are essentially unity on the largest scales (smallest ℓ's), before they start diverging either towards high or low values at some characteristic scale. There are two exceptions to this trend, namely W1 and W4, which

start diverging essentially already at very low ℓ's.

Next, the transfer functions split into two main groups: our K1, Ka1 and Q1–2 transfer functions are slightly higher than the corresponding WMAP functions, while the V and W DAs are slightly lower.

Both of these general and qualitative remarks reflect the position of each DA in the WMAP focal plane (see Figure 6 of Jarosik et al. 2007 for an excellent visualization of the A side beams): K1, Ka1 and Q1–2 are positioned the furthest away from the optical axis, while V1–2 and W1–4 are the closest. Similarly, W1 and W4 are positioned lower in elevation, and generally have more sub-structure than W2 and W3.

However, it should be emphasized that the overall differences are generally small, typically less than 2% at $\ell \leq \ell_{\rm hybrid}$. Further, these differences are only significant (again, with the exception of W1 and W4) in the intermediate- and high-ℓ ranges.

To build up some intuitive understanding of the spatial variations caused by the asymmetric WMAP beams, we show in Figure 3.5 the difference between the fully asymmetrically convolved map and the corresponding map convolved with the symmetrized transfer function directly in harmonic space for one of the V1 simulations. Thus, the two convolved maps have identical power spectra, but slightly different phases. The top panel shows the full-sky difference map with a temperature scale of $\pm 5 \mu$K. The lower panels show two selected $15^\circ \times 15^\circ$ regions centered on the north ecliptic pole (NEP; top row) and the Galactic center (GC; bottom row), respectively. The left column shows the actual temperature map convolved with the asymmetric beam, and the right column shows the same differences as in the full-sky plot.

The first striking feature seen in this map is that the differences are clearly larger in the ecliptic plane than around the ecliptic poles. This is due to the WMAP scanning strategy, which leads to a larger number of observations per pixels around the poles, and also with a greater range of beam orientations. Next, it is difficult to spot any single unambiguous and well-defined correlation between the convolved and the difference maps. Clearly, there are similar morphological structures in the two, but the sign of the correlations appears to vary. Third, we see a clear tendency of diagonal striping in the GC plot, which corresponds to correlations along ecliptic meridians and lines of constant latitude. (Note that these plots are shown in Galactic coordinates, while the WMAP scanning strategy is nearly azimuthally symmetric in ecliptic coordinates.)

In the next section, we consider the impact of the asymmetric beams on cosmological parameters. However, before concluding this section we make a comment concerning an outstanding issue regarding the 3-year WMAP power spectra first noted by [79]. They pointed out the presence of a 3σ amplitude discrepancy between the V- and W-band power spectra (Figure 5 of Eriksen et al., 2007). Specifically, the V-band spectrum was biased low compared to the W-band spectrum between $\ell = 300$ and 600 by $\sim 80\mu\mathrm{K}^2$. [88] later showed that $\sim 30\mu\mathrm{K}^2$ of this discrepancy could be attributed to over-estimation of point source power in the 3-year WMAP spectrum analysis, and this was subsequently confirmed and corrected by [28]. Still, about $50\mu\mathrm{K}^2$ of this difference remained, which was statistically significant at $\sim 2\sigma$.

[79] proposed that this difference might be due to errors in the beam transfer functions caused by asymmetric beams. Given the new results presented in this chapter, we are now in a position to consider this issue more quantitatively. The

relevant question is then whether the WMAP V-band transfer functions are systematically biased high compared to the W-band functions. At first glance, one may get this impression from the plots shown in Figure 3.4: The V-band ratios both drop noticeably from $\ell = 300$ (decreasing nearly linearly from -0.2 to -0.7%), whereas W2 and W3 are slightly high in the same range, at about +0.1 to +0.2%. On the other hand, W1 and W4 are even lower than the V-band functions, at -0.4 to -0.6%. The net difference is therefore not more than a few tenths of a percent, which corresponds to $\sim 10\mu\mathrm{K}^2$ in the power spectrum. Thus, it is possible that this effect may contribute somewhat to the power spectrum discrepancy between V- and W-band, but it does not seem to fully explain the difference.

3.6 Impact on cosmological parameters

We now assess the impact of asymmetric beams in WMAP on cosmological parameters. We do this by modifying the co-added 5-year WMAP temperature power spectrum [91] provided with the WMAP likelihood code [78, 1] according to the transfer function ratios shown in Figure 3.4, and run CosmoMC [90] to estimate the resulting parameters. Only a simple 6-parameter ΛCDM model is considered in this chapter. For comparison, we also run the code with the nominal WMAP spectrum as input, so that we can directly estimate the impact of asymmetric beams with everything else held fixed.

Unfortunately, the individual cross-spectra for each pair of DAs have not yet been published by the WMAP team, but only the total co-added spectrum. We must, therefore, make a few approximations in order to apply the proper beam corrections to the full spectrum. First, let σ_n^i denote the white noise level of DA

i (see Table 3.1), β_ℓ^i the transfer function estimate derived in this chapter, and let $\beta_\ell^{i,\mathrm{WMAP}}$ be the nominal WMAP transfer function. Finally, define

$$\delta_\ell^i = \frac{\beta_\ell^i}{\beta_\ell^{i,\mathrm{WMAP}}} - 1 \tag{3.13}$$

to be the fractional difference between the two.

Next, the WMAP team uses the MASTER pseudo-spectrum algorithm [87] for power spectrum estimation [85, 28, 91], which quickly produces good estimates at high ℓ's. However, this method is not a maximum-likelihood estimator, and it does not yield optimal error bars. To improve on this, the WMAP applies different pixel weights in different multipole regions: At low ℓ's, where the sky maps are signal dominated, they apply equal weights to all pixels, while at high ℓ's, where the maps are noise dominated, they apply inverse noise variance pixels weights. These weights are then taken into account when co-adding the cross-spectra obtained from all possible DA pairs (but excluding auto-correlations). The transition is made at $\ell = 500$.

Parameter	Nominal WMAP	Corrected beams	Shift in σ
$\Omega_\mathrm{b}h^2$	0.0228 ± 0.0006	0.0228 ± 0.0006	0.1
$\Omega_\mathrm{cdm}h^2$	0.109 ± 0.0006	0.112 ± 0.006	0.4
$\log(10^{10}A_\mathrm{s})$	3.064 ± 0.042	3.079 ± 0.042	0.4
τ	0.089 ± 0.017	0.089 ± 0.017	0.00
h	0.722 ± 0.027	0.716 ± 0.026	-0.3
n_s	0.965 ± 0.014	0.969 ± 0.014	0.3

Table 3.2: Comparison of cosmological parameters derived from the nominal WMAP power spectrum (second column) and from the power spectrum corrected for asymmetric beams (third column). The rightmost column shows the relative shift between the two in units of σ.

The beam-convolved (but noiseless) power spectrum $\tilde{C}_\ell^{ij}$ observed by a given DA pair, i and j, may be written as $\tilde{C}_\ell^{ij} = \beta_\ell^i \beta_\ell^j C_\ell$, where C_ℓ is the true power spectrum

of our sky, and β_ℓ^i is the true transfer function for DA i. The noise amplitude of the same spectrum is proportional to $\sigma_n^i \sigma_n^j / \beta_\ell^i \beta_\ell^j$. The inverse noise variance weight of this cross-spectrum is therefore approximately

$$w_{ij} = \frac{\frac{\beta_\ell^i \beta_\ell^j}{\sigma_n^i \sigma_n^j}}{\sum_{i'<j'} \frac{\beta_\ell^{i'} \beta_\ell^{j'}}{\sigma_n^{i'} \sigma_n^{j'}}}, \tag{3.14}$$

where the sum runs over all N different pairs of cross-spectra. (Note that this is only an approximation to the exact expression, because other effects also enter the full calculations. One important example is the sky cut, which couples different ℓ modes, and is taken into account through a coupling matrix. Such effects are not included in the analysis presented here.

Pulling all of this together, the appropriately co-added power spectrum provided by WMAP should ideally read

$$\hat{C}_\ell = \begin{cases} \frac{1}{N} \sum_{i<j} \frac{\tilde{C}_\ell^{ij}}{\beta_\ell^i \beta_\ell^j} & \text{for} \quad \ell \leq 500 \\ \sum_{i<j} w_{ij} \frac{\tilde{C}_\ell^{ij}}{\beta_\ell^i \beta_\ell^j} & \text{for} \quad \ell > 500, \end{cases} . \tag{3.15}$$

However, the spectrum that in fact is provided by WMAP is Equation 3.15 evaluated for $\beta_\ell = \beta_\ell^{\rm WMAP}$, which, according to our calculations, is slightly biased. To obtain the appropriate correction factor, $\alpha_\ell = \hat{C}_\ell / \hat{C}_\ell^{\rm WMAP}$, for each ℓ, we therefore set $\beta_\ell = \beta_\ell^{\rm WMAP}(1 + \delta_\ell)$ in Equation 3.15, and expand to first order in δ_ℓ. Doing this, we find that

$$\alpha_\ell = \begin{cases} 1 - \frac{1}{N} \sum_{i<j} (\delta_\ell^i + \delta_\ell^j) & \text{for} \quad \ell \leq 500 \\ 1 - \sum_{i<j} w_{ij}^{\rm WMAP} (\delta_\ell^i + \delta_\ell^j) & \text{for} \quad \ell > 500 \end{cases} \tag{3.16}$$

where $w_{ij}^{\rm WMAP}$ is the expression given in Equation 3.14 evaluated with $\beta_\ell^{\rm WMAP}$.

This function is plotted in Figure 3.6. Note, however, that we have capped the function by hand at $\ell = 750$ to be conservative, considering that our V-band transfer functions do not have support all the way to the maximum multipole used in the WMAP likelihood code, $\ell_{\rm max} = 1000$.

The results from the corresponding CosmoMC analyses are tabulated in Table 3.2 in terms of marginal means and standard deviations, and plots of the marginal distributions are shown in Figure 3.7. Here we see that there are small but noticeable shift in several parameters. For example, there is a positive shift of 0.4σ in the amplitude of scalar perturbations, $A_{\rm s}$, and 0.3σ in the spectral index of scalar perturbations. Although relatively modest, these shifts are certainly large enough that they should be taken properly into account.

3.7 Conclusions

This chapter has two main goals. First, we wanted to generate a set of WMAP-like simulations that fully take into account the asymmetric beams and anisotropic scanning pattern of the WMAP satellite. Such simulations are extremely valuable for understanding the impact of beam asymmetries on various statistical estimators and models. One example of such, which indeed provided us with the initial motivation for studying this issue, is the anisotropic universe model presented by [76], and later considered in detail with respect to the WMAP data by [82]. The result from that analysis was a tentative detection of violation of rotational invariance in the early universe, or some other effect with similar observational signatures, at the 3.8σ confidence level. It was shown that neither foregrounds nor correlated

noise could have generated this signal, but the question of asymmetric beams was left unanswered. This issue will now be revisited in an upcoming paper, using the simulations generated here.

The second goal of the chapter was to assess the impact of beam asymmetries on the WMAP power spectrum and cosmological parameters. We did this by comparing the power spectrum of the full beam convolved simulations with the power spectrum of the input realizations, thereby providing a direct estimate the effective beam transfer functions. Doing so, we found differences at the $1-2\%$ level in all differencing assemblies at intermediate and high ℓ's with respect to the nominal WMAP transfer functions.

A similar analysis was performed for the 3-year WMAP data release by [28], who approached the problem from an analytical point of view. However, at that time only the A-side beams were available [84], and they therefore assumed identical beams on both the A and B sides. With this data, they concluded that the impact of beam asymmetries was $\lesssim 1\%$ everywhere below $\ell = 1000$ for the V- and W-band DAs. For comparison, we find that there is a $\sim 1\%$ bias already at $\ell = 600$ for the combined co-added temperature power spectrum, and increasing rapidly to $\sim 1.5\%$ at $\ell = 750$. It is not unlikely that this trend may continue further in ℓ, but to answer that question would require considerably more computational resources. Nevertheless, the two analyses appear to be in reasonable agreement with each other, especially considering the fact that we take into account the full beam maps of both the A and B sides.

As far as cosmological parameters go, the impact of asymmetric beams appear to be small but noticeable. Specifically, we find shifts of 0.4σ in the amplitude of scalar

perturbations, $A_{\rm s}$, and the physical density of cold dark matter, $\Omega_{\rm cdm}h^2$, and 0.3σ in the spectral index of scalar perturbations, $n_{\rm s}$. While these shifts are relatively modest, they are of the same order of magnitude or larger than, say, marginalization over the Sunyaev-Zeldovich effect [94] or unresolved point sources [91], which indeed are taken into account.

One outstanding question that still remains is the impact of the anisotropic effective pixel window. As explicitly demonstrated in this chapter, the difference between the isotropized HEALPix pixel window and the actual WMAP V1 scanning induced pixel window becomes visible at $\ell \sim 900$ for one year of WMAP observations. Of course, this is well within the noise-dominated regime for the WMAP data, and unlikely to have any major impact on cosmological results, but we believe that a proper understanding of this issue, both with respect to WMAP and Planck, is warranted, and we intend to revisit this issue in a separate study.

The simulations described in this chapter may be downloaded from IKW's homepage[4].

[4]http://www.fys.uio.no/∼ingunnkw/WMAP5_beams

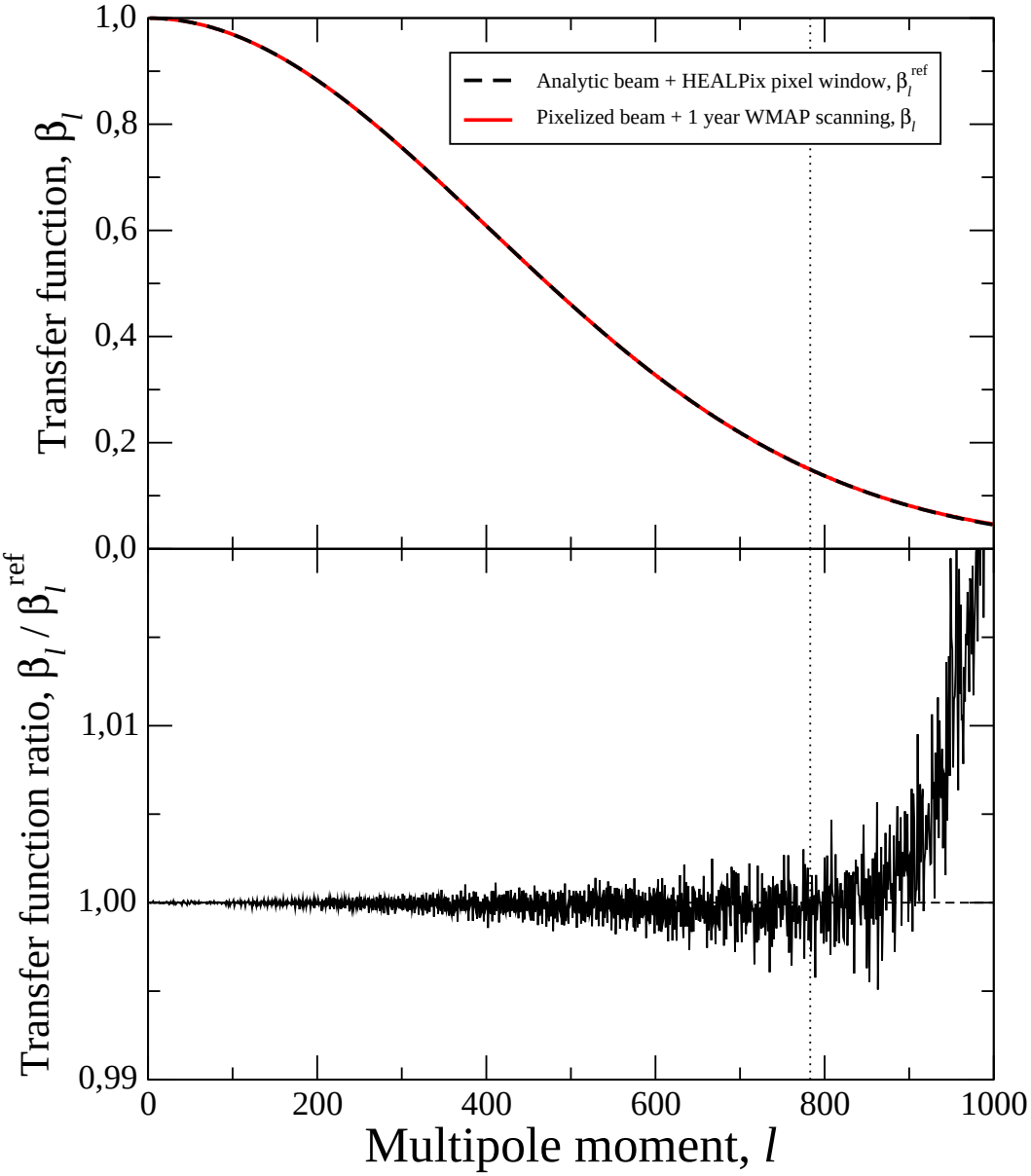

Figure 3.1: Top panel: Comparison between the transfer functions, β_ℓ, for a Gaussian beam of $20'$ FWHM. This was computed from a pixelized beam map and with the WMAP V1 scanning strategy (red line), and alternatively, by using the well-known analytic expression for the Legendre transform of a Gaussian beam (Equation 3.12) and isotropized HEALPix pixel window (black dashed line). The vertical dotted line indicates the multipole moment, $\ell_{\rm hybrid}$, at which $\beta_\ell = 0.15$. Bottom panel: The ratio between the transfer functions in the top panel. Note the excellent agreement up to $\ell \approx 800$, after which the differences in pixel window approximations becomes visible.

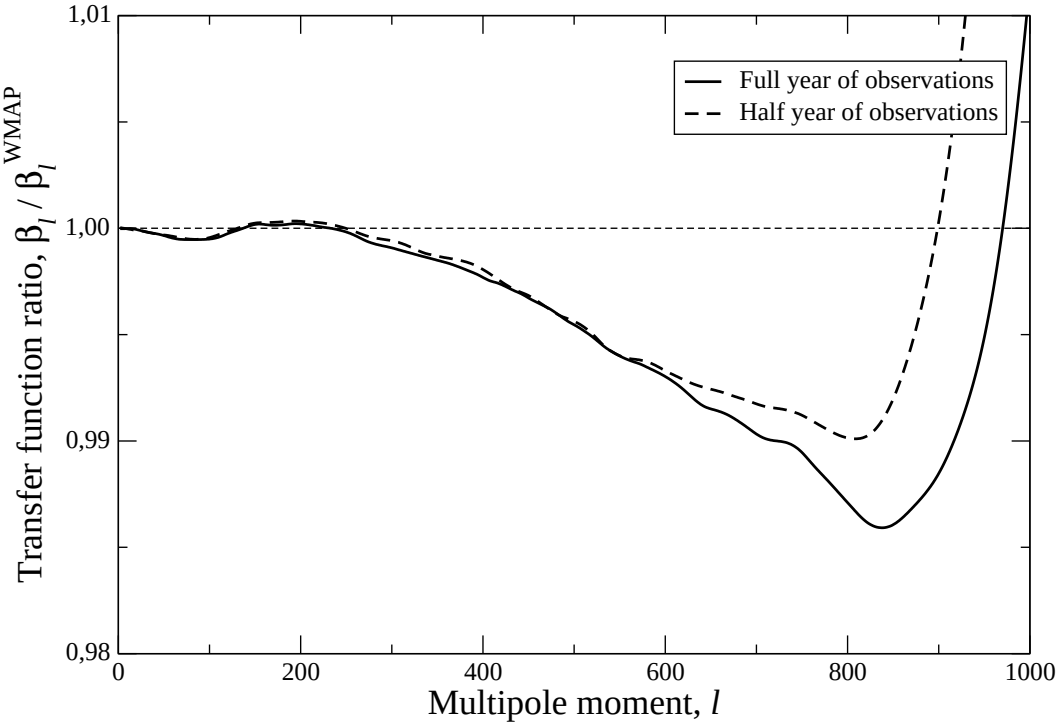

Figure 3.2: Comparison of the V1 WMAP beam transfer functions obtained from six (dashed line) and twelve (solid line) months of observations. Note that the behaviour at low and intermediate ℓ's is similar, whereas the pixel window-induced increase is seen earlier in ℓ for the six month data set than for the twelve month data set.

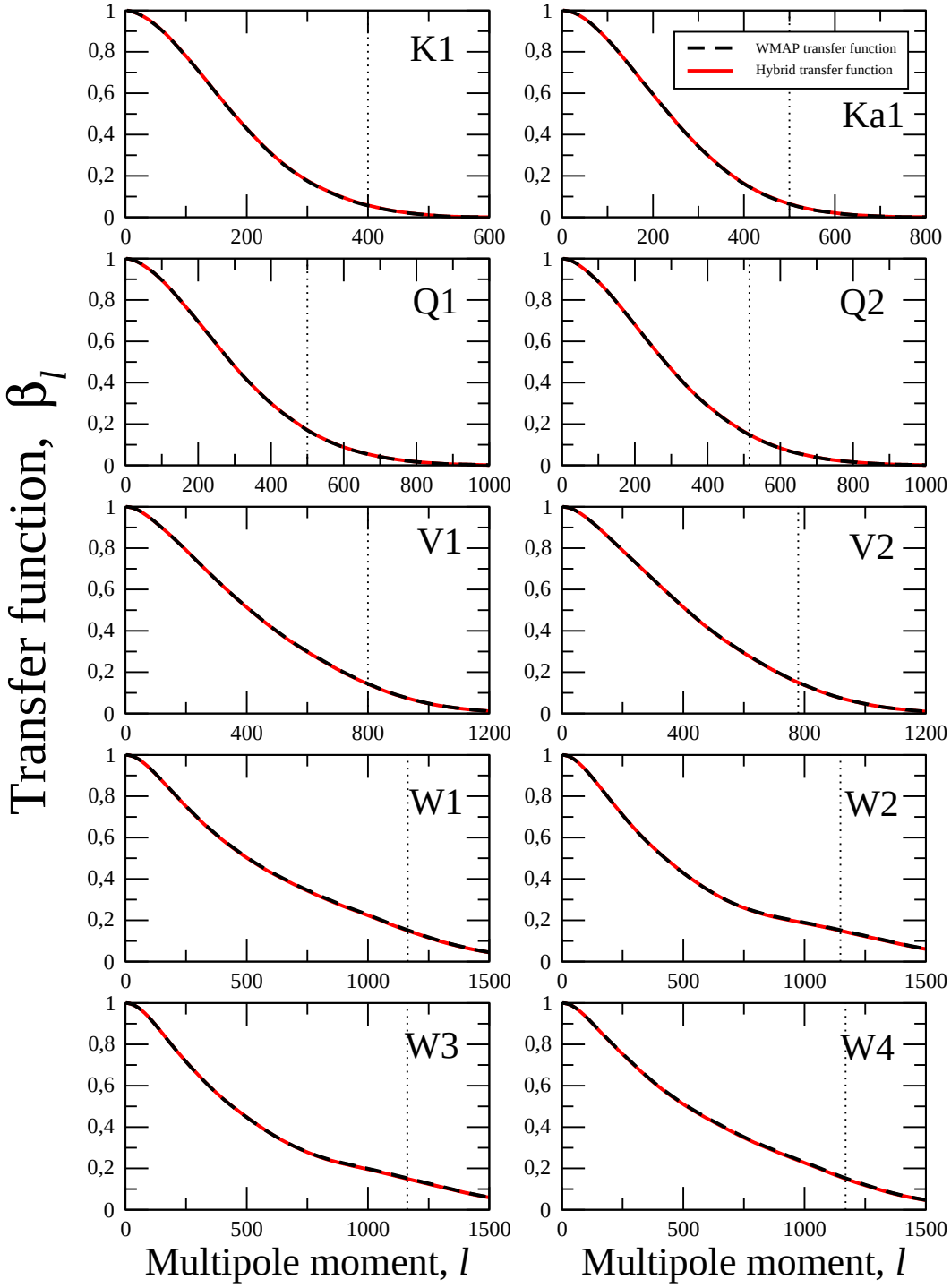

Figure 3.3: Comparison between transfer functions derived in this chapter (red lines) to the nominal WMAP transfer functions (black dashed lines). The transition multipole, $\ell_{\rm hybrid}$ is marked by dotted vertical lines.

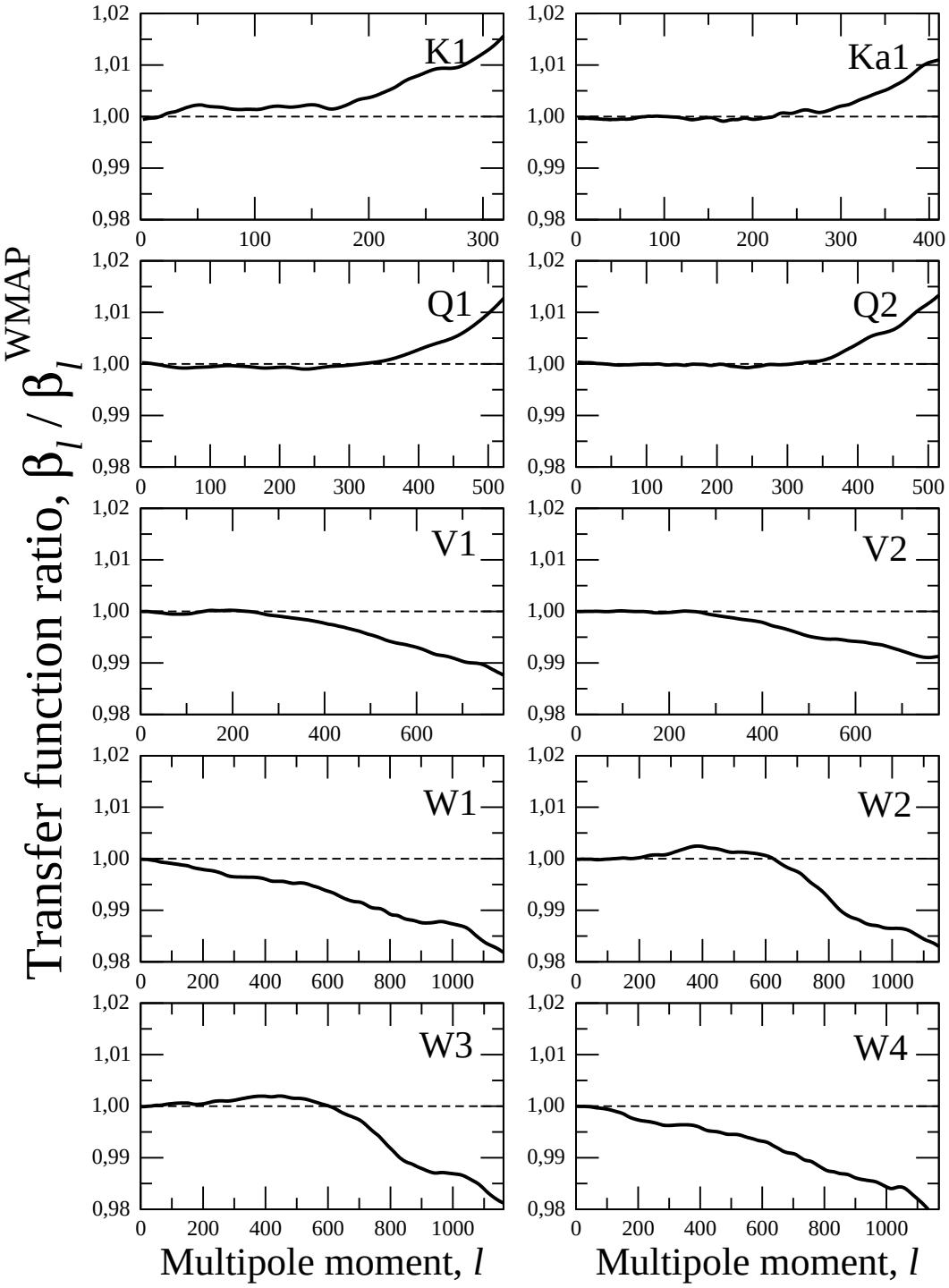

Figure 3.4: The ratio between the transfer functions derived in this chapter and the nominal WMAP transfer functions for all DAs. Note that the DAs split into two main groups depending on focal plane position: The outer DAs, K1, Ka1 and Q1–2, all rise with ℓ, whereas the inner DAs, V1–2 and W1–4, decrease with ℓ. Note also the similarity between W1 and W4, between W2 and W3, and between V1 and V2.

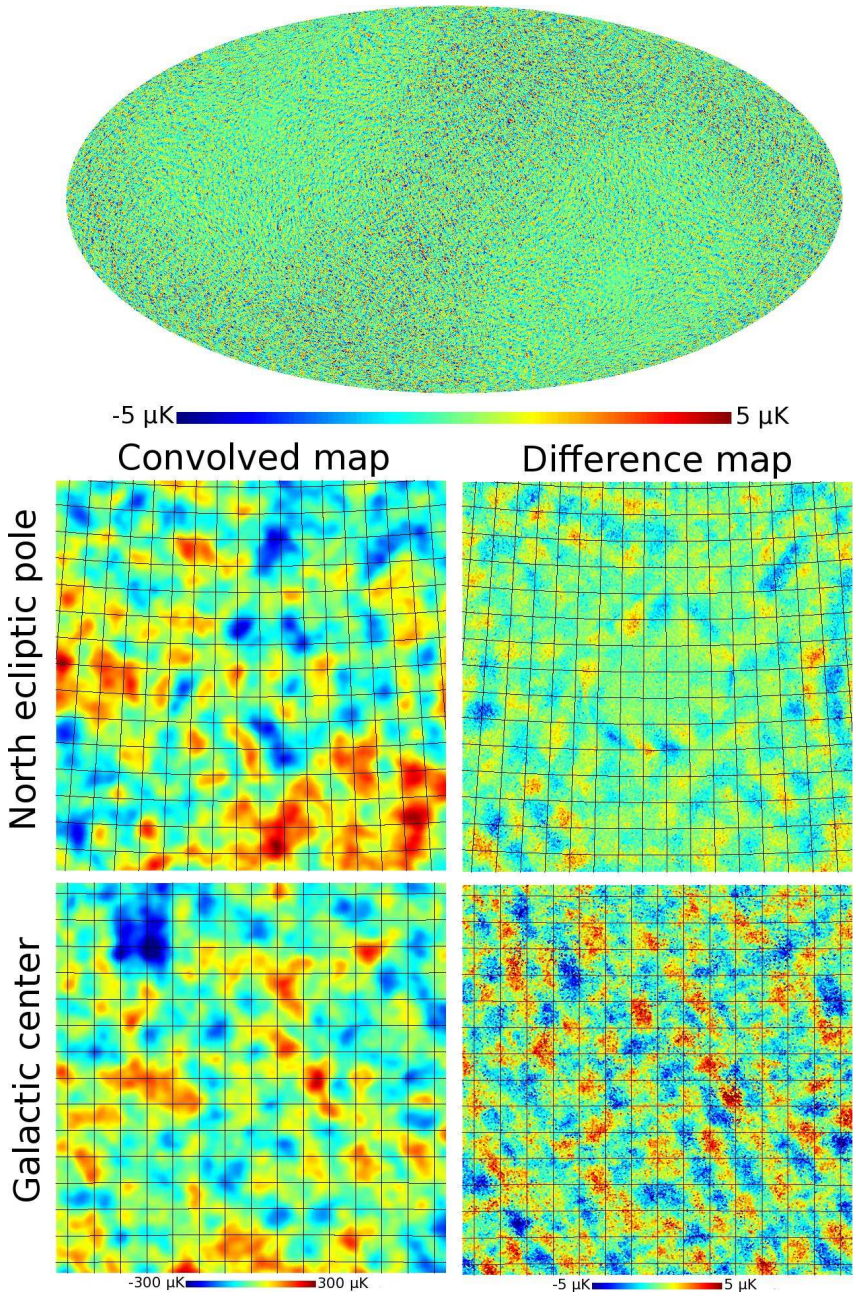

Figure 3.5: Top panel: Difference between a V1 simulation convolved with the full asymmetric beam and the same realization convolved with the corresponding symmetrized transfer function. The two maps have identical power spectrum but different phases. Note that larger differences are observed along the ecliptic plane, where the density of observations is lower than towards the ecliptic poles, and the cross-linking is also weaker. Bottom panels: Zoom-in on two regions, the north ecliptic pole (NEP; top row) and the Galactic center (GC; bottom row). Left column shows the map convolved with an asymmetric beam, and right column shows the same difference as in the top panel.

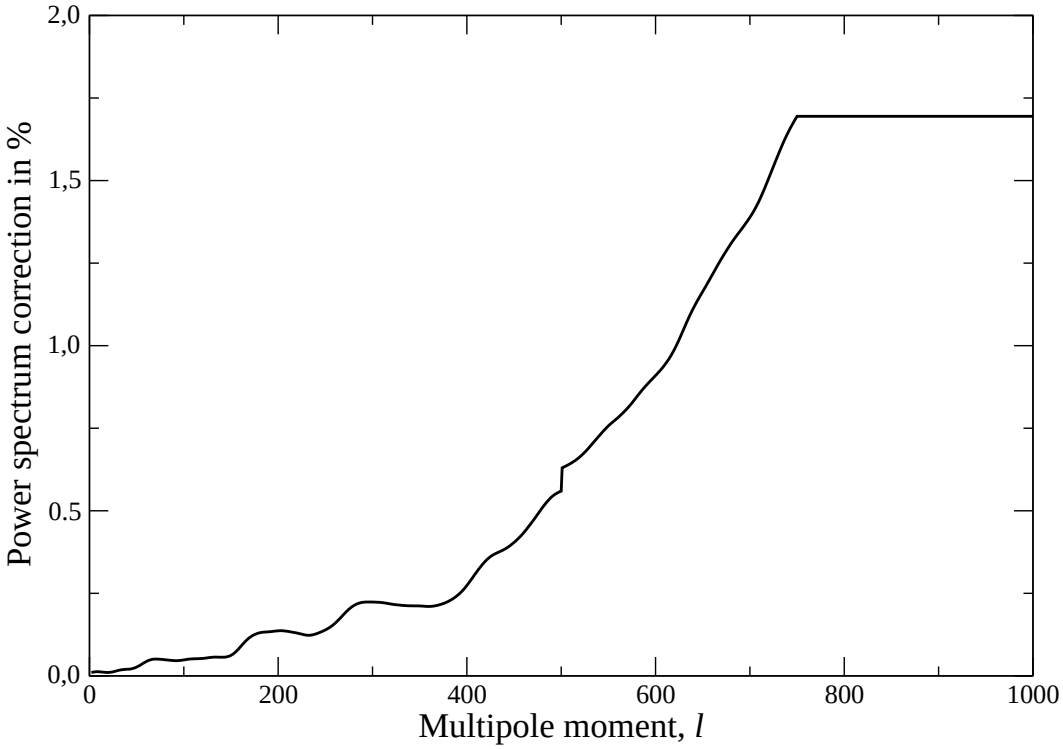

Figure 3.6: Total correction to the 5-year co-added WMAP temperature power spectrum due to asymmetric beams. Note the transition between high and low signal-to-noise weighting schemes at $\ell = 500$, and also the manually capped amplitude at $\ell > 750$. The latter is imposed in order to be conservative in the very high-ℓ regime, where the transfer functions are sensitive to pixel window effects.

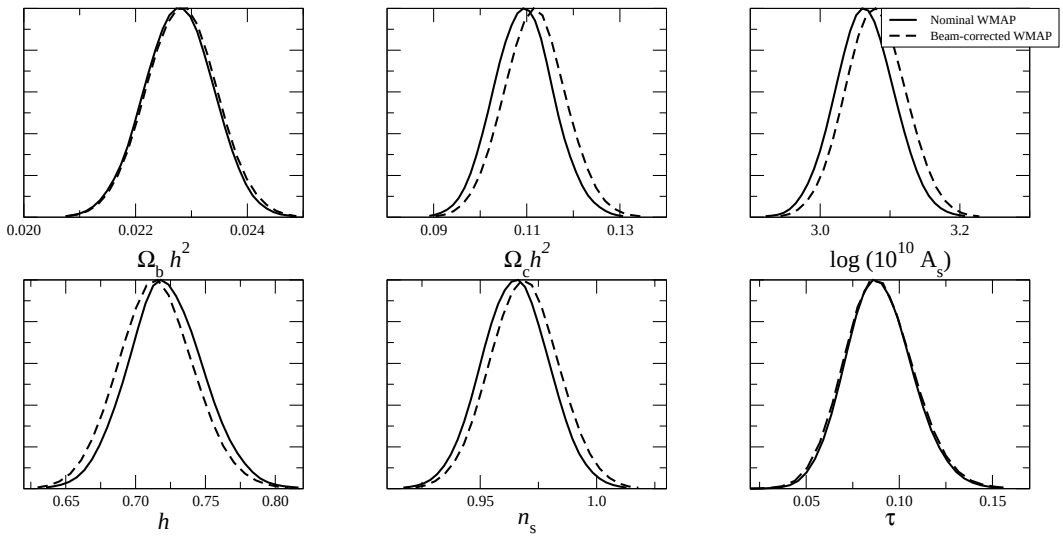

Figure 3.7: Marginal distributions for cosmological parameters derived with (dashed lines) and without (solid lines) correction for asymmetric beams.

Chapter 4

Dark Matter and Dark Radiation

4.1 Introduction

A wide variety of cosmological observations seem to point to a two-component dark sector, in which approximately 73% of the energy density of the universe is in dark energy and 23% is in non-baryonic dark matter (DM). Ordinary matter constitutes the remaining 4% [4, 12]. The physics of the dark matter sector is plausibly quite minimal: an excellent fit to the data is obtained by assuming that dark matter is a cold, collisionless relic, with only the relic abundance as a free parameter. The well-known "WIMP miracle" [12, 97, 98] is the fact that a stable, neutral particle with weak-scale mass and coupling naturally provides a reasonable energy density in DM. Particles of this type arise in models of low-scale supersymmetry [12] or large extra dimensions [13], and provide compelling DM candidates. In the contemporary universe, they would be collisionless as far as any conceivable dynamical effects are concerned.

Nevertheless, it is also possible to imagine a rich phenomenology within the dark sector. The dark matter could be coupled to a relatively strong short-range

force that could have interesting consequences for structure on small scales [14, 99]. Alternatively, DM could also be weakly coupled to long-range forces, which might be related to dark energy [100]. One difficulty with the latter is that such forces are typically mediated by scalar fields, and it is very hard to construct natural models in which the scalar field remains massless (to provide a long-range force) while interacting with the DM at an interesting strength.

In this paper, we explore the possibility of a long-range *gauge* force coupled to DM, in the form of a new unbroken abelian field, dubbed the $U(1)_D$ "dark photon." We imagine that this new gauge boson $\hat{\gamma}$ couples to a DM fermion χ, but not directly to any Standard Model (SM) fields. Our model is effectively parameterized by only two numbers: m_χ, the mass of the DM, and $\hat{\alpha}$, the dark fine-structure constant. If m_χ is sufficiently large and $\hat{\alpha}$ is sufficiently small, annihilations of DM particles through the new force freeze out in the early universe and are negligible today, despite there being equal numbers of positively- and negatively-charged particles. The dark matter in our model is therefore a plasma, which could conceivably lead to interesting collective effects in the DM dynamics.

Remarkably, the allowed values of m_χ and $\hat{\alpha}$ seem quite reasonable. We find that the most relevant constraint comes from demanding that accumulated soft scatterings do not appreciably perturb the motion of DM particles in a galaxy over the lifetime of the universe, which can be satisfied by $\hat{\alpha} \sim 10^{-3}$ and $m_\chi \sim$ TeV. For values near these bounds, the alterations in DM halo shapes may in fact lead to closer agreement with observation [14]. However, for such regions of parameter space, if $U(1)_D$ were the only interaction felt by the χ particles, the resulting relic abundances would be slightly too large, so we need to invoke an additional annihilation channel.

We show that χ can in fact be a WIMP, possessing $SU(2)_L$ quantum numbers in addition to $U(1)_D$ charge. Such a model provides the correct relic abundance, and is consistent with particle-physics constraints so long as the mixing between ordinary photons and dark photons is sufficiently small.

We consider a number of other possible observational limits on dark electromagnetism, and show that they do not appreciably constrain the parameter space. Since the DM halo is overall neutral under $U(1)_D$, there is no net long-range force that violates the equivalence principle. Although there are new light degrees of freedom, their temperature is naturally lower than that of the SM plasma, thereby avoiding constraints from Big-Bang Nucleosynthesis (BBN). Energy loss through dark bremsstrahlung radiation is less important than the soft-scattering effects already mentioned. The coupling of DM to the dark radiation background can, in principle, suppress the growth of structure on small scales, but we show that the DM decouples from the dark radiation at an extremely high redshift. On the other hand, we find that there are plasma instabilities (*e.g.*, the Weibel instability) that can potentially play an important role in the assembly of galactic halos; however, a detailed analysis of these effects is beyond the scope of this work.

The idea of an unbroken $U(1)$ coupled to dark matter is not new.[1] De Rujula et al. [102] explored the possibility that dark matter was charged under conventional electromagnetism (see also [105, 103, 104, 106]). Gubser and Peebles [107] considered structure formation in the presence of both scalar and gauge long-range forces, but concentrated on a region of parameter space in which the gauge fields were subdominant. Refs. [108, 109] considered several models for a hidden dark sector,

[1] Broken $U(1)$ forces have, of course, also been considered, see *e.g.* Ref. [101]

including one manifestation in which the dark matter consists of heavy hidden-sector staus interacting via a copy of electromagnetism. The effect of dimension-6 operators containing a new $U(1)$ gauge boson and SM fields was considered in Ref. [110], for models where the only fields in a hidden sector are charged under the new force. Additional models which contain unbroken abelian gauge groups may be found, for example in Refs. [111, 112]. In this paper, we construct minimal models of dark matter coupled to a new unbroken $U(1)_D$, leaving the dark fine-structure constant and dark-matter mass as free parameters, and explore what regions of parameter space are consistent with astrophysical observations and what new phenomena might arise via the long-range gauge interaction.

In Section 4.2, we introduce our notation for a minimal dark-matter sector including a new abelian symmetry $U(1)_D$. We then consider the bounds on the new dark parameters from successful thermal production of sufficient quantities of dark matter as well as requiring that BBN and cosmic microwave background (CMB) predictions remain unchanged. The restrictions of parameter space are closely related to those resulting from standard short-range WIMP dark matter. In Section 4.3, we consider the effect of long range interactions on DM particle interactions in the halos of galaxies. By requiring that our model not deviate too greatly from the predictions of collisionless DM, we find that the allowed regions of $\hat{\alpha}/m_\chi$ parameter space from Section 4.2 are essentially excluded. In order to evade these constraints, Section 4.4 describes an extended model, where the dark-matter candidate is charged under both $SU(2)_L$ and the new $U(1)_D$. Additional effects of dark radiation are presented in Section 4.5, and we conclude in Section 4.6.

We note that our model does not address the hierarchy problem, nor provide a

high-energy completion to the SM. However, new gauge groups and hidden sectors may be generic results of many such high-energy theories (*e.g.*, string and grand unified theories), and a WIMP coupled to an unbroken $U(1)$ is certainly a plausible low-energy manifestation of such theories. The most important lesson of our model is that interesting physics might be lurking in the dark sector, and it is worthwhile to consider a variety of possible models and explore their consequences for astrophysics and particle physics.

4.2 Dark Radiation and the Early Universe

We postulate a new "dark" abelian gauge group $U(1)_D$ with gauge coupling constant $\hat{g}$ and dark fine-structure constant $\hat{\alpha} \equiv \hat{g}^2/4\pi$. In the simplest case, the dark matter sector consists of a single particle χ with $U(1)_D$ charge of $+1$ and mass m_χ along with its antiparticle $\bar{\chi}$. For definiteness, we take χ to be a fermion, though our results are applicable to scalars as well. As the limits on new long range forces on SM fields are very stringent, we assume that all the SM fields are neutral under $U(1)_D$. For the moment we take the χ field to be a singlet under $SU(3)_C \times SU(2)_L \times U(1)_Y$, a restriction that will be relaxed in Section 4.4. As a result, this extension of the SM is anomaly free. In this Section, we will derive constraints on the mass m_χ and coupling $\hat{\alpha}$ from the evolution of dark matter in the early universe. Two considerations drive these constraints: the dark matter must provide the right relic abundance at thermal freeze-out, and the dark radiation from the $U(1)_D$ cannot contribute too greatly to relativistic degrees of freedom at BBN (a similar bound coming from the CMB also applies but is weaker).

The degrees of freedom in the dark sector are thus the heavy DM fermions χ

and massless dark photons $\hat{\gamma}$. The Lagrangian for the dark sector is

$$\mathcal{L} = \bar{\chi}(i\not{D} + m_\chi)\chi - \frac{1}{4}\hat{F}_{\mu\nu}\hat{F}^{\mu\nu}. \tag{4.1}$$

Here $D_\mu = \partial_\mu - i\hat{g}\hat{A}_\mu$ and $\hat{F}_{\mu\nu}$ is the field-strength tensor for the dark photons. We assume that the mixing term $c\hat{F}_{\mu\nu}F^{\mu\nu}$ is set to zero at some high scale (say the GUT scale). This is a self-consistent choice, since if there is no mixing between the dark and visible sectors, $c = 0$ is preserved by the renormalization group evolution. (In Section 4.4 we argue that mixing is not generated by radiative corrections even when χ carries $SU(2)_L$ quantum numbers.) This choice allows us to bypass constraints on a new $U(1)$ coming from mixing between the photon and dark photon, that is, 'paraphotons' [114, 103]. We have no *a priori* assumptions on the parameters m_χ and $\hat{\alpha}$, though as we shall see, it suffices to think of the former as $\mathcal{O}(100-1000\text{ GeV})$ and the latter $\lesssim \mathcal{O}(10^{-2})$.

We now follow the thermal history of the dark sector. Our analysis follows that of Ref. [109]; we rehearse it in a slightly simpler context here to illustrate how the results depend on our various assumptions. If the visible sector and the dark sector are decoupled from each other, they may have different temperatures, T and $\hat{T}$, respectively; rapid interactions between them would equilibrate these two values. After inflation, the two sectors could conceivably reheat to different temperatures, depending on the coupling of the inflaton to the various fields. Even if the temperatures are initially equal, once the two sectors decouple as the universe expands and cools, entropy deposited from frozen-out degrees of freedom in one sector will generally prevent the dark temperature $\hat{T}$ from tracking the visible sector

temperature T. The ratio

$$\xi = \hat{T}/T \tag{4.2}$$

will depend on the spectrum of both sectors, and is itself a function of T.

As the temperature drops below a particle's mass, the associated degrees of freedom freeze out and dump entropy into their respective sectors (dark or visible). This causes the temperature of that sector to decline more slowly than $1/a$, where a is the scale factor of the universe. As the entropy density s of the visible sector and $\hat{s}$ of the dark sector are individually conserved after decoupling, we must separately count the degrees of freedom in these two sectors. There are two definitions of degrees of freedom of interest to us: g_* and $g_{*\mathrm{S}}$. The former is defined as

$$g_* = \sum_{i=\mathrm{bosons}} g_i \left(\frac{T_i}{T}\right)^4 + \frac{7}{8} \sum_{i=\mathrm{fermions}} g_i \left(\frac{T_i}{T}\right)^4, \tag{4.3}$$

and is used in calculation of the total relativistic energy density, $\rho_R \propto g_* T^4$. Here g_i is the number of degree of freedom for particle species i, T_i is the temperature of the thermal bath of species i, and T is the temperature of the photon bath. The sums run over all active degrees of freedom at temperature T. Separating out the visible fields, g_* can be written as

$$g_* = g_{*\mathrm{vis}} + \sum_{i=\mathrm{bosons}} g_i \xi(T)^4 + \frac{7}{8} \sum_{i=\mathrm{fermions}} g_i \xi(T)^4, \tag{4.4}$$

where the sums now run over the dark particles. If we restrict the visible sector to the SM, then the term $g_{*\mathrm{vis}}$ is 106.75 above the top mass, dropping gradually to ~ 60 at $T = \Lambda_{\mathrm{QCD}}$. Between 100 MeV $\gtrsim T \gtrsim$ 1 MeV, $g_{*\mathrm{vis}} = 10.75$, and drops

again to 3.36 in the present day. (See, *e.g.*, Ref. [113] for more detail.)

Similarly, the total entropy density $s_{\rm tot}$ (a conserved quantity) at a photon temperature T is proportional to $g_{*\rm S}T^3$, where

$$g_{*\rm S} = \sum_{i=\rm bosons} g_i \left(\frac{T_i}{T}\right)^3 + \frac{7}{8}\sum_{i=\rm fermions} g_i \left(\frac{T_i}{T}\right)^3 \tag{4.5}$$

$$= g_{*\rm S,vis} + \sum_{i=\rm bosons} g_i \xi(T)^3 + \frac{7}{8}\sum_{i=\rm fermions} g_i \xi(T)^3 \,. \tag{4.6}$$

Prior to neutrino decoupling, all the relativistic standard model degrees of freedom are in thermal equilibrium at a common temperature. Thus, before $T \sim 1$ MeV when neutrinos decouple, we have $g_{*\rm vis} = g_{*\rm S,vis}$. Furthermore, we may split the dark $g_{*\rm S}$ into heavy and light degrees of freedom: $g_{\rm heavy}$ and $g_{\rm light}$, where the heavy degrees of freedom are non-relativistic at BBN. We are interested in the number of degrees of freedom at BBN ($T \sim 1$ MeV) because formation of the experimentally observed ratios of nuclei are very sensitive to the expansion of the universe at that time, which is related to the energy density of radiation through the Friedmann equation. From this, a bound on the number of relativistic degrees of freedom can be derived [109].

Using the separate conservation of the visible and dark sector entropy and the previous definitions, we see that at BBN

$$\frac{g_{\rm light}\xi(T_{\rm BBN})^3}{(g_{\rm heavy}+g_{\rm light})\xi(T_{\rm RH})^3} = \frac{g_{*\rm vis}(T_{\rm BBN})}{g_{*\rm vis}(T_{\rm RH})} \tag{4.7}$$

here we have set $g_{*\rm S,vis} = g_{*\rm vis}$ (recall that $g_{*\rm vis}(T_{\rm BBN}) = 10.75$). The BBN bound on relativistic degrees of freedom is usually stated in terms of number of light neutrino

species in thermal equilibrium at the time: $N_\nu = 3.24 \pm 1.2$ [115]. Here the error bars correspond to 2σ (95% confidence). Therefore, assuming three light neutrino species in the visible sector, if the dark sector is not to violate this bound, we must require

$$g_{\rm light}\xi(T_{\rm BBN})^4 = \frac{7}{8} \times 2 \times (N_\nu - 3) \leq 2.52 \quad (95\% \text{ confidence}). \tag{4.8}$$

Combining Eqs. (4.7) and (4.8), we find that

$$g_{\rm light}\left[\frac{g_{\rm heavy} + g_{\rm light}}{g_{\rm light}}\frac{10.75}{g_{*\rm vis}(T_{\rm RH})}\right]^{4/3}\xi(T_{\rm RH})^4 \leq 2.52 \quad (95\% \text{ confidence}). \tag{4.9}$$

Since the high energy completion of the visible sector must at minimum include the SM fields, $g_{*\rm vis}(T_{\rm RH}) \geq 106.75$; a bound on the dark sector $g_{\rm light}$ and $g_{\rm heavy}$ can be derived for a fixed value of $\xi(T_{\rm RH})$ (see Fig. 4.1). Increasing the number of visible sector degrees of freedom at high temperatures (i.e., to that of the MSSM) relaxes this bound.

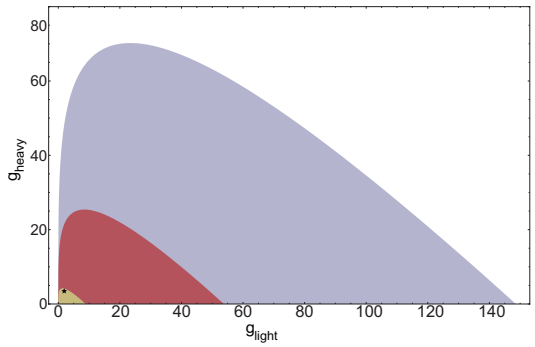

Figure 4.1: The allowed values of dark $g_{\rm light}$ (those degrees of freedom relativistic at $T_{\rm BBN}$) and $g_{\rm heavy}$ (the remaining dark degrees of freedom) arising from BBN constraints Eqs. (4.8) and (4.9). The allowed regions correspond to 95% confidence levels for $\xi(T_{\rm RH}) = 1$ and a visible sector $g_{*\rm vis} = 106.75$ (red), $\xi(T_{\rm RH}) = 1$ and $g_{*\rm vis} = 228.75$ (corresponding to MSSM particle content, in blue), and $\xi(T_{\rm RH}) = 1.4(1.7)$ and $g_{*\rm vis} = 106.75(228.75)$ (in yellow). The minimal dark sector model of this paper is noted by a black star at $g_{\rm light} = 2$ and $g_{\rm heavy} = 3.5$.

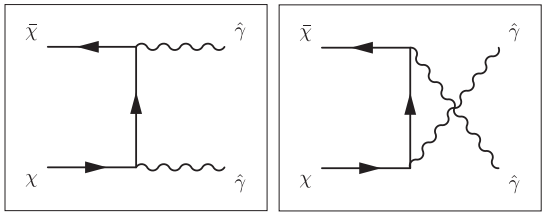

Figure 4.2: Pair annihilation/creation of dark matter χ into dark photons $\hat{\gamma}$ via t and u-channel exchange diagrams. These processes keep the dark sector in thermal equilibrium until the χ particles become non-relativistic.

In the case of $\xi(T_{\rm RH}) = 1$, we see that the minimal model of the dark sector (only heavy $\chi/\bar{\chi}$ and light $\hat{\gamma}$) is safely included. Due to the fourth power of ξ entering into Eq. (4.9), if the minimal dark sector is not to be ruled out, we find $\xi(T_{\rm RH}) \leq 1.4(1.7)$ for the SM(MSSM) particle content. A similar bound on relativistic degrees of freedom can be derived from the CMB, but provides a weaker 2σ exclusion limit [116, 109].

We now turn to bounds on the coupling $\hat{\alpha}$ and dark matter mass m_χ coming from the dark matter abundance. At temperatures $\hat{T}$ much above m_χ, the χ particles are kept in thermal equilibrium with the dark photons $\hat{\gamma}$ (and possibly other particles in the dark sector) via pair annihilation/creation as in the Feynman diagrams of Fig. 4.2. Since the annihilation can proceed via s-wave processes, the thermally averaged cross-section $\langle \sigma v \rangle$ is, to leading order, independent of v:[2]

$$\langle \sigma v \rangle \approx \sigma_0 = \frac{\pi \hat{\alpha}^2}{2 m_\chi^2} + \mathcal{O}(v^2). \tag{4.10}$$

Using this, the relic density of the χ particles may be easily calculated (see, for example Ref. [113]).

[2]Strictly speaking, there will be a Sommerfeld enhancement in this cross-section in the limit $v \to 0$ [117]. This will slightly change the relic abundance [118], but we leave the detailed analysis for future work.

As a rule of thumb, the dark matter drops out of thermal equilibrium when the rate Γ of annihilation $\chi\bar{\chi} \to \hat{\gamma}\hat{\gamma}$ (and the reverse process) is outpaced by the expansion of the universe H. Using the Boltzmann equation, the contribution of χ to the energy density of the universe can be more precisely calculated as

$$\Omega_{\rm DM}h^2 = 1.07 \times 10^9 \frac{(n+1)x_f^{n+1}\ {\rm GeV}^{-1}}{(g_{*\rm S}/\sqrt{g_*})m_{\rm Pl}\sigma_0}. \tag{4.11}$$

Here x_f is the ratio $m_\chi/\hat{T}_f$ where $\hat{T}_f$ is the dark temperature at time of freeze-out and $n = 0$ for s-wave processes. The quantity x_f is given by

$$x_f = \ln\left[0.038(n+1)\left(\frac{g}{\sqrt{g_*}}\right)m_{\rm Pl}m_\chi\sigma_0\right] - \left(n+\frac{1}{2}\right)\ln\ln\left[0.038(n+1)\left(\frac{g}{\sqrt{g_*}}\right)m_{\rm Pl}m_\chi\sigma_0\right], \tag{4.12}$$

where g is the number of degrees of freedom in the χ system (namely 4).

As g_* enters into the formula for x_f only logarithmically, we may make the approximation that $g_{*\rm S} \approx 100$ if χ freezes out while T is above $\Lambda_{\rm QCD}$. We make the additional assumptions that the only degrees of freedom in addition to the SM are the $\hat{\gamma}$ and χ in the dark sector and that $\xi(T_{\rm RH}) = 1$. We shall consider how these assumptions may be relaxed later.

Under these assumptions, the contribution of the dark sector to g_* and $g_{*\rm S}$ is $2 + (7/8) \times 4 = 11/2$. As no dark degrees of freedom have frozen out yet, $\xi(T_f) = \left(\frac{g_{*\rm vis}(T_f)}{g_{*\rm vis}(T_{\rm RH})}\right)^{1/3}\xi(T_{\rm RH}) \approx 1$. With the measured value $\Omega_{DM}h^2 = 0.106 \pm 0.08$ [4], we may solve for the allowed values of $\hat{\alpha}$ as a function of m_χ in Eq. (4.11). The resulting band is shown in Fig. 4.3.

In this discussion we have assumed that the process which sets the relic abun-

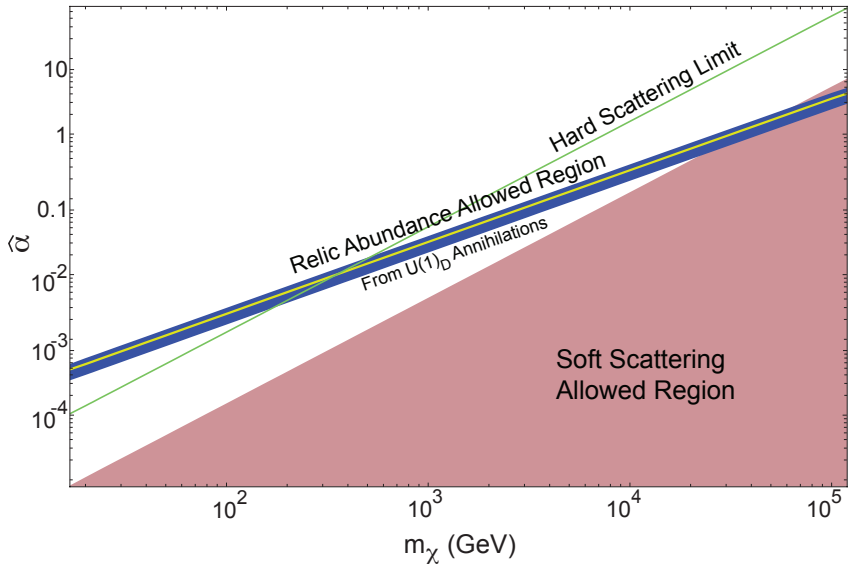

Figure 4.3: The allowed regions of $\hat{\alpha}$ vs. m_χ parameter space. The relic abundance allowed region applies to models in which $U(1)_D$ is the only force coupled to the dark matter; in models where the DM is also weakly interacting, this provides only an upper limit on $\hat{\alpha}$. The thin yellow line is the allowed region from correct relic abundance assuming $\Omega_{\rm DM}h^2 = 0.106 \pm 0.08$, $\xi(T_{\rm RH}) = 1$, $g_{*\rm vis} \approx 100$, and $g_{\rm heavy} + g_{\rm light} = 5.5$ while the surrounding blue region is $g_{*\rm vis} = 228.75(60)$, $\xi(T_{\rm RH}) = 1(0.1)$, and $g_{\rm heavy} + g_{\rm light} = 100(5.5)$ at the lower(upper) edge. The diagonal green line is the upper limit on $\hat{\alpha}$ from effects of hard scattering on galactic dynamics; in the red region, even soft scatterings do not appreciably affect the DM dynamics. We consider this to be the allowed region of parameter space.

dance of χ is annihilation into $\hat{\gamma}$s, as shown in Figure 4.2. As we will argue in the next section (and as is already shown in Figure 4.3), the values we obtain for $\hat{\alpha}$ from this calculation are incompatible with bounds from galactic dynamics unless $m_\chi > 10^5$ GeV (at which point $\hat{\alpha}$ is non-perturbative). However, we can get the correct relic abundance even with much lower values of $\hat{\alpha}$ by adding other annihilation channels, such as the weak interactions, as explored in Section 4.4. In that case, the "relic abundance allowed region" discussed here really becomes an upper limit; if the dark fine-structure constant is larger than that value, annihilations are too efficient, and the correct abundance cannot be obtained.

We now consider how changing our assumptions on g_* and ξ can change our conclusions on the allowed parameter space. The parameter $\xi(T_f)$ does not enter explicitly into the calculation for $\Omega_{\rm DM}h^2$, however it does affect the number of active degrees of freedom at freeze-out directly, through Eqs. (4.4) and (4.6), and indirectly by allowing the temperature T to differ from $\hat{T}$. If $\xi < 1$, $\hat{T} < T$ and there could be many more heavy visible degrees of freedom still active when χ freezes out. $\xi > 1$ would reduce the visible degrees of freedom. However, as we have seen in Eq. (4.9), it is difficult to construct a scenario with large ξ, short of a massive increase in $g_{*\rm vis}$ and small values of $g_{*\rm heavy} + g_{*\rm light}$. We include in Fig. 4.3 the bounds from both a large and small value of g_*. The large limit is $g_{*\rm vis}(T_f) = 228.75$, (*i.e.* equivalent to the MSSM degrees of freedom), $\xi(T_{\rm RH}) = 1$, and $g_{\rm heavy} + g_{\rm light} = 100$, while the small value is given by $g_{*\rm vis}(T_f) = 60$, (*i.e.* equivalent to the SM degrees of freedom at $\Lambda_{\rm QCD}$), $\xi(T_{\rm RH}) = 0.1$, and $g_{\rm heavy} + g_{\rm light} = 5.5$.

4.3 Galactic Dynamics

Although freezeout in our scenario is similar to that in the standard WIMP scenario, the long-range DM-DM interactions implied by the unbroken $U(1)_D$ may lead to considerably different DM phenomenology in the current Universe, and in particular in galactic halos. In this scenario, dark-matter halos are composed of an equal mixture of χ and $\bar{\chi}$. The overall halo will be $U(1)_D$ neutral, eliminating long-range forces that are incompatible with experiment.

However, nearest-neighbor interactions between χ particles remain, and these interactions can be constrained by observations that suggest that dark matter is effectively collisionless. Constraints to dark-matter self-interactions arise from evidence for nonspherical cores for some dark-matter halos (collisions tend to make the cores of halos round) [119] and from evidence for dark-matter halos with large phase-space densities (collisions would reduce phase-space densities) [99, 120, 121]. Roughly speaking, a bound to DM-DM interactions can be derived by demanding that scattering induces no more than a small fractional change in the energy of a typical DM particle in a galactic halo during the history of the Universe [14]. This translates to an upper bound of ~ 0.1 cm^2/g on the more familiar quantity σ/m_χ.[3] A separate bound of $\sigma/m_\chi < 1.25$ can be derived from the Bullet Cluster [122, 123], but as this is less restrictive we ignore it here.

To illustrate, we first consider hard scattering of a χ off another χ or $\bar{\chi}$, where energy on the order of $m_\chi v^2/2$ is exchanged. The mean free time τ for a χ to

[3] This can be seen from Eq. (4.13), using the age of the universe for τ, and Galactic parameters $\rho = nm_\chi = 0.3$ GeV/cm^3, $v/c = 10^{-3}$.

undergo a hard scattering with another $\chi(\bar{\chi})$ is given by

$$\tau = \frac{1}{\langle n\sigma v\rangle}, \tag{4.13}$$

where n is the number density of dark matter, σ is the hard-scattering cross-section, and v is the velocity of the dark-matter particles. The number N of dark-matter particles in the Galaxy is

$$N = \frac{M_{\rm Gal}}{m_\chi} \approx 10^{64} \left(\frac{m_\chi}{\rm TeV}\right)^{-1}, \tag{4.14}$$

and $n \approx 3N/4\pi R^3$, where R is the radius of the Galaxy. The velocity v is

$$v \simeq \sqrt{\frac{GM_{\rm Gal}}{R}} \simeq \sqrt{\frac{GNm_\chi}{R}}. \tag{4.15}$$

The dynamical time $\tau_{\rm dyn}$ in the Galaxy is

$$\tau_{\rm dyn} = 2\pi R/v. \tag{4.16}$$

Taking $\tau_{\rm dyn} \approx 2 \times 10^8$ years for the Milky Way, the average time for a hard scatter for a dark-matter particle is greater than the age of the universe if

$$\frac{\tau}{\tau_{\rm dyn}} = \frac{2R^2}{3N\sigma} \gtrsim 50. \tag{4.17}$$

A hard scatter occurs when two particles pass close enough so that their kinetic energy is comparable to their potential energy. The impact parameter that defines

a hard scatter is thus

$$b_{\rm hard} = \frac{2\hat{\alpha}}{v^2 m_\chi}. \tag{4.18}$$

Taking the cross-section for hard scatters to be $\sigma_{\rm hard} \approx b_{\rm hard}^2$, and using Eq. (4.15) for v, we find

$$\frac{\tau_{\rm hard}}{\tau_{\rm dyn}} = \frac{G^2 m_\chi^4 N}{6\hat{\alpha}^2} \gtrsim 50. \tag{4.19}$$

Using $G = m_{\rm Pl}^{-2} \approx 10^{-32}$ TeV^{-2} we find the hard scattering limit on the $U(1)_D$ coupling constant to be

$$\hat{\alpha} \lesssim \sqrt{\frac{1}{300}} \left(\frac{m_\chi}{\rm TeV}\right)^{3/2} = 0.06 \left(\frac{m_\chi}{\rm TeV}\right)^{3/2}. \tag{4.20}$$

The allowed region arising from this bound is shown in Fig. 4.3.

We now turn to the effect of soft-scattering on the allowed values of $\hat{\alpha}$ and m_χ. Here we consider the approach of one χ particle towards another $\chi(\bar{\chi})$ at impact parameter b. By definition, for soft-scattering $b > b_{\rm hard}$. The velocity change induced by the encounter is

$$\delta v = \pm \frac{2\hat{\alpha}}{m_\chi b v}. \tag{4.21}$$

As one dark-matter particle orbits the Galaxy, it sees a surface density $N/\pi R^2$ of dark matter. The number of interactions that occur between an impact parameter b and db is $\delta n = (N/\pi R^2) 2\pi b db$. While the change in δv over these interactions should average to zero, this is not true for δv^2:

$$\delta v^2 = (\delta v)^2 \delta n = \frac{8\hat{\alpha}^2 N}{m_\chi^2 v^2 R^2} b^{-1} db. \tag{4.22}$$

Integrating δv^2 from $b_{\rm hard}$ to the maximum possible impact parameter in the Galaxy, R, gives the total change in v^2 as the particle orbits once through the halo:

$$\Delta v^2 = \frac{8\hat{\alpha}^2 N}{m_\chi^2 v^2 R^2} \ln(R/b_{\rm hard}) = \frac{8\hat{\alpha}^2 N}{m_\chi^2 v^2 R^2} \ln\left(\frac{GNm_\chi^2}{2\hat{\alpha}}\right). \tag{4.23}$$

The number $\tau/\tau_{\rm dyn}$ of orbits it will take for the dark-matter particle to have $\Delta v^2/v^2 \sim \mathcal{O}(1)$ is

$$\frac{\tau_{\rm soft}}{\tau_{\rm dyn}} = \frac{G^2 m_\chi^4 N}{8\hat{\alpha}^2} \ln^{-1}\left(\frac{GNm_\chi^2}{2\hat{\alpha}}\right) \gtrsim 50. \tag{4.24}$$

The logarithmic suppression in Eq. (4.24) relative to Eq. (4.19) is due to the long-range Coulomb force generated by the $U(1)_D$. As can be seen in Fig. 4.3, the allowed region from these considerations of Galactic dynamics completely exclude the $\hat{\alpha}/m_\chi$ band that gives the correct relic abundance up to $m_\chi \sim 30$ TeV. For $m_\chi \sim 1$ TeV a dark matter candidate which freezes out due to $U(1)_D$ interactions is ruled out from such considerations. In particular, models such as that in Ref. [109] with $m_\chi \sim m_W$ and a hidden copy of electromagnetism (*i.e.* $\hat{\alpha} = 1/137$) are ruled out, even though the freeze-out proceeds through hidden-sector weak interactions rather than a $U(1)_D$. Interestingly, $\hat{\alpha} = \alpha$ is allowed for $m_\chi \gtrsim 2$ TeV.

Before considering whether such a model may be valid if our assumptions are loosened, we should ask why Galactic dynamics do not similarly exclude WIMP dark matter. After all, both models have similar cross sections for annihilations in the early universe (Eq. (4.10)) as is required for the correct relic density. Though the soft-scattering limit clearly will not apply due to the short range nature of the broken $SU(2)_L$, naively it would seem that the hard scattering limit Eq. (4.19) should apply to WIMPs equally well. However, notice that the threshold for hard

scattering with a $U(1)_D$ is dependent on energy. As the temperature drops, the cross-section rises, as the χ particles no longer have to approach as close in order for to potential energy $V(r)$ to be of the order of the kinetic energy. Contrast this to hard scattering from WIMPs, where the cross-section is always proportional to $\alpha^2/m_{\rm DM}^2$, regardless of the velocity. Entering this cross-section into Eq. (4.17), results in the uninteresting bound that $m_{\rm DM} \lesssim 10^{13}$ TeV for WIMP dark matter from Galactic dynamics constraints.

It is difficult to see any way of avoiding the bounds from Galactic dynamics, so we look to loosen the limits derived in Section 4.2. Clearly if the interaction responsible for freezing out the relic density is not the $U(1)_D$ constrained by soft-scattering, then $\hat{\alpha} \lesssim 10^{-3}$ is not ruled out. We consider such examples in the next Section. However, we first consider the possibility that our assumptions in deriving the relic density are too conservative.

From Eq. (4.11), if we reduce $\hat{\alpha}$ (and therefore σ_0) in order to satisfy the scattering bounds, we must either decrease x_f or increase $g_{*\rm S}/\sqrt{g_*}$. In lowering $\hat{\alpha}$ by a minimum of two orders of magnitude, $x_f/(g_{*\rm S}/\sqrt{g_*})$ must likewise increase. As x_f depends only logarithmically on $\hat{\alpha}$ and the number of degrees of freedom, so it is hard to see how it it could be increased sufficiently to counterbalance $\hat{\alpha}$ of order 10^{-3} (rather than $\hat{\alpha} \sim 10^{-2}$). We conclude that the number of effective degrees of freedom must be increased. From Eqs. (4.4) and (4.6), we see that if $\xi = 1$, then at freeze-out we must have

$$\frac{g_{*\rm S}}{\sqrt{g_*}} = \sqrt{\sum_{i=\rm bosons} g_i + \frac{7}{8} \sum_{i=\rm fermions} g_i} \sim 10^2. \tag{4.25}$$

From Eq. (4.9), these $\sim 10^4$ degrees of freedom must exist in the visible sector at T_f, rather than the dark sector.

Alternatively, we could imagine that there are no (or few) new particles beyond the minimum χ and $\hat{\gamma}$ at freeze-out, but instead $\xi \gg 1$. In this limit

$$\frac{g_{*\mathrm{S}}}{\sqrt{g_*}} \approx \xi \sim 10^2. \tag{4.26}$$

This limit is more troublesome; from Eq. (4.9) we saw that large values of ξ at the reheating scale (and subsequently T_f) very quickly violate the bounds on relativistic degrees of freedom at BBN. Clearly, by increasing the number of degrees of freedom in the visible sector, this bound could be avoided as well. However, we are left with the conclusion that either $\xi(T_f) \sim 10^2$ or there exist $\sim 10^4$ new particles at a few hundred GeV to a TeV. We leave it to the reader to decide how palatable these alternatives are.

A separate, but conceptually similar, bound on scattering can be placed by considering the interaction of galactic dark matter with the hotter DM of the surrounding cluster. Scattering will cause heating in galactic DM, and eventually evaporate the halo. From Ref. [124] the characteristic time for this evaporation is given by

$$t_{\mathrm{evap.}} = 3.5 \times 10^9 \text{ years} \left(\frac{\sigma/m_\chi}{\mathrm{cm}^2/\mathrm{g}}\right)^{-1} \left(\frac{v_{\mathrm{cluster}}}{10^3 \mathrm{km/s}}\right)^{-1} \left(\frac{\rho_{\mathrm{cluster}}}{1.3 \times 10^{-3} M_\odot \mathrm{pc}^{-3}}\right)^{-1}. \tag{4.27}$$

We may estimate the cross-section for soft-scattering by calling the path length λ over which a single particle looses of order its initial kinetic energy $(\Delta v^2/v^2)^{-1} R$, where R is the radius of the galaxy, and $\Delta v^2/v^2$ from Eq. (4.23) is the fractional

energy loss as the particle travels once through the halo. This can be expressed as an effective scattering cross-section by setting $\lambda = (n\sigma)^{-1}$, where $n = N/R^3$ is the number density of DM in the halo, we find

$$\frac{\sigma}{m_\chi} \approx \frac{8\hat{\alpha}^2}{m_\chi^3 v^4} \ln\left(\frac{GNm_\chi^2}{2\hat{\alpha}}\right). \tag{4.28}$$

Letting the cluster velocity and density take on the canonical values ($v_{\rm cluster} = 10^3$km/s and $\rho_{\rm cluster} = 1.3\times10^{-3} M_\odot {\rm pc}^{-3}$, where $M_\odot$ is the solar mass), we can place limits on $\hat{\alpha}$ and m_χ by requiring that $t_{\rm evap.}$ is longer than the age of the universe. Numerically, we find this bound less stringent than that from soft-scattering of particles within the Galactic halo, Eq. 4.24.

It is interesting to note that, aside from logarithmic enhancements, the bound placed on $\hat{\alpha}$ vs. m_χ parameter space from soft-scattering is essentially a line of constant σ/m_χ (that is, they are, up to log corrections, lines of slope 2/3 on the log-log plot). As mentioned, limiting DM to one hard scattering in the lifetime of the universe is equivalent to bounding σ/m_χ in the Galaxy to be $\lesssim 0.1$ cm^2/g. It has been suggested in the literature that values of σ/m_χ in the range $0.01 - 5$ cm^2/g [119, 99, 120, 121] may provide better agreement between simulation and observation. Therefore, our limit from soft-scattering should be considered as the general region at which interaction effects may become relevant. Additionally, from Eq. (4.28) as $\sigma/m_\chi \propto v^{-4}$, it should be expected that the soft-scattering bound will vary greatly in DM systems with a range of virial velocities v. In particular, we surmise that a bound even stronger than that estimated here can be obtained from the dwarf galaxies that exhibit the highest observed dark-matter phase-space

densities [125].

4.4 Weakly Coupled Models

In this Section, we examine an expanded version of our minimal model: one in which the χ dark matter particles possess $SU(2)_L$ quantum numbers in addition to a $U(1)_D$ charge. For such $SU(2)_L \times U(1)_D$ particles, the cross-section for freeze-out in the early universe is dominated by the weak interaction $\sigma \sim \alpha^2/m_\chi^2$, and the $U(1)_D$ contribution is negligible for the small values of $\hat{\alpha}$ under consideration. At late times the situation is reversed. The weak cross-section remains small, as it is the result of a short-range force. However the long range cross-section for soft-scattering increases as the dark matter cools and slows, as exemplified in Eq. (4.23). This allows the strength of $\hat{\alpha}$ to be $\sim 10^{-3}$ as required by Galactic dynamics without running afoul of the relic density conditions, which would require $\hat{\alpha} \sim 10^{-2}$ (when $m_\chi \sim 1$ TeV).

We therefore take our Dirac fermion χ to be a $(\mathbf{1}, \mathbf{n})_{Y,D}$ multiplet of $SU(3)_C \times SU(2)_L \times U(1)_Y \times U(1)_D$, where we shall take the $U(1)_D$ coupling to be in the region of Fig. 4.3 allowed by soft-scattering. Thus $\hat{\alpha} \lesssim 10^{-3}$. The behavior of this model in the early universe is very similar to the 'minimal dark model' of Ref. [126], from which we take many of our constraints.

In outlining our original model in section 4.2, we set the coefficient of the mixing term $F_{\mu\nu}\hat{F}^{\mu\nu}$ to zero at the high scale. Clearly loops involving χ would generate a non-zero mixing if the χ field possesses non-zero hypercharge Y. In order to avoid this complication, we set $Y = 0$.

Our χ particle must be neutral under $U(1)_{EM}$. With the assumption of $Y = 0$,

this requires χ to sit in an n-plet of $SU(2)_L$ where n is odd (*i.e.* $n = 3, 5, \ldots$). In the spirit of simplicity we take $n = 3$, so the χ triplet contains the neutral χ^0 and (electromagnetically) charged $\chi^\pm$, all with $U(1)_D$ charges of $+1$. Due to $SU(2)_L$ loops, the $\chi^\pm$ are 166 MeV heavier than the χ^0, and decay before BBN. If the dark matter mass is $m_\chi = 2.4$ TeV, the correct dark matter abundance (including production and then decay of $\chi^\pm$) results from thermal freeze out (see Ref. [126]). We note that our model does have the nice feature of automatically suppressing unwanted decays of χ into SM particles, as by assumption χ is the lightest particle charged under $U(1)_D$.

This minimal model is anomaly free. Triangle diagrams with one or three $SU(2)_L$ vertexes vanish by the tracelessness of the $SU(2)_L$ generators. The diagrams consisting of an odd number of $U(1)_D$ vertexes also vanish as the dark sector contains only two Weyl fermions, one with $+1$ under $U(1)_D$, and the other with -1.

This model does not run afoul of BBN (or CMB) bounds. As in the pure $U(1)_D$ theory, the only new relativistic degrees of freedom at BBN are the two from the $\hat{\gamma}$. Due to the interactions between χ and the weakly charged SM fields, we expect the temperatures T and $\hat{T}$ to track, so $\xi = 1$ until the χ freeze-out. With small values of $\hat{\alpha}$, the dark photons may freeze-out earlier, and would thus be colder. However, if we take the worse-case scenario that the dark photons do not decouple until after the χ undergo freeze-out we find (from Eq. (4.9)) that BBN bounds are satisfied as long as freeze-out occurs when

$$g_{*\mathrm{vis}} \geq 18.8. \tag{4.29}$$

This is easily satisfied for any model that freezes out before the QCD phase transi-

tion.

Next we must check that our χ does not have too large of a coupling to SM particles. We first demonstrate that no mixing occurs between the photon and the dark photon $\hat{\gamma}$. As indicated previously, we assume that there is no $F_{\mu\nu}\hat{F}^{\mu\nu}$ term at high energies. With purely $SU(2)_L \times U(1)_D$ coupling, we find that the diagram Fig. 4.4a vanishes. This is because any such vertex can be rewritten as the $\hat{\gamma}$ coupling to a χ or $\bar{\chi}$ which then couples to the γ through some vertex involving SM fermions and $SU(2)_L$ couplings (Fig. 4.4b). However, since the mass and $SU(2)_L$ couplings of χ are the same as those of $\bar{\chi}$ yet the $U(1)_D$ charge is opposite, the sum of the two diagrams is zero.

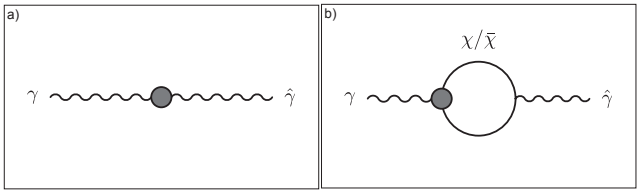

Figure 4.4: Feynman diagrams leading to $\gamma/\hat{\gamma}$ mixing. The vertex in a) can be expanded into that shown in b), as the only particle to which the $\hat{\gamma}$ couples is $\chi/\bar{\chi}$. Since the mass and $SU(2)_L$ charge of these two particles are the same, yet they possess opposite $U(1)_D$ charge, the sum of the χ and $\bar{\chi}$ diagrams in b) is zero, and the overall mixing vanishes.

Similarly, the coupling between $\hat{\gamma}$ and a standard model fermion f is also zero. The relevant diagrams are shown in Fig. 4.5. Again, the vertex between f and $\hat{\gamma}$ (Fig. 4.5a) can be divided into the $\chi/\bar{\chi}$ vertex connecting with $\hat{\gamma}$ and a vertex between $\chi/\bar{\chi}$ vertex connecting with f (Fig. 4.5b). As the latter vertex is identical for χ and $\bar{\chi}$ but the former has opposite signs, the overall diagram vanishes.

The lowest order coupling of SM fermions to $\hat{\gamma}$ occurs at $\alpha^2\hat{\alpha}$. This is due to a two loop effect, as shown in Fig. 4.6, and unlikely to be accessible in direct detection. We can represent this interaction by an effective Lagrangian whose lowest order term

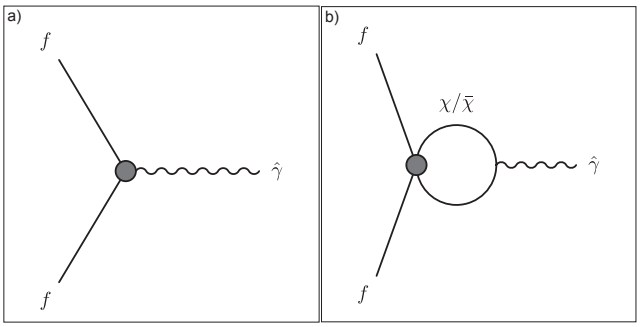

Figure 4.5: Feynman diagram leading to $\hat{\gamma}$ interactions with SM fermions f. The vertex in a) can be expanded into that shown in b), as the only particle with an interaction with $\hat{\gamma}$ is the $\chi/\bar{\chi}$. Since the mass and $SU(2)_L$ charge of these two particles are the same, yet the $U(1)_D$ charges are opposite, the sum of the χ and $\bar{\chi}$ diagrams in b) is zero, and the overall coupling of f to $\hat{\gamma}$ is therefore zero as well.

is given by $\frac{\beta}{m_\chi^3}\hat{F}_{\mu\nu}\hat{F}^{\mu\nu}\bar{f}f$ where $\beta = \lambda_f\frac{\alpha^2\hat{\alpha}}{4\pi}$ and λ_f is the Yukawa coupling of the fermion that is involved. Let us estimate the order of magnitude of this interaction. To be conservative we use the Yukawa coupling of a u quark and take $\hat{\alpha} = 10^{-2}$; which by galactic dynamics is the maximum allowed value for $m_\chi \sim 2$ TeV. With these values we find $\beta \sim 10^{-10}$ and $\frac{\beta}{m_\chi^3} \sim 10^{-20}\,\text{GeV}^{-3}$. We estimate that the interaction length for dark photons inside the cores of stars would be on the order of 10^{18} km, and thus this interaction would not introduce a potentially dangerous new source of stellar cooling.

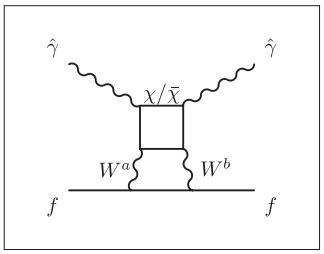

Figure 4.6: The leading order interaction of the dark sector with SM fermions. The dark photons $\hat{\gamma}$ couple to a loop of χ particles, which couple through two $SU(2)_L$ gauge bosons to SM fermions. Coupling through a single $SU(2)_L$ boson is zero due to the tracelessness of τ^a.

Due to the high-order interaction between $\hat{\gamma}$ and SM particles, we cannot expect

to directly observe the dark radiation. In addition, while the χ fields would have a direct detection cross-section of $10^{-44} - 10^{-45}$ cm^2 [126] and so could be seen in SuperCDMS, any such detection would be indistinguishable from a scenario without the dark photons. Therefore, the presence of a new unbroken $U(1)_D$ in the dark sector could only be probed via its effect on galactic dynamics. Clearly in the limit that $\hat{\alpha} \to 0$, the Galactic structure would remain unchanged. Values of $\hat{\alpha}$ near the maximum allowed from soft-scattering (*i.e.* $\hat{\alpha} \sim 10^{-2}$ for the $SU(2)_L$ triplet candidate with $m_\chi \sim 2$ TeV) should have a measurable effect on the halo structure, as in this regime the dark matter is no longer completely collisionless. A full study of this effect requires simulations beyond the scope of this paper, though some additional considerations are discussed in the following section.

4.5 Other Effects of Dark Photons

The existence of a dark matter 'plasma' may have additional effects that could significantly affect structure formation. We mention three possibilities here: bremsstrahlung, early universe structure formation, and the Weibel instability in galactic halos. The first two result in much weaker bounds than those already derived, and are mentioned here only for completeness. The Weibel instability may have significant and visible effects in the halo, but requires simulation beyond the scope of this paper.

4.5.1 Bremsstrahlung

Emission of a soft $\hat{\gamma}$ during a $\chi/\bar{\chi}$ collision could conceivably serve as another energy loss mechanism in the halo on par with soft and hard scattering as outlined in section 4.3. To derive a bound on $\hat{\alpha}$ as related to m_χ, we make the same assumption

as in the case of soft scatter: over the lifetime of the universe, a dark-matter particle cannot lose on order of its initial kinetic energy through bremsstrahlung of dark radiation. By assuming dipole radiation during a soft collision, we find that

$$\frac{3}{64}\frac{Gm_\chi^3 R}{\hat{\alpha}^3}\ln^{-1}\left(\frac{GNm_\chi^2}{2\hat{\alpha}}\right) \geq 50. \tag{4.30}$$

However this bound is weaker than that from both hard and soft-scattering over the parameter space of interest.

4.5.2 Structure Formation

In the early universe, structure cannot grow until after matter/radiation equality. Until the matter (which can clump) decouples from the dark radiation (which cannot), density perturbations remain fixed. We can estimate the scale factor at which this occurs by finding the redshift z_* at which the dissipation time (the time over which the velocity of a dark matter particle is significantly perturbed by the radiation) becomes longer than the Hubble time H^{-1}. The argument follows that in Ref. [127] for the decoupling of baryons from the photon bath.

The dissipation time is the logarithmic derivative of the velocity:

$$t_{\rm diss}^{-1} \equiv v^{-1}\frac{dv}{dt} = v^{-1}\frac{F}{m_\chi}\,. \tag{4.31}$$

Here F is the force due to radiation pressure,

$$F = \frac{4}{3}\hat{\sigma}_T a\hat{T}^4 v\,, \tag{4.32}$$

where

$$\hat{\sigma}_T = \frac{8\pi}{3}\frac{\hat{\alpha}^2}{m_\chi^2} \tag{4.33}$$

is the Thomson cross-section for dark matter interacting with dark photons and (as before) $\hat{T}$ is the temperature of the dark photons. As we shall see, the decoupling occurs when the universe is radiation dominated, so the Hubble time is given by

$$H^2 = \frac{4\pi^3}{45} g_* \frac{T^4}{m_{\rm Pl}^2}. \tag{4.34}$$

Here T is the photon temperature.

The conservation of entropy relates the photon temperature T at redshift z_* with the photon temperature today, T_0,

$$T = \left(\frac{g_{*\,S}(T_0)}{g_{*\,S}(T)}\right)^{1/3} \frac{T_0}{a}. \tag{4.35}$$

Combining Eqs. (4.31) and (4.34), we find the decoupling redshift z_* to be

$$\begin{aligned} 1 + z_* &= \frac{3}{16}\sqrt{\frac{\pi}{5}}\xi^{-4}\frac{m_\chi^3}{\hat{\alpha}^2 T_0^2 m_{\rm Pl}} g_*(T)^{1/2} \left(\frac{g_{*S}(T)}{g_{*S}(T_0)}\right)^{2/3} \\ &= 2.3\times 10^{18}\xi^{-4}\left(\frac{10^{-2}}{\hat{\alpha}}\right)^2 \left(\frac{m_\chi}{\rm TeV}\right)^3 g_*(T)^{1/2}\left(\frac{g_{*S}(T)}{g_{*S}(T_0)}\right)^{2/3}. \end{aligned} \tag{4.36}$$

As before ξ is the ratio of dark photon temperature to photon temperature at redshift z_* (recall that it is difficult to construct models where ξ is much larger than unity). The number of degrees of freedom that contribute to the entropy density today, $g_{*\,S}(T_0)$, is of order unity. The decoupling occurs extremely early, before even dark matter freeze-out.[4] As a result, it seems that this effect will be cosmologically

[4]This is not a contradiction: freeze-out is the time when the dark particles and antiparticles stop

irrelevant.

4.5.3 Plasma Instabilities

In Section 4.3, we constrained $\hat{\alpha}$ by demanding that dark matter be effectively collisionless in galactic halos, under two-body interactions. However, there may be collective plasma effects that affect DM dynamics on timescales much shorter than those due to two-body interactions. Unfortunately, it is difficult to state with confidence what the observational consequences of those effects will actually be, even if they are relevant. Given theoretical uncertainties about the nonlinear evolution of such instabilities, we leave the detailed implications to future work.

As a simple example we consider the Weibel instability [128], an exponential magnetic-field amplification that arises if the plasma particles have an anisotropic velocity distribution. Such anisotropies could arise, for example, during hierarchical structure formation as subhalos merge to form more massive halos. Similar instabilities in the baryonic gas have been postulated to account for the magnetic fields in galaxy clusters [129]. The growth rate Γ of the magnetic field is

$$\Gamma = \omega_p \frac{v}{c} = \sqrt{\frac{(4\pi)^2 \hat{\alpha} \rho}{m_\chi^2}} \frac{v}{c}, \tag{4.37}$$

where ω_p is the plasma frequency, $\rho \approx 0.4$ GeV/cm^3 is the dark-matter density, and v is the velocity of the dark matter within the colliding halos. Assuming $v/c \sim 10^{-3}$, we find

$$\Gamma \sim 10^{-2} \mathrm{s}^{-1} \times \frac{\hat{\alpha}^{1/2}}{(m_\chi/\mathrm{TeV})}. \tag{4.38}$$

annihilating, while decoupling occurs when the dark photons stop imparting significant velocity to the dark matter.

To be relevant for galactic-halo formation, the timescale Γ^{-1} for magnetic-field amplification should be shorter than the dynamical timescale τ of the merging sub-halos. The instability will be therefore of interest when

$$\left(\frac{m_\chi}{\text{TeV}}\right) \lesssim 10^{11}\hat{\alpha}^{1/2}\left(\frac{\tau}{10^6 \text{ yrs}}\right). \tag{4.39}$$

This range of $\hat{\alpha}$ and m_χ encompasses the entire parameter space of interest for any reasonable value of τ. Therefore, we suspect that galactic structure will be affected by plasma effects in the dark matter due to the $U(1)_D$ even when $\hat{\alpha}$ is not near the boundary of allowed values from soft-scattering. One possibility is that nonlinear evolution would result in a strongly magnetized plasma, and if so, dark matter would be effectively collisional and thus probably inconsistent with data. However, theory and simulations that study the nonlinear evolution of the Weibel instability for relativistic pair plasmas and nonrelativistic electron-proton plasmas do not yet agree whether the magnetic fields survive, and simulations for the equal-mass nonrelativistic plasma we are considering have not been performed. It is therefore premature to conclude that these instabilities will result in effectively collisional dark matter; a more detailed study will be required to assess these effects.

4.6 Conclusions

Given how little direct information we have about the nature of dark matter, it is of crucial importance to explore models in which the DM sector has an interesting phenomenology of its own. In many ways, an unbroken $U(1)$ gauge field coupled to dark matter is a natural way to obtain a long-range interaction between DM particles.

In contrast to the case of hypothetical long-range scalar fields, the masslessness of the gauge field is protected by a symmetry, and the absence of long-range violations of the equivalence principle is naturally explained by the overall charge neutrality of the dark plasma. New unbroken $U(1)$'s can appear naturally in unified models.

While a dark $U(1)$ may be realized as a broken symmetry with massive vector bosons, it has been pointed out that there are few constraints on the massless, unbroken case from the early universe. We have verified that the minimal model, with just a single massive Dirac fermion for the dark matter and a massless dark photon, is consistent with limits obtained from the number of relativistic degrees of freedom at BBN, with relatively mild assumptions on the reheating temperature of the dark sector. More complicated models are also allowed, depending on the details of spectrum and reheating.

We found that one cannot build a dark matter model charged under a hidden unbroken $U(1)_D$ in which this new gauge group is responsible for thermal freeze out. As can be seen in Fig. 4.3, the required values of $\hat{\alpha}$ and m_χ required for the χ particles to form a thermal relic would violate bounds coming from limits on hard and soft-scattering of dark matter in the Galactic halo. As an important consequence of this argument, models in which dark matter couples to an exact copy of ordinary electromagnetism (in particular, with $\hat{\alpha} = \alpha$) are ruled out unless $m_\chi >$ a few TeV. This constrains the parameter space of models with hidden copies of the SM or the MSSM in which the dark matter is electrically charged, such as the model in Ref. [109] where the stau was suggested as a dark matter candidate.

By adding additional interactions to increase the annihilation cross-section, it is possible to build a scenario with an unbroken dark $U(1)$ and the correct relic abun-

dance. Introducing another short-range force coupling to the χ, for example the familiar $SU(2)_L$, can provide an appropriately large cross-section for $\chi/\bar{\chi}$ annihilation. The new coupling $\hat{\alpha}$ must then be relatively small (compared to the $SU(2)_L$ α) in order to evade Galactic dynamics bounds.

The simplest model which realizes this situation is a Dirac fermion in a triplet of $SU(2)_L$ (in order to avoid $U(1)_Y/U(1)_D$ mixing). Bounds from the early universe then force m_χ to be on the order of a few TeV, which implies $\hat{\alpha} \lesssim 10^{-2}$. Since all couplings between the dark radiation and the SM enter at two loops (and require two dark photons in the process), it would be very difficult to observe the presence of the new gauge group through direct detection. Instead, the best search strategy would be an indirect one: looking for the effects on galactic dynamics arising from a soft-scattering mediated by a long-range force. Clearly, as $\hat{\alpha}$ goes to zero, the model becomes indistinguishable from minimal weakly coupled dark matter. However, if the coupling is near the limit from soft-scattering, one would expect detectable deviations from the assumptions of collisionless dark matter currently used in simulations.

Additionally, since the $U(1)_D$ effectively makes the dark halo a plasma (albeit a very cold, tenuous one), there may be other effects on structure formation that constrain this model [130]. We have estimated that the timescale for the Weibel instability in our model is short compared to relevant timescales for galactic dynamics. If this instability has a dramatic effect when subhalos collide during the assembly of a galactic halo, our $U(1)_D$ could be excluded for the entire range of interesting parameters. Further work is required to before we can reliably understand the quantitative effects of such instabilities on galactic dynamics.

This work opens a window to new phenomenological possibilities within the dark sector. One avenue for further investigation would be the possibility of "dark atoms," which would arise if there were two different stable species with dark charge, each with an asymmetry in the number density of positive and negative charges (with one balancing the other to maintain overall charge neutrality). From there, one is free to contemplate dark chemistry and beyond. Dark matter constitutes a large majority of the matter density of the universe, and there is no reason to assume *a priori* that physics there is any less rich and interesting than that of ordinary matter.

Chapter 5

Light Scalars and the Generation of Density Perturbations During Preheating or Inflaton Decay

Measurements of the cosmic microwave background radiation [132, 133] have clearly shown the presence of super-horizon primordial density fluctuations at roughly one part in 10^5. Inflation provides a natural explanation for such density fluctuations, since vacuum fluctuations of the inflaton (or any other light scalar field) get pushed outside of the horizon and enter at a much later time as classical density perturbations [134]. Recently, Dvali, Gruzinov and Zaldarriaga [135, 136] and Kofman [137] (DGZK) have shown in a number of scenarios how the interactions of such additional light fields to, e.g. the inflaton, could also generate adiabatic density fluctuations, independent of those created by the inflaton dynamics. In this scenario the size of non-Gaussian perturbations can be much larger than what occurs in single-field inflationary models [136, 138].

This is achieved by coupling a light scalar field to a heavier field that at some time subsequent to inflation dominates the energy of the Universe, such that the particle properties of this heavier field are modified by the fluctuations of the light field.

When the heavier particle decays, spatial fluctuations in either its mass or its decay width generate energy density perturbations in the radiation. This is because before reheating the universe is matter dominated, with the oscillating heavier particle dominating the total energy density, while after the decay the universe is radiation dominated. As the energy density in matter redshifts slower than energy density in radiation, regions of the universe where the decay occurs at a later time stay matter dominated longer and will be denser than regions where decay happens earlier. This gives density perturbations of order

$$\frac{\delta\rho}{\rho} \sim -\frac{\delta\Gamma}{\Gamma} \sim \frac{\delta\tau}{\tau}\,, \tag{5.1}$$

where

$$\tau \equiv t_{\rm RH} - t_0 \tag{5.2}$$

is the time between the end of inflation (t_0) and reheating ($t_{\rm RH}$). The evolution of density perturbations in this scenario has been studied in detail in [135, 139].

In a similar way, modifications to the particle properties of the particles *produced* during reheating can also introduce energy density perturbations. Density perturbations are created if the decay products interact with fields that were light during inflation.

To see this, we need to discuss how the inflaton reheats. Suppose reheating occurs through direct (Born) decay of the inflaton. Then a fluctuation in the mass of the decay product χ modifies the inflaton decay width, because of the dependence of the available phase space on the masses of the final state particles. These lead

to *calculable* density perturbations since the exact dependence of the width on the mass of the light particles can be computed in any given model [138, 140]. If, for example, the inflaton decays via $\Phi \to \chi\chi$ then the tree-level decay width is modified from phase space by an amount

$$\frac{\delta\Gamma}{\Gamma} = -2\frac{\delta m_\chi^2}{m_\phi^2 - 4m_\chi^2} + 2\left(\frac{\delta m_\chi^2}{m_\phi^2 - 4m_\chi^2}\right)^2 + \cdots . \tag{5.3}$$

If Φ decays near threshold, then the resulting density perturbation dependence on δm_χ^2 can be large and highly non-linear.

We expect a δm_χ^2 with a super-horizon spatial variation to be generated if χ interacts with a field σ that was light during the inflationary era and through to the era of reheating. Note that even in the absence of direct couplings of the fields χ and σ, they are expected to interact indirectly through some intermediate states. Quantum corrections will typically generate a dependence of m_χ^2 on the super-horizon fluctuations of σ at some order in perturbation theory, as indicated by Fig. 5.1. In this paper we focus mainly on the effect that fluctuations in the mass of the particles produced during reheating or preheating have on density perturbations.

Besides reheating through direct Born decay, the inflaton may instead reheat the universe through parametric resonance (preheating) [141, 142, 143, 144, 145]. Preheating can be very efficient and be completed very soon after inflation, within $\mathcal{O}(10-100)$ oscillations of the inflaton field about its minimum. Whether this process of reheating dominates over the Born decay into bosons or fermions depends on the parameters of the model [1].

[1]The growth of perturbations during the matter-dominated era of the oscillating inflaton has been studied in [146] and, if parametric resonance occurs, in [147].

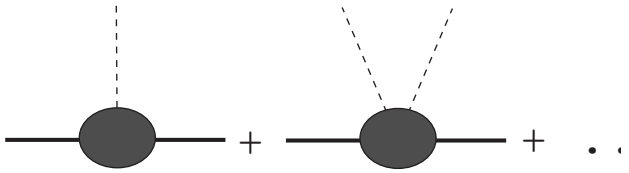

Figure 5.1: Quantum corrections may generate a dependence of m_χ^2 on super-horizon fluctuations in σ.

In the scenario of DGZK, additional density perturbations can be created during preheating, by modifying the time it takes for parametric resonance to complete and for the universe to thermalize. The size of this time interval depends on the parameters of the model, and in particular on the mass of the produced particles, which we discuss below in a simple model. This is the main subject of this paper. Depending on how efficient preheating is, the size of the time interval can have a weak or strong sensitivity to the mass of the decay products.

We use the canonical model of preheating and add a scalar σ which we assume is light during inflation so that it acquires super-horizon perturbations $\delta\sigma(x) \sim H_{\rm inf}$ during that era. For this to occur it is necessary that during inflation its mass satisfies $m_\sigma < H_{\rm inf}$. σ is assumed to interact more strongly with the χ compared to Φ. The interactions we consider are

$$-\mathcal{L}_I = \frac{g^2}{2}\Phi^2\chi^2 + \mu\,\chi^2\sigma + \frac{\lambda}{2}\chi^2\sigma^2 + \frac{m_\chi^2}{2}\chi^2 + \frac{m_\sigma^2}{2}\sigma^2. \tag{5.4}$$

A Z_2 symmetry $\chi \to -\chi$ has been imposed for simplicity. Self-interactions σ^4 and χ^4 are assumed to be irrelevant during the first stage of preheating defined below. We assume that at the end of inflation the fields χ and σ are near enough to the minimum of their potential so that we can neglect the motion of their zero modes.

Inflation ends when $t = t_0 \simeq 1/m_\Phi$ and is followed by a matter-dominated era

described by rapid oscillations of the inflaton about the minimum of its potential which we assume to be

$$V(\Phi) = \frac{1}{2} m_\Phi^2 \Phi^2 \ . \tag{5.5}$$

For simplicity we assume that the inflationary potential is also described by this simple quadratic form, giving rise to chaotic inflation [148]. During inflation, $H_{\rm inf} \simeq m_\Phi$. At the end of inflation $\Phi = \Phi_0 \simeq m_{\rm pl}/3$ and thereafter decays as $\Phi(t) \simeq m_{\rm pl}/3m_\Phi t$.

For large enough coupling g, these oscillations trigger parametric resonance, and the energy density in χ increases exponentially [141]. If this process is efficient, the universe eventually is dominated by the χ particles, which then thermalize the universe at some later time through its interactions with Standard Model or Grand Unified Model particles.

The perturbations in the inflaton give rise to adiabatic density perturbations, whose size depend on the form of the inflaton potential. In this letter we concentrate on the density perturbations generated from the fluctuations in the σ scalar field. In de Sitter space [149]

$$\langle \sigma^2(0) \rangle = \frac{H_{\rm inf}^2}{4\pi^2} N \, , \tag{5.6}$$

$$\langle \sigma(x)\, \sigma(y) \rangle = \frac{H_{\rm inf}^2}{4\pi^2} \, , \tag{5.7}$$

where in Eq. (5.6) N is the number of e-foldings during inflation. In Eq. (5.7) the comoving coordinates x, y are well seperated and we neglect the logarithmic dependence on $|x-y|$.

The χ field does not acquire super-horizon perturbations because its effective

mass

$$m^2_{\chi,\mathrm{eff}} = m^2_\chi + g^2\,|\Phi|^2 + \lambda\frac{H^2_{\mathrm{inf}}}{4\pi^2}N \tag{5.8}$$

during inflation is larger than the Hubble parameter for parameter values which allow for efficient parametric resonance. Henceforth we absorb the $\lambda H^2_{\mathrm{inf}}N/(4\pi^2)$ into m^2_χ. Treating σ as an external field, its fluctuations can be absorbed into fluctuations in the mass of the field χ,

$$\delta m^2_\chi \;\;=\;\; 2\,\mu\,\delta\sigma + \lambda\,\delta\sigma^2. \tag{5.9}$$

where we have used

$$\delta\sigma \equiv \sigma - \langle\sigma\rangle\,, \quad \delta\sigma^2 \equiv \sigma^2 - \langle\sigma^2\rangle\,, \tag{5.10}$$

and we will impose $\langle\sigma\rangle = 0$. The size of the fluctuations δm^2_χ is determined by the two-point function

$$\langle\delta m^2_\chi(x)\,\delta m^2_\chi(y)\rangle = 4\mu^2\langle\sigma(x)\,\sigma(y)\rangle + 2\lambda^2\langle\sigma(x)\sigma(y)\rangle^2$$

Using Eqs. (5.6) and (5.7) we find the fluctuations for widely separated comoving coordinates x and y to be of order

$$\delta m^2_\chi \sim \sqrt{\mu^2 H^2_{\mathrm{inf}} + \lambda^2 H^4_{\mathrm{inf}}}\,. \tag{5.11}$$

While the field $\sigma(x)$ is Gaussian, the fluctuation δm^2_χ is only Gaussian for $\lambda = 0$.

For $\lambda H_{\rm inf}^2 \gg \mu H_{\rm inf}$, δm_χ^2 is highly non-Gaussian. For example, consider in this limit the three-point function for equally separated comoving coordinates. One finds for the analog of skewness

$$\frac{\langle \delta m_\chi^2(x)\delta m_\chi^2(y)\delta m_\chi^2(z)\rangle}{\langle \delta m_\chi^2(x)\delta m_\chi^2(y)\rangle^{3/2}} = \frac{8\langle\sigma(x)\sigma(y)\rangle\langle\sigma(y)\sigma(z)\rangle\langle\sigma(z)\sigma(x)\rangle}{2^{3/2}\langle\sigma(x)\sigma(y)\rangle^3} = 2\sqrt{2}\,. \tag{5.12}$$

For the remainder of this paper we set $\mu = 0$ which corresponds to imposing a $\sigma \to -\sigma$ symmetry. We make this decision to simplify the analysis of the backreaction of χ on σ discussed below. Then

$$\frac{\delta m_\chi^2}{m_\Phi^2} \sim \lambda \frac{H_{\rm inf}^2}{m_\Phi^2} \simeq \lambda\ . \tag{5.13}$$

These fluctuations in δm_χ^2 are non-Gaussian and always positive.

This situation would be excluded if this were the only source of density perturbations. A more interesting scenario in this situation would be if the dominant source of perturbations came from the inflaton potential. Then the perturbations generated during preheating providing a sub-dominant, non-Gaussian contribution. Since here the source for the non-Gaussian perturbations is *not* the same as the source -the inflaton- providing the dominant Gaussian contribution, the current limits on non-Gaussianity [150] do not apply, since those limits assume that the non-Gaussian and Gaussian perturbations are generated by the same field.

We define preheating to last until significant particle production of χ occurs and the energy densities in Φ and χ become equal. The duration of this stage depends

on m_χ and coupling constant g,

$$\tau = \tau(g, m_\chi) \ . \tag{5.14}$$

Fluctuations in m_χ and the coupling g give rise to density fluctuations from Eq. (5.1).

Fluctuations in g can be generated if it is replaced by an effective coupling

$$g_{\rm eff}^2 = g^2 \left(1 + \frac{\sigma^2}{M^2}\right) \ , \tag{5.15}$$

where M is some mass scale [151]. The σ dependence of $g_{\rm eff}$ generates non-Gaussian perturbations $\delta_g \equiv \delta g^2/g^2 = H_{\rm inf}^2/M^2$. It also modifies the large time-dependent mass of χ, an effect that is distinct from modifying m_χ. Here too we have to worry about the backreaction of χ on σ.

Next we describe our numerical method for determining the energy density in χ during preheating. Neglecting the backreaction of χ on the inflaton, which only becomes significant at the end of the preheating stage when $\rho_\chi = \rho_\Phi$ [143], the equation of motion for the fields $\chi \equiv \hat{\chi}(a_0/a)^{3/2}$ (a is the scale factor) and σ are

$$\hat{\chi}_k'' + [A_k + 2q\cos(2(z - z_0))]\,\hat{\chi}_k = 0 \tag{5.16}$$

$$\delta\sigma'' + \frac{2}{z}\delta\sigma' + m_{\sigma,\rm eff}^2\delta\sigma = 0 \ , \tag{5.17}$$

where derivatives are with respect to $z \equiv m_\Phi t$ and we have chosen $z_0 \equiv 1$. We have

defined

$$\begin{aligned} q &= \frac{g^2\Phi_0^2 a_0^3}{4a^3 m_\Phi^2} \equiv q_0 \frac{a_0^3}{a^3} \quad , \quad a_0 \equiv a(t_0) \\ A_k &= \frac{1}{m_\Phi^2}\left(k^2\frac{a_0^2}{a^2} + \widetilde{m}_\chi^2\right) + 2q \ , \end{aligned} \tag{5.18}$$

and the mass parameters are given by

$$\begin{aligned} \widetilde{m}_\chi^2 &= m_\chi^2 + \lambda\,\delta\sigma^2 \\ m_{\sigma,\mathrm{eff}}^2 &= m_\sigma^2 + \lambda\chi^2 \, . \end{aligned} \tag{5.19}$$

The equation for $\hat{\chi}_k$ describes a time-dependent harmonic oscillator with frequency $\Omega_k^2 = m_\Phi^2\,[A_k + 2q\cos(2(z - z_0))]$. In the limit of a static universe and constant $\delta\sigma$ this equation reduces to the Mathieu equation.

Efficient parametric resonance requires $q_0 \gg 1$ and $\widetilde{m}_\chi \lesssim m_\phi$. Note that we included a term of order $\lambda H_{\mathrm{inf}}^2 N$ into the definition of m_χ^2, where N is the number of e-foldings during inflation. The bound $\widetilde{m}_\chi \lesssim m_\phi$ therefore implies $N \lesssim \lambda^{-1}$. For the values of λ we consider, this is a very weak bound on the number of e-foldings during inflation.

For a given value of k the energy density in χ is

$$\rho_k(z) = \Omega_k(z) N_k(z) \ , \tag{5.20}$$

where $N_k(t)$ is the number density for a mode with given wave number k. The number density can be calculated by numerically solving for the Bogolyubov coefficient,

giving [142]

$$N_k(t) = \frac{a_0^3}{2\Omega_k a^3(t)} \left(\Omega_k^2(t) |\tilde{\chi}_k|^2 + m_\Phi^2 |\tilde{\chi}_k'|^2 \right) \ , \tag{5.21}$$

with initial conditions $\tilde{\chi}_k(t_0) = 1/\sqrt{2\Omega_k}$, $m_\Phi \tilde{\chi}_k'(t_0) = -i\sqrt{\Omega_k/2}$. The field $\tilde{\chi}_k$ satisfies the same equation as $\hat{\chi}_k$ and is related to it (see Appendix B of [142]). The energy density is obtained by integrating Eq. (5.20) to obtain

$$\rho_\chi(z) = \frac{1}{2\pi^2} \int_0^\infty k^2 dk \ \Omega_k(z) N_k(z) \ . \tag{5.22}$$

The exponentially large number density of χ particles leads to a large backreaction on σ that must be included to correctly determine the size of the effect we are describing. The backreaction of χ on σ can have two effects: first, it can lead to production of large numbers of σ particles, and second it gives rise to a large effective mass of the σ field. The first effect was analyzed by Felder and Kofman [152] using a numerical lattice simulation of preheating and the subsequent thermalization of the χ with the σ fields. In their Figures 14 and 15 they show the number densities of Φ, χ and σ. Their numerical results show that during preheating the number density in σ is much smaller than in either χ or Φ and its effect on the evolution of either n_χ or n_Φ is negligible. The second effect is more significant. Once $m_{\sigma,\mathrm{eff}}$ gets larger than H, the amplitude $\delta\sigma$ will decrease rapidly [153]. To simplify the analysis we will assume that the dependence of $m_{\sigma,\mathrm{eff}}$ on m_σ can be neglected. To estimate the time at which the backreaction becomes important, we compare the effective mass $m_{\sigma,\mathrm{eff}}^2 \sim \lambda \langle \chi^2 \rangle$ to the Hubble parameter. The ratio that determines their relative

importance can be expressed as

$$\frac{m^2_{\sigma,\rm eff}}{3H^2} = \frac{2\lambda}{3g^2}\frac{\rho_\chi}{\rho_\Phi}\frac{m^2_\Phi}{H^2}\ , \tag{5.23}$$

where we have used $m_{\chi,\rm eff} \simeq g|\Phi|$ and $\rho_\chi \simeq g|\Phi|n_\chi \simeq g^2\Phi^2\langle\chi^2\rangle$ [143]. For $\lambda \sim 10^{-5}$ and $H \sim 2m_\Phi/300$ we find that this backreaction becomes important when $\rho_\chi/\rho_\Phi \approx 3\,g^2$. For $\lambda \sim 10^{-7}$ the backreaction becomes important when $\rho_\chi/\rho_\Phi \approx 300\,g^2$. In this letter we will not solve the full coupled set of differential equations, but rather deal with this backreaction by turning off δm^2_χ at the time z_c when $m^2_{\sigma,\rm eff} = 3H^2$, i.e. defined implicitly by

$$\frac{\rho_\chi(z_c)}{\rho_\Phi(z_c)} \equiv \frac{g^2}{\lambda}\frac{2}{3z_c^2}\ . \tag{5.24}$$

Although for different values of δm^2_χ the intercept time z_c is different, that difference is second order in δm^2_χ. It is then sufficient to use the z_c obtained by setting $\delta m^2_\chi = 0$. If Eq.(5.24) intercepts R along a plateau corresponding to no particle production, then we make the conservative choice of cutting off the mass fluctuation at the location of the first intercept.

In Fig. 5.2 we display a logarithmic plot of the ratio $R \equiv \rho_\chi(t)/\rho_\Phi(t)$ together with Eq. (5.24) for scenario 1, as defined in Table 5.1. In order to estimate the sensitivity of $z_{\rm RH} = 1 + m_\Phi\tau$ on δm^2_χ, we show in Fig. 5.3 a magnification of the region where $R(z_{\rm RH}) = 1$. We also show these plots for the three other scenarios defined in Table 5.1 (keeping $m_\Phi/m_{\rm pl} = 10^{-6}$ fixed).

We are interested in the change in τ generated by a fluctuation $\delta m^2_\chi/m^2_\Phi \simeq \lambda$.

scenario	g	λ	m_χ^2/m_Φ^2	z_c	κ_m
1	4×10^{-4}	10^{-7}	0.1	88	0.8
2	6×10^{-4}	10^{-7}	0.4	82	0.15
3	4×10^{-4}	10^{-5}	0.1	47	0.14
4	6×10^{-4}	10^{-5}	0.4	50	0.06

Table 5.1: Definition of the four choices parameter sets. Also shown are the numerical results for z_c and κ_m, as defined in Eqs (5.24) and (5.25).

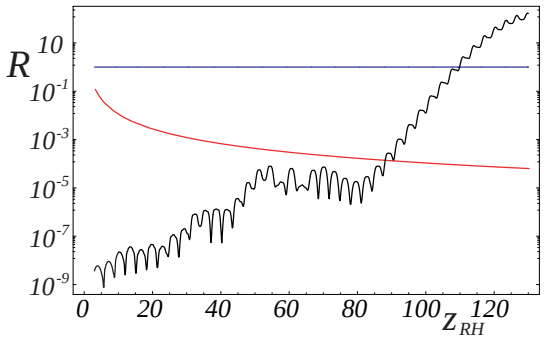

Figure 5.2: Logarithmic plot of $R = \rho_\chi/\rho_\Phi$. The chosen parameters are $g = 4\times10^{-4}$, $m_\Phi = 10^{-6}m_{\rm pl}$, $m_\chi^2/m_\Phi^2 = 0.1$. Also shown is Eq. (5.24) with $\lambda = 10^{-7}$.

Since λ is tiny, that change can be expressed as

$$\frac{\delta\tau}{\tau} = \kappa_m \frac{\delta m_\chi^2}{m_\Phi^2} \quad . \tag{5.25}$$

From Table 5.1 we can see that the typical κ_m is $\mathcal{O}(0.1-1)$.

The reader may wonder why we are using larger values for δm_χ^2 that are not consistent with the λ we choose. Since the perturbation $\delta\tau$ is linear in δm_χ^2, the κ_m obtained this way is unchanged if we were to use smaller values for δm_χ^2. The reason for this choice of δm_χ^2 is that the plots are easier to read. We also repeat that z_c was determined with the correct λ.

One may also wonder why the presence of a δm_χ^2 at early times has any effect at all, especially given that it only persists while $R \lesssim 10^{-5} - 10^{-3}$. Parametric resonance is dramatic because of stimulated emission. So even if at earlier times

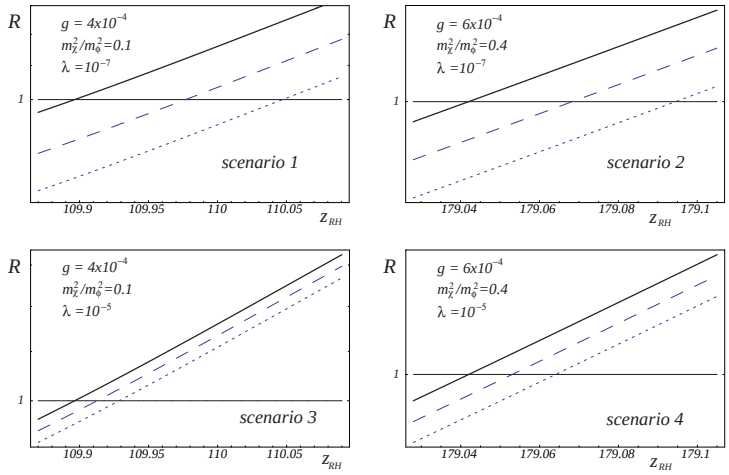

Figure 5.3: Logarithmic plot of the effect of the mass fluctuation δm_χ^2 on $z_{\rm RH}$. The chosen parameters are given in each figure. The solid line corresponds to $\delta m_\chi^2 = 0$, while the long and short dashed lines correspond to $\delta m_\chi^2/m_\Phi^2 = 10^{-3}$ and 2×10^{-3}, respectively.

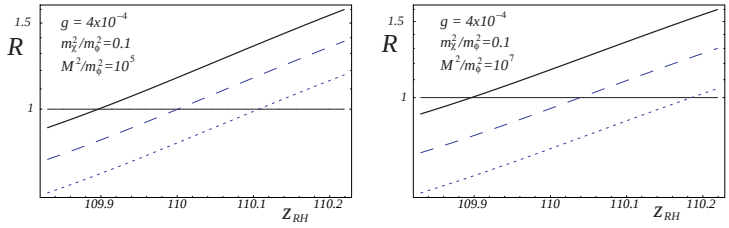

Figure 5.4: Logarithmic plot of the effect of the fluctuation in the coupling constant δg^2 on $z_{\rm RH}$. The chosen parameters are given in each figure. The solid line corresponds to $\delta g^2 = 0$, while the long and short dashed lines correspond to $\delta g^2/g^2 = 10^{-3}$ and 2×10^{-3}, respectively.

the production of χ particles is affected due to a non-zero δm_χ^2, this will impact the much greater growth occurring at later times. A more detailed numerical simulation, including all the effects of backreaction and scattering, such as done in [152] for preheating without a fluctuating σ field, is needed to explore in detail the sensitivity of $\delta\rho/\rho$ to super-horizon fluctuations in σ.

Mathematically, the intuition expressed above may be expressed in the following

way. The density in χ is approximately given by

$$\rho_\chi \simeq \widetilde{N}\frac{a_0^3}{a^3}\exp\left[\int_{t_0}^{t_{\rm RH}} dt\,\nu(t)\right] \tag{5.26}$$

where $\widetilde{N}$ is a prefactor that depends on the parameters of the model. Here ν is a characteristic exponent leading to exponential growth. We approximate its dependence on k as given by its value near $k \simeq 0$. The coefficient ν also depends on m_χ^2, so

$$\nu = \nu_0 - \nu_1 \frac{\delta m_\chi^2}{m_\Phi^2}\Theta(z_c - z)\ . \tag{5.27}$$

Numerically we find that $\nu_1/\nu_0 \sim \mathcal{O}(1)$ and is positive. A negative correlation is expected, since both the characteristic exponents of the Mathieu equation and the instability bands are the largest near the kinematic limit $A = 2q$, corresponding to $m_\chi = k = 0$. Increasing m_χ^2 removes more instability bands from the available phase space. Using the approximate formula above, we can solve for the change in the reheat time due to a fluctuation δm_χ^2, approximating all the dependence of $\delta\tau$ on δm_χ^2 as occurring from the exponential. This gives

$$\frac{\delta\tau}{\tau} \simeq -\frac{\nu_1}{\nu_0}\frac{\delta m_\chi^2}{m_\Phi^2}\frac{z_c}{z_{\rm RH}} \simeq \frac{\delta m_\chi^2}{m_\Phi^2}\frac{z_c}{z_{\rm RH}}\ . \tag{5.28}$$

This result has $\mathcal{O}(1)$ agreement with our previous numerical computations. (Compare $z_c/z_{\rm RH}$ with κ_m.) It illustrates that $\delta\tau/\tau$ is not suppressed by any very small numbers other than $\delta m_\chi^2/m_\Phi^2$.

We also explore the dependence of τ on fluctuations in $g_{\rm eff}$ [151]. For non-zero particle number n_χ the interaction (5.15) introduces a backreaction of χ on σ

corresponding to an effective mass $m^2_{\sigma,\rm eff} = g^2\Phi^2\langle\chi^2\rangle/M^2$. As before, we cut off the fluctuation in $g_{\rm eff}$ when $m^2_{\sigma,\rm eff} = 3H^2$. This occurs when

$$\frac{\rho_\chi}{\rho_\Phi} = \frac{M^2}{m^2_{\rm pl}} \ . \tag{5.29}$$

The fluctuation in $g_{\rm eff}$

$$\delta_g \equiv \frac{\delta g^2}{g^2} = \frac{H^2_{\rm inf}}{M^2} \ , \tag{5.30}$$

gives rise to non-Gaussian density perturbations.

In Fig. 5.4 we display the ratio R for $g = 4 \times 10^{-4}$, $m_\Phi/m_{\rm pl} = 10^{-6}$ and $m^2_\chi/m^2_\Phi = 0.1$. We choose two values of M that give $\delta_g = 10^{-5}$ and $\delta_g = 10^{-7}$. According to (5.29), the fluctuation in $g_{\rm eff}$ is cut off at $\rho_\chi/\rho_\Phi = 10^{-7}$ and 10^{-5}, respectively, corresponding to $z_c = 26$ and $z_c = 47$. For both of these parameters we find that there is a large linear effect which we express as

$$\frac{\delta\tau}{\tau} = \kappa_g\delta_g \ . \tag{5.31}$$

For $\delta_g = 10^{-5}$ we find $\kappa_g = 0.9$ and for $\delta_g = 10^{-7}$ we find $\kappa_g = 1.4$. As in the previous case, in obtaining our plots we used larger values of δ_g to determine κ_g.

In conclusion, we have shown that during preheating, interactions of the "decay products" of the inflaton with other light scalar fields can give rise to super-horizon mass fluctuations in these decay products. These fluctuations will then give rise to density perturbations of the universe. Depending on the coupling of the decay products of the inflaton to the light scalar fields, the dominant density perturbations generated from this effect will be either Gaussian or non-Gaussian.

Appendix A

Convergence of the Differential Map Maker

As described in Section 3.2.2, we introduce one new step to the differential map making algorithm presented by Wright et al. [96]: We initialize the iterations at the exact solution of Equation 3.7 evaluated at low resolution, which in this paper is taken to be $N_{\rm side} = 16$, with 3072 pixels.

To demonstrate the improvement in convergence due to this choice of initialization, we revisit the analytic case considered in Section 3.4, which compared the results from our simulation pipeline with an exact analytic case, but taking into account the actual WMAP scanning strategy.

In Figure A.1 we show a set of difference maps taken between the intermediate solutions produced by the differential map maker and the analytic and isotropic map solution. From top to bottom, the panels show the residuals after 2, 5 and 10 iterations, and at the bottom, the final converged solutions. The left panel shows the series obtained when initializing the search at the low-resolution solution, while the right panel shows the series when initializing at zero. Convergence was achieved respectively after 67 and 123 iterations in the two cases.

Note that the WMAP team initializes their search at the CMB dipole, which is

the dominant component in their data set. However, this is in our setting equivalent to initializing at zero, since our simulation does not include a dipole.

Taking the difference between the two final solutions, we have verified that the peak-to-peak residuals in the two maps are less than 0.1 μK, of which essentially all is concentrated in a single dipole component. The solution is thus independent of initialization, and the only difference lies in computational speed.

Finally, note that even though the two maps are internally indistinguishable, they are both quite different from the isotropic reference map. To be precise, the RMS difference between the derived maps and the isotropic reference map is 0.91 μK, with a spatial pattern similar to the overall WMAP scanning pattern.

The cause of these residuals is once again the differences in the treatment of the effective pixel windows: The HEALPix pixel window is computed by uniformly averaging over the full sky, whereas the simulation pipeline takes into account the actual pointing directions of the satellite. Sub-pixel variations in the CMB sky therefore leads to significant differences in the two estimates on small scales. The effect of such pixel window variations on the 5-year WMAP power spectrum will be considered in a future paper.

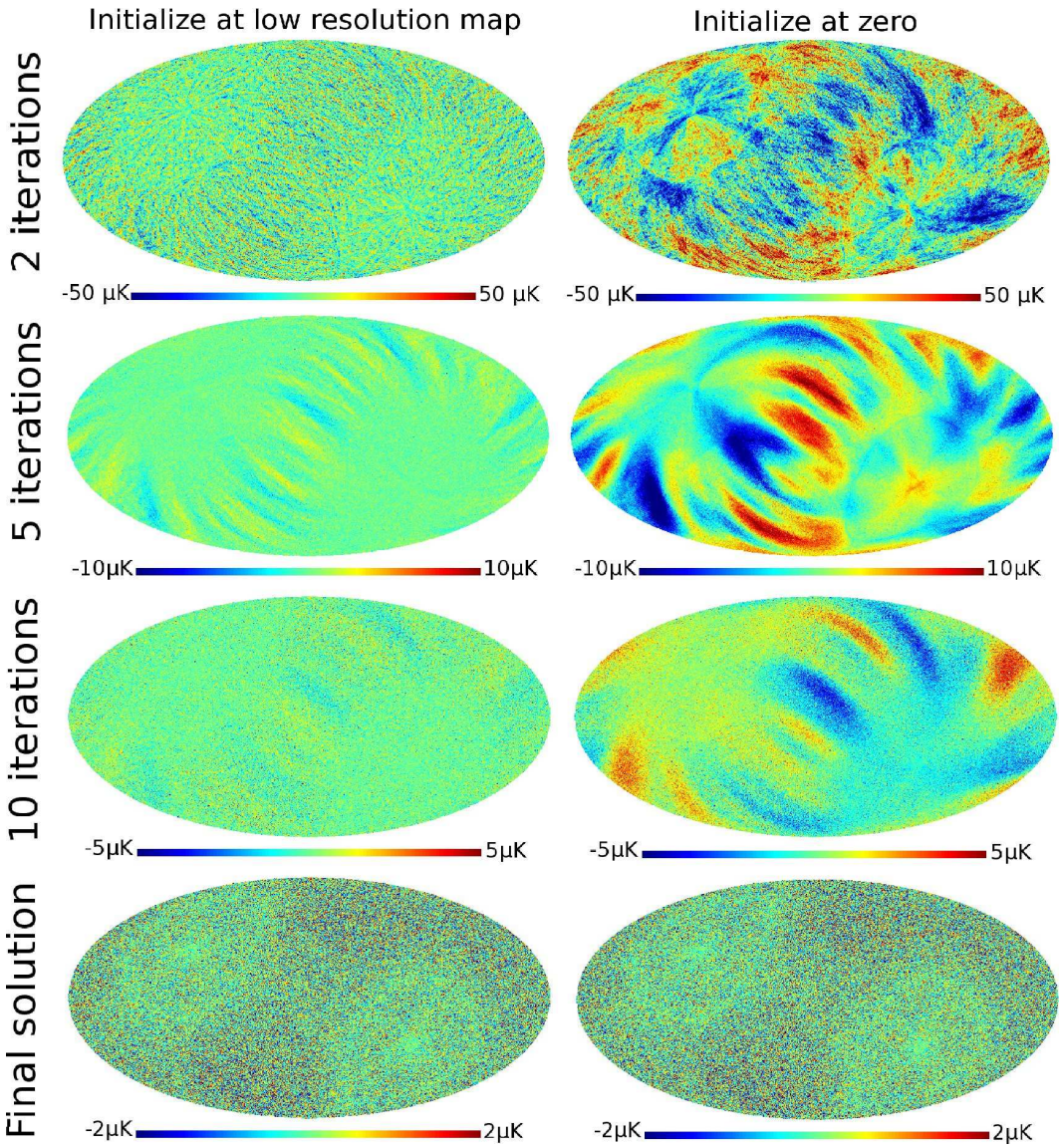

Figure A.1: Comparison of convergence of the differential map maker for two different choices of initialization. The left column shows the snapshots from the series obtained with initializing at a solution obtained by brute-force evaluation at low resolution, while the right column shows the series obtained when initializating at zero. Each plot is a difference map between the current solution for a data set including asymmetric beams and real scanning strategy and the corresponding map convolved with the analytic Gaussian beam and isotropic HEALPix pixel window. The bottom row shows the final solutions obtained in the two cases, which were obtained after 67 and 123 iterations, respectively. These final maps are idential up to a $\sim 0.1\mu$K dipole.

Bibliography

[1] E. Komatsu *et al.* [WMAP Collaboration], Astrophys. J. Suppl. **180**, 330 (2009) [arXiv:0803.0547 [astro-ph]].

[2] S. Dodelson *et al.* [SDSS Collaboration], Astrophys. J. **572**, 140 (2001) [arXiv:astro-ph/0107421]; S. Cole *et al.* [The 2dFGRS Collaboration], Mon. Not. Roy. Astron. Soc. **362**, 505 (2005) [arXiv:astro-ph/0501174].

[3] A. G. Riess *et al.* [Supernova Search Team Collaboration], Astron. J. **116**, 1009 (1998) [arXiv:astro-ph/9805201]; P. M. Garnavich *et al.* [Supernova Search Team Collaboration], Astrophys. J. **509**, 74 (1998) [arXiv:astro-ph/9806396]; S. Perlmutter *et al.* [Supernova Cosmology Project Collaboration], Astrophys. J. **517**, 565 (1999) [arXiv:astro-ph/9812133].

[4] C. Amsler *et al.* [Particle Data Group], Phys. Lett. B **667**, 1 (2008).

[5] A. H. Guth, Phys. Rev. D **23**, 347 (1981);

[6] A. D. Linde, Phys. Lett. B **108**, 389 (1982); A. Albrecht and P. J. Steinhardt, Phys. Rev. Lett. **48**, 1220 (1982).

[7] V. F. Mukhanov and G. V. Chibisov, JETP Lett. **33** (1981) 532 [Pisma Zh. Eksp. Teor. Fiz. **33** (1981) 549]; A. A. Starobinsky, Phys. Lett. B **117** (1982)

175; A. H. Guth and S. Y. Pi, Phys. Rev. Lett. **49** (1982) 1110; S. W. Hawking, Phys. Lett. B **115**, 295 (1982).

[8] L. Ackerman, S. M. Carroll and M. B. Wise, Phys. Rev. D **75**, 083502 (2007) [arXiv:astro-ph/0701357].

[9] L. Ackerman, M. R. Buckley, S. M. Carroll and M. Kamionkowski, Phys. Rev. D **79**, 023519 (2009) [arXiv:0810.5126 [hep-ph]].

[10] L. Ackerman, C. W. Bauer, M. L. Graesser and M. B. Wise, Phys. Lett. B **611**, 53 (2005) [arXiv:astro-ph/0412007].

[11] N. E. Groeneboom and H. K. Eriksen, Astrophys. J. **690**, 1807 (2009) [arXiv:0807.2242 [astro-ph]].

[12] G. Jungman, M. Kamionkowski and K. Griest, Phys. Rept. **267**, 195 (1996) [arXiv:hep-ph/9506380].

[13] G. Servant and T. M. P. Tait, Nucl. Phys. B **650**, 391 (2003) [arXiv:hep-ph/0206071]. H. C. Cheng, J. L. Feng and K. T. Matchev, Phys. Rev. Lett. **89**, 211301 (2002) [arXiv:hep-ph/0207125]. D. Hooper and S. Profumo, Phys. Rept. **453**, 29 (2007) [arXiv:hep-ph/0701197].

[14] D. N. Spergel and P. J. Steinhardt, Phys. Rev. Lett. **84**, 3760 (2000) [arXiv:astro-ph/9909386]; M. Kaplinghat, L. Knox and M. S. Turner, Phys. Rev. Lett. **85**, 3335 (2000) [arXiv:astro-ph/0005210]; A. Tasitsiomi, Int. J. Mod. Phys. D **12**, 1157 (2003) [arXiv:astro-ph/0205464].

V. F. Mukhanov and G. V. Chibisov, JETP Lett. **33** (1981) 532 [Pisma Zh. Eksp. Teor. Fiz. **33** (1981) 549]; A. A. Starobinsky, Phys. Lett. B **117** (1982)

175; A. H. Guth and S. Y. Pi, Phys. Rev. Lett. **49** (1982) 1110; S. W. Hawking, Phys. Lett. B **115**, 295 (1982).

[15] For a review of inflation see e.g. S. Dodelson, *Modern Cosmology*, Academic Press, San Diego (2003); D. Langlois, arXiv:hep-th/0405053.

[16] A. D. Linde, Phys. Lett. B **129** (1983) 177.

[17] A. D. Linde, Phys. Rev. D **49**, 748 (1994) [arXiv:astro-ph/9307002].

[18] A review of various models can be found in D. H. Lyth and A. Riotto, Phys. Rept. **314**, 1 (1999) [arXiv:hep-ph/9807278].

[19] G. F. Smoot *et al.*, Astrophys. J. **396**, L1 (1992); C. L. Bennett *et al.*, Astrophys. J. **464**, L1 (1996)

[20] J. E. Ruhl *et al.*, Astrophys. J. **599**, 786 (2003); S. Masi *et al.*, arXiv:astro-ph/0507509; W. C. Jones *et al.*, Astrophys. J. **647**, 823 (2006);

[21] M. C. Runyan *et al.*, Astrophys. J. Suppl. **149**, 265 (2003); C. l. Kuo *et al.* [ACBAR collaboration], Astrophys. J. **600**, 32 (2004).

[22] T. J. Pearson *et al.*, Astrophys. J. **591**, 556 (2003); A. C. S. Readhead *et al.*, Astrophys. J. **609**, 498 (2004).

[23] P. F. Scott *et al.*, Mon. Not. Roy. Astron. Soc. **341**, 1076 (2003); K. Grainge *et al.*, Mon. Not. Roy. Astron. Soc. **341**, L23 (2003); C. Dickinson *et al.*, extended Mon. Not. Roy. Astron. Soc. **353**, 732 (2004).

[24] A. Benoit *et al.* [Archeops Collaboration], Astron. Astrophys. **399**, L19 (2003); M. Tristram *et al.*, Astron. Astrophys. **436**, 785 (2005).

[25] N. W. Halverson *et al.*, Background Astrophys. J. **568**, 38 (2002).

[26] A. T. Lee *et al.*, Astrophys. J. **561**, L1 (2001).

[27] D. N. Spergel *et al.* [WMAP Collaboration], Astrophys. J. Suppl. **170**, 377 (2007)

[28] G. Hinshaw *et al.* [WMAP Collaboration], Astrophys. J. Suppl. **170**, 288 (2007)

[29] A. Zee, Phys. Rev. D **25**, 1864 (1982).

[30] S. M. Carroll, G. B. Field and R. Jackiw, Phys. Rev. D **41**, 1231 (1990).

[31] S. R. Coleman and S. L. Glashow, Phys. Lett. B **405**, 249 (1997) [arXiv:hep-ph/9703240].

[32] D. Colladay and V. A. Kostelecky, Phys. Rev. D **58**, 116002 (1998) [arXiv:hep-ph/9809521].

[33] J. Soda and S. Kanno, arXiv:gr-qc/0612069.

[34] A. de Oliveira-Costa, M. Tegmark, M. Zaldarriaga and A. Hamilton, Phys. Rev. D **69**, 063516 (2004) [arXiv:astro-ph/0307282].

[35] H. K. Eriksen, F. K. Hansen, A. J. Banday, K. M. Gorski and P. B. Lilje, Astrophys. J. **605**, 14 (2004) [Erratum-ibid. **609**, 1198 (2004)] [arXiv:astro-ph/0307507].

[36] C. J. Copi, D. Huterer and G. D. Starkman, Phys. Rev. D **70**, 043515 (2004) [arXiv:astro-ph/0310511].

[37] D. J. Schwarz, G. D. Starkman, D. Huterer and C. J. Copi, Phys. Rev. Lett. **93**, 221301 (2004) [arXiv:astro-ph/0403353].

[38] F. K. Hansen, A. J. Banday and K. M. Gorski, Mon. Not. Roy. Astron. Soc. **354**, 1714 (2004) [arXiv:astro-ph/0404206].

[39] S. Prunet, J. P. Uzan, F. Bernardeau and T. Brunier, Phys. Rev. D **71**, 083508 (2005) [arXiv:astro-ph/0406364].

[40] H. K. Eriksen, A. J. Banday, K. M. Gorski and P. B. Lilje, Astrophys. J. **622**, 58 (2005) [arXiv:astro-ph/0407271].

[41] K. Land and J. Magueijo, Phys. Rev. Lett. **95**, 071301 (2005) [arXiv:astro-ph/0502237].

[42] T. R. Jaffe, A. J. Banday, H. K. Eriksen, K. M. Gorski and F. K. Hansen, Astrophys. J. **629**, L1 (2005) [arXiv:astro-ph/0503213].

[43] C. J. Copi, D. Huterer, D. J. Schwarz and G. D. Starkman, Mon. Not. Roy. Astron. Soc. **367**, 79 (2006) [arXiv:astro-ph/0508047].

[44] K. Land and J. Magueijo, Mon. Not. Roy. Astron. Soc. **367**, 1714 (2006) [arXiv:astro-ph/0509752].

[45] A. Bernui, T. Villela, C. A. Wuensche, R. Leonardi and I. Ferreira, arXiv:astro-ph/0601593.

[46] Y. Wiaux, P. Vielva, E. Martinez-Gonzalez and P. Vandergheynst, Phys. Rev. Lett. **96**, 151303 (2006) [arXiv:astro-ph/0603367].

[47] L. R. Abramo, A. Bernui, I. S. Ferreira, T. Villela and C. A. Wuensche, Phys. Rev. D **74**, 063506 (2006) [arXiv:astro-ph/0604346].

[48] J. Magueijo and R. D. Sorkin, arXiv:astro-ph/0604410.

[49] A. Hajian and T. Souradeep, Phys. Rev. D **74**, 123521 (2006) [arXiv:astro-ph/0607153].

[50] C. G. Park, C. Park and J. R. I. Gott, arXiv:astro-ph/0608129.

[51] D. Huterer, New Astron. Rev. **50**, 868 (2006) [arXiv:astro-ph/0608318].

[52] P. Vielva, Y. Wiaux, E. Martinez-Gonzalez and P. Vandergheynst, New Astron. Rev. **50**, 880 (2006) [arXiv:astro-ph/0609147].

[53] K. Land and J. Magueijo, arXiv:astro-ph/0611518.

[54] H. K. Eriksen, A. J. Banday, K. M. Gorski, F. K. Hansen and P. B. Lilje, Astrophys. J. **660**, L81 (2007) [arXiv:astro-ph/0701089].

[55] A. Berera, R. V. Buniy and T. W. Kephart, JCAP **0410**, 016 (2004) [arXiv:hep-ph/0311233].

[56] E. P. Donoghue and J. F. Donoghue, Phys. Rev. D **71**, 043002 (2005) [arXiv:astro-ph/0411237].

[57] C. Gordon, W. Hu, D. Huterer and T. Crawford, Phys. Rev. D **72**, 103002 (2005) [arXiv:astro-ph/0509301].

[58] C. Armendariz-Picon, JCAP **0603**, 002 (2006) [arXiv:astro-ph/0509893].

[59] R. V. Buniy, A. Berera and T. W. Kephart, Phys. Rev. D **73**, 063529 (2006) [arXiv:hep-th/0511115].

[60] J. G. Cresswell, A. R. Liddle, P. Mukherjee and A. Riazuelo, Phys. Rev. D **73**, 041302 (2006) [arXiv:astro-ph/0512017].

[61] S. H. S. Alexander, arXiv:hep-th/0601034.

[62] R. A. Battye and A. Moss, Phys. Rev. D **74**, 041301 (2006) [arXiv:astro-ph/0602377].

[63] L. Campanelli, P. Cea and L. Tedesco, Phys. Rev. Lett. **97**, 131302 (2006) [Erratum-ibid. **97**, 209903 (2006)] [arXiv:astro-ph/0606266].

[64] A. E. Gümrükcüoğlu, C. R. Contaldi and M. Peloso, arXiv:astro-ph/0608405.

[65] E. A. Lim, Phys. Rev. D **71**, 063504 (2005) [arXiv:astro-ph/0407437].

[66] G. B. Arfken and A. J. Weber, *Mathematical Methods for Physicists*, Academic Press (1995)

[67] G. Dvali, A. Gruzinov and M. Zaldarriaga, Phys. Rev. D **69**, 023505 (2004) [arXiv:astro-ph/030359]; G. Dvali, A. Gruzinov and M. Zaldarriaga, Phys. Rev. D **69**, 083505 (2004) [arXiv:astro-ph/0305548]; L. Kofman, plenary talk COSMO-02, Chicago, September 2002, astro-ph/0303614.

[68] V. A. Kostelecky and S. Samuel, Phys. Rev. D **40**, 1886 (1989).

[69] T. Jacobson and D. Mattingly, Phys. Rev. D **64**, 024028 (2001) [arXiv:gr-qc/0007031].

[70] T. Jacobson and D. Mattingly, Phys. Rev. D **70**, 024003 (2004) [arXiv:gr-qc/0402005].

[71] S. M. Carroll and E. A. Lim, Phys. Rev. D **70**, 123525 (2004) [arXiv:hep-th/0407149].

[72] C. Eling and T. Jacobson, Phys. Rev. D **69**, 064005 (2004) [arXiv:gr-qc/0310044].

[73] V. A. Kostelecky, Phys. Rev. D **69**, 105009 (2004) [arXiv:hep-th/0312310].

[74] R. W. Wald, Phys. Rev. D **28** (1983) 2118.

[75] S. Weinberg, Phys. Rev. D **72**, 043514 (2005) [arXiv:hep-th/0506236].

[76] L. Ackerman, S. M. Carroll and M. B. Wise, Phys. Rev. D **75**, 083502 (2007)

[77] C. L. Bennett *et al.* [WMAP Collaboration], Astrophys. J. Suppl. **148**, 1 (2003)

[78] J. Dunkley *et al.* [WMAP Collaboration], Astrophys. J. Suppl. **180**, 306 (2009)

[79] H. K. Eriksen *et al.*, Astrophys. J. **656**, 641 (2007)

[80] K. M. Gorski, E. Hivon, A. J. Banday, B. D. Wandelt, F. K. Hansen, M. Reinecke and M. Bartelman, Astrophys. J. **622**, 759 (2005)

[81] Green, P. J., & Silverman, B. W. 1994, Non-Parametric Regression and Generalized Linear Models, Chapman and Hall, 1994

[82] N. E. Groeneboom and H. K. Eriksen, Astrophys. J. **690**, 1807 (2009)

[83] Groeneboom, N. E., Eriksen, H. K., Gorski, K., Huey, G., Jewell, J., & Wandelt, B. 2009, arXiv:0904.2554

[84] R. S. Hill *et al.* [WMAP Collaboration], Astrophys. J. Suppl. **180**, 246 (2009)

[85] G. Hinshaw *et al.* [WMAP Collaboration], Astrophys. J. Suppl. **148**, 63 (2003) G. Hinshaw *et al.* [WMAP Collaboration], Astrophys. J. Suppl. **170**, 288 (2007)

[86] G. Hinshaw *et al.* [WMAP Collaboration], Astrophys. J. Suppl. **180**, 225 (2009)

[87] Hivon, E., Górski, K. M., Netterfield, C. B., Crill, B. P., Prunet, S., & Hansen, F. Astrophys. J. **567**, 2 (2002)

[88] K. M. Huffenberger, H. K. Eriksen and F. K. Hansen, Astrophys. J. **651**, L81 (2006)

[89] N. Jarosik *et al.* [WMAP Collaboration], Astrophys. J. Suppl. **170**, 263 (2007) E. Komatsu *et al.* [WMAP Collaboration], Astrophys. J. Suppl. **180**, 330 (2009)

[90] A. Lewis and S. Bridle, Phys. Rev. D **66**, 103511 (2002)

[91] M. R. Nolta *et al.* [WMAP Collaboration], Astrophys. J. Suppl. **180**, 296 (2009)

[92] L. Page *et al.* [WMAP Collaboration], Astrophys. J. Suppl. **148**, 39 (2003)

[93] Press, W. H. 2002, "Numerical recipes in C++ : the art of scientific computing", Cambridge University Press, ISBN: 0521750334

[94] D. N. Spergel *et al.* [WMAP Collaboration], Astrophys. J. Suppl. **170**, 377 (2007)

[95] B. D. Wandelt and K. M. Gorski, Phys. Rev. D **63**, 123002 (2001)

[96] Wright, E. L., Hinshaw, G., & Bennett, C. L., Astrophys. J. **458**, L53 (1996)

[97] L. Bergstrom, Rept. Prog. Phys. **63**, 793 (2000) [arXiv:hep-ph/0002126].

[98] G. Bertone, D. Hooper and J. Silk, Phys. Rept. **405**, 279 (2005) [arXiv:hep-ph/0404175].

G. Servant and T. M. P. Tait, Nucl. Phys. B **650**, 391 (2003) [arXiv:hep-ph/0206071]. H. C. Cheng, J. L. Feng and K. T. Matchev, Phys. Rev. Lett. **89**, 211301 (2002) [arXiv:hep-ph/0207125]. D. Hooper and S. Profumo, Phys. Rept. **453**, 29 (2007) [arXiv:hep-ph/0701197].

D. N. Spergel and P. J. Steinhardt, Phys. Rev. Lett. **84**, 3760 (2000) [arXiv:astro-ph/9909386]; M. Kaplinghat, L. Knox and M. S. Turner, Phys. Rev. Lett. **85**, 3335 (2000) [arXiv:astro-ph/0005210]; A. Tasitsiomi, Int. J. Mod. Phys. D **12**, 1157 (2003) [arXiv:astro-ph/0205464].

[99] B. D. Wandelt, R. Dave, G. R. Farrar, P. C. McGuire, D. N. Spergel and P. J. Steinhardt, arXiv:astro-ph/0006344.

[100] J. A. Frieman and B. A. Gradwohl, Phys. Rev. Lett. **67**, 2926 (1991). B. A. Gradwohl and J. A. Frieman, Astrophys. J. **398**, 407 (1992); G. W. Anderson and S. M. Carroll, arXiv:astro-ph/9711288; S. M. Carroll, Phys. Rev. Lett. **81**, 3067 (1998) [arXiv:astro-ph/9806099]; G. R. Farrar and P. J. E. Peebles, Astrophys. J. **604**, 1 (2004) [arXiv:astro-ph/0307316]; S. S. Gubser and P. J. E. Peebles, Phys. Rev. D **70**, 123511 (2004) [arXiv:hep-th/0407097]; S. S. Gubser and P. J. E. Peebles, Phys. Rev. D **70**, 123510 (2004) [arXiv:hep-th/0402225]; O. Bertolami and J. Paramos, Phys. Rev. D **71**, 023521 (2005) [arXiv:astro-ph/0408216]; A. Nusser, S. S. Gubser and P. J. E. Peebles, Phys.

Rev. D **71**, 083505 (2005) [arXiv:astro-ph/0412586]; R. Bean, E. E. Flanagan and M. Trodden, Phys. Rev. D **78**, 023009 (2008) [arXiv:0709.1128 [astro-ph]]; M. Kesden and M. Kamionkowski, Phys. Rev. D **74**, 083007 (2006) [arXiv:astro-ph/0608095]; M. Kesden and M. Kamionkowski, Phys. Rev. Lett. **97**, 131303 (2006) [arXiv:astro-ph/0606566]; J. Bovy and G. R. Farrar, arXiv:0807.3060 [hep-ph]; S. M. Carroll, S. Mantry, M. J. Ramsey-Musolf and C. W. Stubbs, arXiv:0807.4363 [hep-ph].

[101] D. Hooper and K. M. Zurek, Phys. Rev. D **77**, 087302 (2008) [arXiv:0801.3686 [hep-ph]].

[102] A. De Rujula, S. L. Glashow and U. Sarid, Nucl. Phys. B **333**, 173 (1990).

[103] B. Holdom, Phys. Lett. B **166**, 196 (1986).

[104] S. Davidson, S. Hannestad and G. Raffelt, JHEP **0005**, 003 (2000) [arXiv:hep-ph/0001179].

[105] S. Dimopoulos, D. Eichler, R. Esmailzadeh and G. D. Starkman, Phys. Rev. D **41**, 2388 (1990).

[106] L. Chuzhoy and E. W. Kolb, JCAP **0907**, 014 (2009) [arXiv:0809.0436 [astro-ph]].

[107] S. S. Gubser and P. J. E. Peebles, Phys. Rev. D **70**, 123510 (2004) [arXiv:hep-th/0402225].

[108] J. L. Feng and J. Kumar, Phys. Rev. Lett. **101**, 231301 (2008) [arXiv:0803.4196 [hep-ph]].

[109] J. L. Feng, H. Tu and H. B. Yu, JCAP **0810**, 043 (2008) [arXiv:0808.2318 [hep-ph]].

[110] B. A. Dobrescu, Phys. Rev. Lett. **94**, 151802 (2005) [arXiv:hep-ph/0411004].

[111] M. Pospelov, A. Ritz and M. B. Voloshin, Phys. Lett. B **662**, 53 (2008) [arXiv:0711.4866 [hep-ph]].

[112] D. V. Ahluwalia, C. Y. Lee, D. Schritt and T. F. Watson, arXiv:0712.4190 [hep-ph].

[113] E. Kolb and M.S. Turner, "The Early Universe," Addison-Wesley Publishing Company, Redwood City, (1990)

[114] L. B. Okun, Sov. Phys. JETP **56**, 502 (1982) [Zh. Eksp. Teor. Fiz. **83**, 892 (1982)].

[115] R. H. Cyburt, B. D. Fields, K. A. Olive and E. Skillman, Astropart. Phys. **23**, 313 (2005) [arXiv:astro-ph/0408033].

[116] T. L. Smith, E. Pierpaoli and M. Kamionkowski, Phys. Rev. Lett. **97**, 021301 (2006) [arXiv:astro-ph/0603144].

[117] J. Hisano, S. Matsumoto, M. M. Nojiri and O. Saito, Phys. Rev. D **71**, 063528 (2005) [arXiv:hep-ph/0412403]; M. Cirelli, A. Strumia and M. Tamburini, Nucl. Phys. B **787**, 152 (2007) [arXiv:0706.4071 [hep-ph]]. M. Cirelli, M. Kadastik, M. Raidal and A. Strumia, arXiv:0809.2409 [hep-ph]. N. Arkani-Hamed, D. P. Finkbeiner, T. Slatyer and N. Weiner, arXiv:0810.0713 [hep-ph]. M. Pospelov and A. Ritz, arXiv:0810.1502 [hep-ph];

[118] M. Kamionkowski and S. Profumo, Phys. Rev. Lett. **101**, 261301 (2008) [arXiv:0810.3233 [astro-ph]].

[119] J. Miralda-Escude, arXiv:astro-ph/0002050.

[120] R. Dave, D. N. Spergel, P. J. Steinhardt and B. D. Wandelt, Astrophys. J. **547**, 574 (2001) [arXiv:astro-ph/0006218].

[121] N. Yoshida, V. Springel, S. D. M. White and G. Tormen, arXiv:astro-ph/0006134.

[122] D. Clowe, M. Bradac, A. H. Gonzalez, M. Markevitch, S. W. Randall, C. Jones and D. Zaritsky, Astrophys. J. **648**, L109 (2006) [arXiv:astro-ph/0608407].

[123] S. W. Randall, M. Markevitch, D. Clowe, A. H. Gonzalez and M. Bradac, arXiv:0704.0261 [astro-ph].

[124] O. Y. Gnedin and J. P. Ostriker, arXiv:astro-ph/0010436.

[125] J. J. Dalcanton and C. J. Hogan, Astrophys. J. **561**, 35 (2001) [arXiv:astro-ph/0004381]; C. J. Hogan and J. J. Dalcanton, Phys. Rev. D **62**, 063511 (2000) [arXiv:astro-ph/0002330].

[126] M. Cirelli, N. Fornengo and A. Strumia, Nucl. Phys. B **753**, 178 (2006) [arXiv:hep-ph/0512090].

[127] P. J. E. Peebles, "Principles of physical cosmology," *Princeton, USA: Univ. Pr. (1993) 718 p*

[128] E. S. Weibel, Phys. Rev. Lett. **2**, 83 (1959); B. D. Fried, Phys. Fluids **2**, 337 (1959).

[129] M. V. Medvedev, L. O. Silva and M. Kamionkowski, Astrophys. J. **642**, L1 (2006) [arXiv:astro-ph/0512079].

[130] J. T. Frederiksen, C. B. Hededal, T. Haugboelle and A. Nordlund, Astrophys. J. **608**, L13 (2004) [arXiv:astro-ph/0308104]; K. I. Nishikawa, P. Hardee, G. Richardson, R. Preece, H. Sol and G. J. Fishman, Astrophys. J. **595**, 555 (2003) [arXiv:astro-ph/0305091]; L. O. Silva, R. A. Fonseca, J. Tonge, J. M. Dawson, W. B. Mori and M. V. Medvedev, Astrophys. J. **596**, L121 (2003) [arXiv:astro-ph/0307500]; M. Milosavljevic, E. Nakar and A. Spitkovsky, Astrophys. J. **637**, 765 (2006) [arXiv:astro-ph/0507553].

[131] J. March-Russell, S. M. West, D. Cumberbatch and D. Hooper, JHEP **0807**, 058 (2008) [arXiv:0801.3440 [hep-ph]].

[132] G. F. Smoot *et al.*, Astrophys. J. **396**, L1 (1992); C. L. Bennett *et al.*, Basic Astrophys. J. **464**, L1 (1996).

[133] C. L. Bennett *et al.*, Astrophys. J. Suppl. **148**, 1 (2003); D. N. Spergel *et al.* Astrophys. J. Suppl. **148**, 175 (2003).

[134] For a review see e.g. E. W. Kolb and M. S. Turner, *The Early Universe*, Perseus Publishing, (1990), Cambridge, Massachusetts.

[135] G. Dvali, A. Gruzinov and M. Zaldarriaga, Phys. Rev. D **69**, 023505 (2004).

[136] G. Dvali, A. Gruzinov and M. Zaldarriaga, Phys. Rev. D **69**, 083505 (2004).

[137] L. Kofman, plenary talk Cosmo03, Chicago, September 2002; astro-ph/0303614.

[138] M. Zaldarriaga, Phys. Rev. D **69**, 043508 (2004).

[139] S. Tsujikawa, Phys. Rev. D **68**, 083510 (2003); A. Mazumdar and M. Postma, Phys. Lett. B **573**, 5 (2003), Erratum-ibid. B **585**, 295 (2004); F. Vernizzi, Phys. Rev. D **69**, 083526 (2004).

[140] M. Postma, JCAP **0403**, 006 (2004).

[141] J. H. Traschen and R. H. Brandenberger, Phys. Rev. D **42**, 2491 (1990); L. Kofman, A. D. Linde and A. A. Starobinsky, Phys. Rev. Lett. **73**, 3195 (1994).

[142] Y. Shtanov, J. H. Traschen and R. H. Brandenberger, Phys. Rev. D **51**, 5438 (1995).

[143] L. Kofman, A. Linde and A. Starobinsky, Phys. Rev. D **56**, 3258 (1997).

[144] I. Zlatev, G. Huey and P. J. Steinhardt, Phys. Rev. D **57**, 2152 (1998).

[145] R. Micha and I. Tkachev, Phys. Rev. D **70**, 043538 (2004).

[146] B. Basset, Phys. Rev. D **56**, 3429 (1997); H. Kodama and T. Hamazaki, Prog. Theor. Phys. **96**, 949 (1996); T. Hamazaki and H. Kodama, Prog. Theor. Phys. **96**, 1123 (1996); Y. Nambu and A. Taruya, Prog. Theor. Phys. **97**, 83 (1997); F. Finelli and R. Brandenberger, Phys. Rev. Lett. **82**, 1362 (1999).

[147] S. Khlebnikov and I. Tkachev, Phys. Lett. B **390**, 80 (1997); S. Khlebnikov and I. Tkachev, Phys. Rev. Lett. **79**, 1607 (1997); S. Khlebnikov and I. Tkachev, Phys. Rev. D **56**, 653 (1997); B. Bassett, D. Kaiser and R. Maartens, Phys. Lett. B **455**, 84 (1999); B. A. Bassett, F. Tamburini, D. I. Kaiser and

R. Maartens, Nucl. Phys. B **561**, 188 (1999); F. Finelli and R. Brandenberger, Phys. Rev. D **62**, 083502 (2000); F. Finelli and S. Khlebnikov, Phys. Lett. B **504**, 309 (2001); F. Finelli and S. Khlebnikov, Phys. Rev. D **65**, 043505 (2002); K. Enqvist, A. Jokinen, A. Mazumdar, T. Multamäki, and A. Väihkönen, astro-ph/0411394.

[148] A. D. Linde, Phys. Lett. B **108**, 389 (1982).

[149] A. D. Linde, *Particle Physics and Inflationary Cosmology*, Harwood Academic Publishers, (1990), New York, New York.

[150] E. Komatsu *et al.*, Astrophys. J. Suppl. **148**, 119 (2003).

[151] F. Bernardeau, L. Kofman and J. P. Uzan, Phys. Rev. D **70**, 083004 (2004).

[152] G. N. Felder and L. Kofman, Phys. Rev. D **63**, 103503 (2001).

[153] K. Enqvist, A. Mazumdar and M. Postma, Phys. Rev. D **67**, 121303 (2003).